

ABSTRACT

Title of Dissertation: HYPERSPECTRAL IMAGING AND PATTERN
 RECOGNITION TECHNOLOGIES FOR REAL TIME
 FRUIT SAFETY AND QUALITY INSPECTION

Xuemei Cheng, Doctor of Philosophy, 2004

Dissertation directed by: Professor Yang Tao
 Department of Biological Resources Engineering

Hyperspectral band selection and band combination has become a powerful tool and have gained enormous interest among researchers. An important task in hyperspectral data processing is to reduce the redundancy of the spectral and spatial information without losing any valuable details that are needed for the subsequent detection, discrimination and classification processes. An integrated principal component analysis (PCA) and Fisher linear discriminant (FLD) method has been developed for feature band selection, and other pattern recognition technologies have been applied and compared with the developed method. The results on different types of defects from cucumber and apple samples show that the integrated PCA-FLD method outperforms PCA, FLD and canonical discriminant methods when they are used separately for classification. The

integrated method adds a new tool for the multivariate analysis of hyperspectral images and can be extended to other hyperspectral imaging applications.

Dimensionality reduction not only serves as the first step of data processing that leads to a significant decrease in computational complexity in the successive procedures, but also a research tool for determining optimal spectra requirement for online automatic inspection of fruit. In this study, the hyperspectral research shows that the near infrared spectrum at 753nm is best for detecting apple defect. When applied for online apple defect inspection, over 98% of good apple detection rate is achieved. However, commercially available apple sorting and inspection machines cannot effectively solve the stem-calyx problems involved in automatic apple defects detection. In this study, a dual-spectrum NIR/MIR sensing method is applied. This technique can effectively distinguish true defects from stems and calyxes, which leads to a potential solution of the problem. The results of this study will advance the technology in fruit safety and quality inspection and improve the cost-effectiveness of fruit packing processes.

HYPERSPECTRAL IMAGING AND PATTERN RECOGNITION TECHNOLOGIES
FOR REAL TIME FRUIT SAFETY AND QUALITY INSPECTION

By

Xuemei Cheng

Dissertation submitted to the Faculty of the Graduate School of the
University of Maryland, College Park in partial fulfillment
of the requirements for the degree of
Doctor of Philosophy
2004

Advisory Committee:

Professor Yang Tao, Chair
Professor Yud-Ren Chen
Professor Hubert Montas
Professor Nam Sun Wang
Professor Fredrick Wheaton

©Copyright by

Xuemei Cheng

2004

ACKNOWLEDGEMENTS

First I would like to thank my advisor and committee chairman, Dr. Yang Tao, for his invaluable guidance and insight into all the aspects of this research. In addition, his confidence in my capability has enabled much of my creative work as well as diligent working habits. I would like to express sincere thanks to Dr. Yud-Ren Chen for his immeasurable guidance, patience, and support throughout the course of my Ph.D. study. I have learned much as a direct result of working with him. I would also like to thank Dr. Hubert Montas, Dr. Nam Sun Wang, Dr. Fredrick Wheaton, and Dr. Estelle Russek-Cohan for serving on my committee and for their time, support, and helpful advice during my research and academic development.

Also, I wish to express my gratitude to Dr.M.S.Kim, Dr.A.M.Lefcourt for their insights, advice and valuable time on helping me with hyperspectral-sensing equipments. I especially thank Dr. C.Y.Wang who provided all the cucumber samples, storage equipments and expert opinions on our experiments. Special thanks to Ms. Diane Chan for her devoted time, her cooperation and great help in the cucumber experiments and data collection that made this research possible. I would like to thank all the present and former members of USDA Instrumentation and Sensing Lab for their support and help during my Ph.D study.

I would like to express my gratitude to all present and former members of the Bio-Imaging and Machine Vision Laboratory at the University of Maryland at College

Park. Special thanks to Ms. Abby Vogel for providing invaluable suggestions and helpful comments on the manuscript.

I want to express my appreciation to all the faculty and friends in ENBE department at University of Maryland at College Park for their support.

Finally, I would like to express my deepest gratitude to my family for their love and support during my study at the University of Maryland.

TABLE OF CONTENTS

ACKNOWLEDGEMENTS	ii
LIST OF TABLES	vi
LIST OF FIGURES	vii
Chapter 1 INTRODUCTION.....	1
Chapter 2 OBJECTIVES	5
Chapter 3 REVIEW OF LITERATURE.....	7
3.1. Nondestructive methods to ensure safety and quality of fresh produce	7
3.1.1 The importance of safety and quality assurance of fresh produce.....	7
3.1.2 The Popular Non-Destructive Techniques.....	9
3.2 Near-Infrared and Mid-Infrared Technology.....	10
3.2.1 Overview of Near Infrared spectroscopy.....	10
3.2.2 Typical Applications of NIR Spectroscopy.....	14
3.2.3 NIR Technology in Fruits and Vegetables.....	17
3.2.4 Mid-Infrared sensing and imaging Applications	19
3.3 On-line Automated Defect Detection of Apples.....	22
3.3.1 On-line System Requirements	22
3.3.2 Challenges for on-line system design	23
3.4 Machine Vision System	28
3.4.1 Machine Vision as a controlled system	29
3.4.2 Machine Vision as a Real-Time System.....	31
3.4.3 Future Trends of Machine Vision.....	33
3.5 Hyperspectral Sensing and Imaging	35
3.5.1 Brief Overview.....	35
3.5.2 Optimal Band Selection and Combination Problem.....	36
Chapter 4 A NOVEL INTEGRATED PCA AND FLD METHOD OF HYPER SPECTRAL IMAGE FEATURE EXTRACTION FOR CUCUMBER CHILLING DAMAGE INSPECTION	39
4.1 Introduction.....	39
4.2 Material and Method.....	41
4.2.1 Sample Materials	42
4.2.2 Hyperspectral Sensing System.....	45
4.2.3 Feature Extraction with Integrated PCA-FLD Method	46
4.3 Results and Discussion	51
4.4 Conclusions.....	59
Chapter 5 COMPARISION OF PATTERN RECOGNITION METHODS FOR HYPER SPECTRAL IMAGING AND BAND SELECTION.....	61
5.1 Introduction.....	61
5.2 Material and Method.....	67
5.2.1 Image acquisition.....	67
5.2.2 Image preprocessing	69
5.2.3 Statistical pattern recognition	74
5.2.4 Artificial neural network.....	78
5.3 Results and Discussion	80
5.3.1 Band Selection Method.....	81

5.3.2 Neural Network Classifier	93
5.3.3 Texture based feature extraction of cucumber images	101
5.4 Conclusions.....	103
Chapter 6 A NIR/MIR DUAL-SENSOR MACHINE VISION SYSTEM FOR ON- LINE APPLE STEM-END/CALYX RECOGNITION.....	105
6.1 Introduction.....	105
6.2 Material and Method.....	108
6.2.1 Machine Vision System	108
6.2.2 Dual Imaging Methods	110
6.3 Results and Discussion	121
6.4 Conclusions.....	125
Chapter 7 CONCLUSION	126
Chapter 8 FUTURE STUDIES	128
REFERENCE.....	129

LIST OF TABLES

Table 3.1 Applications of NIR dyes for popular technologies (Raghavachari, 2001)	17
Table 4.1 Cucumber Sample Diversity	45
Table 4.2 Samples Used for Optimal K Value Tests	54
Table 4.3 Samples Used for the Experiments	56
Table 4.4 Summary of Three Feature Extraction Methods.....	58
Table 5.1 Summary of properties and parameters of input apple samples	81
Table 5.2 Best three-band combinations given by different band combination methods for (a) raw data set and, (b) log data set.....	86
Table 6.1 Properties of the samples used for testing the performance of the online dual NIR/MIR sensing system.	110

LIST OF FIGURES

Figure 3.1 Ball-and-spring model	11
Figure 3.2 Potential energy diagrams for (a) the ball on spring model and (b) the quantum mechanical model of molecular vibrations.	13
Figure 4.1 Four levels of chilling injury (presented in the rectangular area) of cucumbers detected in this study. (a) trace chilling injury (b) slight chilling injury (c) moderate chilling injury (d) severe chilling injury. The images used were 800nm near infrared image.	43
Figure 4.2 The NIR reflectance images of a slightly chilling damaged cucumber and a good one with bumpy skin. The two images show the similarity in appearance of the two cucumbers. The images were taken at 800 nm. (a) A cucumber with slight chilling damages (b) A healthy cucumber with bumpy skin.	43
Figure 4.3 The hyperspectral reflectance effect on wholesome (bumpy good and smooth good) cucumbers and unwholesome (with chilling injury level of trace, slight, moderate, and severe) cucumbers.	52
Figure 4.4 (a) The good cucumber recognition rates versus K values for four evaluating tests, where each test used 20 different image samples. (b) The Chilling injury detection rate versus K values for the same four validating tests as in (a).	53
Figure 4.5 Chilling injury detection rates and good cucumber recognition rates were shown by using FLD, PCA and integrated FLD-PCA methods for the first experiment, where 20 image samples were used for training and the other 80 image samples were used for testing. The rates were calculated based on the total 100 testing cucumber image samples.	55
Figure 4.6 Chilling injury detection rates and good cucumber recognition rates were shown by using FLD, PCA and integrated FLD-PCA methods for the second experiment, where a total 60 cucumber image samples were used as training samples and the same 60 cucumber images were tested.	57
Figure 4.7 Chilling injury detection rates and good cucumber recognition rates were shown by using FLD, PCA and integrated FLD-PCA methods for the third experiment, where 40 image samples were used as training samples and another 80 image samples were used as testing samples. The rates were calculated based on the 80 testing image samples only.	57
Figure 5.1 Model for statistical pattern recognition [Jain et al.,2000].	63
Figure 5.2 5×5 Gaussian filter with $\sigma = 1.0$	70
Figure 5.3 Dimension reduction of hyperspectral image cube. (a) The original hyperspectral image cube and three-dimensional coordinates system, where axis x and y are the spatial dimension and axis s is the spectral dimension. (b) The 2D image representation after dimension reduction, and the 2D coordinate system, where axis x' is the transformed spatial dimension and axis s is the spectral dimension again.	71
Figure 5.4 The multi-layer feed forward artificial neural network used in this study.	79
Figure 5.5 Typical apple samples used for this study.	80
Figure 5.6 Defect detection rate of integrated PCA-FLD projection with different K values for raw data and log transformed data.	84

Figure 5.7 Good apple recognition rate vs. defect recognition rate of five band selection methods for raw data set.	84
Figure 5.8 Good apple recognition rate vs. defect recognition rate of five band selection methods for log data.	85
Figure 5.9 Discriminant power of three different projection methods: PCA, integrated PCA-FLD and FLD, when applied individually with raw data and log data.	89
Figure 5.10 Discriminant power of different projection methods: PCA, integrated PCA-FLD and FLD, when compared under one large feature space with different input data: raw data and log data.	90
Figure 5.11 Good apple recognition rate and defect recognition rate using different projection-based methods followed by stepwise discriminant analysis with raw data input.	91
Figure 5.12 Good apple recognition rate and defect recognition rate using different projection-based methods followed by stepwise discriminant analysis with log data input.	92
Figure 5.13 Training curve of neural network 1	95
Figure 5.14 Relation between detection rate and number of hidden neurons in neural network 1. This network is trained to differentiate good and defective apples. .	96
Figure 5.15 Training curve of neural network 2, which is used to differentiate defect on apples from stem/calyx.	97
Figure 5.16 Relation between detection rate and number of hidden neurons in neural network 2. This network is trained to differentiate defects on apples from stem/calyx.	98
Figure 5.17 Training curve of neural network 3, which is used to differentiate the following three classes of objects, i.e., good apples, defects, and stem/calyx....	99
Figure 5.18 Relation between detection rate and number of hidden neurons in neural network 3. This network is trained to differentiate three classes of objects, i.e., good apples, defects, and stem/calyx.	100
Figure 5.19. Comparison of various degrees of cucumber chilling damages, where (a) shows severe chilling damage, (b) indicates slight chilling damages, and in (c) there is no chilling damage.	102
Figure 5.20 Recognition rate of cucumber chilling damages vs. normal cucumber skin using Gabor texture features, where (a) shows the recognition rate of slight/trace chilling damages and (b) shows the recognition rate of normal cucumber skin.	103
Figure 6.1 Schematic representation of the machine vision system for online apple defect inspection.	109
Figure 6.2 Schematic representation of the relationship among the sensing objects, the NIR sensor and the MIR sensor.	111
Figure 6.3 Schematic representation of binary interpolation.	113
Figure 6.4 The flow chart of the on-line image processing procedure	114
Figure 6.5 Schematic representation for the principle of spherical transformation method.	116
Figure 6.6 Spherical transform curves for two different sized objects.	117

Figure 6.7 An example result of dual NIR/MIR sensing algorithm. (a) original NIR image, (b) background removed MIR image, (c) normalized NIR image, (d) resized MIR image, (e)adaptive transformed NIR image, (f) blob extracted MIR image, (g) blob extracted NIR image, (h)dual image combination result image. The boundary lines on the apples in (f), (g) and (h) were artificially added for visualization purpose.	122
Figure 6.8 The test result of sample recognition rates for online dual NIR/MIR sensing algorithm.	124

CHAPTER 1 INTRODUCTION

The United States packs over 220 million boxes of apples each year (Tao, 1996). In a typical apple packing line, the apples are floated in a cleaning tank before they are elevated onto an inspection table. Apples with rot, injury, disease, serious bruising and other defects must be removed at this early stage (before waxing) to prevent cross-contamination and reduce subsequent processing cost. Workers along the inspection table will inspect the apples and remove the defective apples and foreign materials. After inspection, the apples are transferred to cleaning, waxing and drying lines. At the final stage, apples are sorted according to their color, size and shape, and then packaged into cartons according to their grades.

Although some aspects of the packing process have been automated, much of it is still done manually. A key step of the apple packing process, the defect inspection process, is still done by hand. Workers are positioned along the apple conveyors to visually inspect the passing apples and remove those with defects and foreign materials such as branches and leaves. Working in a wet environment and inspecting a large amount of apples each day is a difficult and labor-intensive job. With tons of apples passing in front of the eyes of workers, human fatigue is unavoidable; there are always falsely classified apples passing through the human inspectors.

An automated defect inspection system would significantly enhance the fresh fruit packing process. It will liberate humans from traditional hand manipulation of agricultural products. Moreover, it will reduce the costs of energy, labor and materials

as well. It can work continuously for long hours and improve the quality of fresh apples and the productivity of packing.

Optical imaging techniques are among the major methods used for designing a non-destructive fruit inspection machine. Machines equipped with optical imaging sensors, in particular, multispectral imaging sensors, become machine vision systems that play a key role for automatic fruit quality and safety inspection. The multispectral imaging sensors typically collect spectral information in a few (usually two or three) selected discrete spectral bands. Different inspection spectra displays different features of the target object. The combination of the multispectral information leads to faster and more efficient target identification compared with a single spectral inspection. However, the system design becomes more complicated. Successful design of a multispectral machine vision system relies on accurate selections of the spectral bands from a wide range of possible inspection spectra. For specific inspection tasks, the selection of bands differ. Optical systems designed to provide high resolution of spectral bands over a wide spectral range are called hyperspectral sensing or imaging systems. Band selection and band combination from the hyperspectral band data become critical to the efficiency of on-line multispectral inspection systems.

Hyperspectral sensing/imaging has been used since the 1980s in detection of reflective radiation and in identification of various surface targets, topological or geological features (Shaw and Manolakis, 2002). The hyperspectral sensors are developed to sample the reflective portion of the electromagnetic spectrum. The entire inspection spectrum spans from the visible region through the near infrared,

and are divided into hundreds of narrow contiguous bands. The spectrum interval can be as narrow as nanometers in wavelength, and as a result, over 100 spectral channels are usually obtained at the same time. Since image data are considered two dimensional, by adding a new dimension of “spectrum” information, the hyperspectral data can be perceived as a three-dimensional data cube.

The rich collection of spectral responses makes it possible to identify the spectral reflection peaks and absorbing troughs of materials instantly. The important information sensed is preserved and precise differentiation and classification over the field of interest are possible. Of course, it is unnecessary for researchers to analyze the obtained image data frame by frame, since in most cases, the acquired data could be redundant. Usually only several or even a single spectrum signature is enough to uniquely characterize the materials of interest. The method for optimal band selection and band combination is an important topic in the field of hyperspectral data processing. The most common method used is the principal component analysis (PCA). It is a classic method in solving the dimensionality reduction problem. However, does this method really match our requirement of band selection? What should the criteria be to measure the efficiency of selected bands over the hundreds of spectra? How can the selected bands be combined to reach the optimal inspection effects? These are questions to be answered in this research.

When the optimal inspection band is determined and applied to the machine vision system for automatic apple defect inspection, however, there is another problem that needs to be solved: how to distinguish the stem-end and calyx from true defects such as bruises, rots, and limb rubs? Once the stems-end or calyx appears in

the field of view of a near-infrared camera, they could be mistakenly identified as defects, because they are similar to the true defective spots in the image and difficult to be differentiated even by human eyes. To address this problem, a NIR/MIR dual-sensor imaging method was developed. The dual-spectral method combines the results of near infrared (NIR) and mid-infrared (MIR) images of apples that can effectively differentiate the stem-end and calyx from true defects (Cheng, et.al., 2002). Fast algorithms and a DSP hardware system are used in this research to implement this new method for real time apple defect inspection.

CHAPTER 2 OBJECTIVES

The overall objective of this research is to integrate hyperspectral imaging, real time machine vision, dual-spectral sensing, and pattern recognition techniques for automatic defect inspection in fresh produce. In particular, these technologies will be applied for cucumber chilling damage inspection and online apple defect detection. The band selection and band combination method is developed based on the optimal band selection criteria, and the method is expected to be extended and applied to general band combination needs for hyperspectral data dimensionality reduction. An online machine vision system is developed to distinguish the stem-ends and calyxes from the true defects of apples. The specific objectives for this project are:

- (1) To develop a pattern recognition method for hyperspectral band selection and band combination applications. Apply this method to cucumber chilling damage inspection and apple defect inspection and test feasibility with these applications.
- (2) To assess the performance and the discriminant power of the new method in comparison with other classic pattern recognition methods. Further the study by applying different pre-processing methods to the original input image data.
- (3) To develop a NIR/MIR machine vision system for online apple defect detection with the optimal near-infrared inspection band obtained from hyperspectral sensing results. To identify stems/calyxes from true defects

and to increase the accuracy of online apple defect inspection through this system.

- (4) To apply neural network classification method for apple defect detection.

Compare the defect detection rate and stem-calyx identification performance with the online dual-camera machine vision system performance.

This dissertation is organized as follows. Chapter 3 describes the overview of this study along with background information of the technical challenges identified from the literature. Chapter 4 is a published journal paper devoted to objective (1). Chapter 5 addresses the objectives (2) and (4). Chapter 6 is another published journal paper that is intended to meet objective (3). The overall conclusion of the dissertation is presented in chapter 7, and suggestions for further study are given in chapter 8.

CHAPTER 3 REVIEW OF LITERATURE

3.1. Nondestructive methods to ensure safety and quality of fresh produce

3.1.1 The importance of safety and quality assurance of fresh produce

Fresh fruits and vegetables are rich in essential vitamins and minerals, fiber, carbohydrates, and phytochemicals (Harvard School of Public Health, 2004). They've been demonstrated to have many health benefits, such as lowered risk for certain cancers, stroke, heart disease, and high blood pressure, etc.. Therefore, an increased and enriched consumption of a variety of fruits and vegetables has been encouraged by nutrition authorities worldwide. According to the General Accounting Office (GAO) report on July 2002, American's consumption of fruit and vegetable has each increased by 0.2 servings between 1989-1996 (or almost ½ serving total) such that the average consumption is near the recommended minimum of 5 servings per day (GAO, 2002). However, the increased consumption of fresh produce has also raised concerns regarding potential safety and quality issues of fresh fruits and vegetables.

In 1983, the Expert Committee on Food Safety convened jointly by the World Health Organization (WHO) and Food and Agricultural Organization (FAO) of the U.N. concluded that illness due to contaminated food is “the most widespread health problem in the contemporary world” (FAO/WHO, 1984, Safety 2002). Fresh produce has become a particular food safety concern since it is generally consumed raw. Both biological and chemical contaminations can occur in raw fruits and vegetables due to

natural causes or during agricultural production procedures. Biological hazards generally refer to food borne microorganisms such as bacteria, viruses, parasites, and some fungi that are able to produce toxins. Chemical hazards are mainly toxic chemicals and pesticides that are associated with environmental pollution. Without proper detection and processing procedures, those contaminations can be transferred to the human body and cause illness. According to the U.S. Center for Disease Control and Prevention (CDC), the number of fresh produce-related food borne disease outbreaks is increasing. In 1973-1979, only 2% of U.S. food borne disease outbreaks were associated with fresh produce while during 1990-1997, this percentage had increased to 6%. The effects of unsafe fruits and vegetables on human health have become one important reason for studying produce safety.

Another complicated issue about fresh produce is quality concern. In general, quality of a fresh produce includes appearance (size, shape, color, gloss, and freedom from defects and decay), texture (firmness, crispness, juiciness, mealiness, and toughness, depending on the commodity), flavor (sweetness, sourness (acidity), astringency, aroma, and off-flavors), and nutritive value (vitamins, minerals, dietary fiber, phytonutrients). Although poor quality of fresh produce will not cause human illness, it can be negatively affected by biological agents (such as post-harvest diseases and post-harvest pests) causing undesirable changes in, for example, texture, taste, appearance, and storage life of the produce. These changes can have a strong adverse economic impact. The need for developing and enhancing the value of fruit and vegetable products has increased dramatically as a result of global competition and market demands.

3.1.2 The Popular Non-Destructive Techniques

In order to deliver a safe and wholesome final product from the fields to the consumers, fruit and vegetable processors are seeking ideas and methods to improve safety and quality of their products in every step along this chain. In particular, an effective safety and quality assurance mechanism throughout the post-harvest handling steps becomes critical. On one hand, high levels of worker hygiene should be enforced to reduce the possible sources of post-harvest contamination. On the other hand, careful harvesting, proper packaging, storage, and transport should be managed to maintain good produce quality (post harvest handling).

Non-destructive methods have been widely used in the research and development community to monitor quality and safety attributes of fresh produce. According to the literature, non-destructive inspection methods have been applied to fruits such as apples, oranges, strawberries, tomato, peaches, pears, etc., and vegetables such as mushrooms, potatoes, carrots, onions, cucumbers, etc (Brosnan and Sun, 2002.).

The availability of low-cost microcomputers and solid-state imaging systems have resulted in increased use of computer-aided machine vision systems to make non-destructive methods more reliable and efficient to ensure the safety and quality of produces. Different light sources and sensing methods have been reported to be used as non-destructive inspection tools. For instance, far-red (725-735nm) lighting from incandescent bulbs and high-pressure sodium lighting have been used to increase the greenness and prolong shelf life of greenhouse-grown cucumbers (Lin and Jolliffe, 1996). The non-destructive measurement of fluorescence parameters have been used

to indicate heat injury in apples (Song et al., 2001); to distinguish maturation, ripeness, and senescence of apples (Song et al., 1997); and to determine the residues of multiple pesticides in fresh produce, such as apples, bananas, cabbages, carrots, cucumbers, lettuce, oranges, pears, peppers, and pineapples (Fillion et al., 2000). Ultrasound treatment incorporated along packing lines has been used to remove and destroy external pests on fruit surfaces (Hansen, 2001). Laser Doppler vibrometer has been used to evaluate different stages of ripeness, firmness and maturity of fruits (Muramatsu et al., 2000, Terasaki, S. et al., 2001). X-ray imaging has been reported to detect the internal damages of sweet onions (Tollner et al., 1999.), the spit pins in peaches (Han et al., 1992), water core damage in apples (Kim and Schatzki, 2000) and pinhole damage in almonds (Kim and Schatzki, 2001, Brosnan and Sun, 2004). Nevertheless, for non-destructive fruit and vegetable surface defect inspection, infrared sensing and imaging technology are the most feasible and viable option.

3.2 Near-Infrared and Mid-Infrared Technology

3.2.1 Overview of Near Infrared spectroscopy

The initial discovery of infrared energy was credited to Sir William Herschel, a British Royal Astronomer in 1800, when he dispersed sunlight through a prism and detected it with a sensitive thermometer. He found the energy beyond the red end of visible light and demonstrated that there is a relationship between temperature and wavelength (Spiro and Schlessinger, 1989). Since its discovery, the study of infrared has led to discovery of the fundamental theories and laws of thermal radiation, and infrared properties are important for exploring the potential structure of different

materials. The infrared range of the electromagnetic spectrum spans from approximately 0.75 μm to 1000 μm . The range is often further divided into near infrared, middle infrared and far infrared. Although there is no exact designation for the separation of infrared bands, the range from 700nm to 2500 nm is generally accepted as near infrared, from 2500 nm up to 6 μm or 7 μm is called middle infrared, and from 7 μm to 15 μm (or 16 μm) bandwidth is commonly considered as far infrared and extreme far infrared ranges from 16 μm to 1mm.

Near-infrared spectroscopy is typically used to investigate the quantitative measurements of organic functional groups. The NIR absorption bands can be considered as a consequence of molecular vibrations of chemical compounds. Infrared radiation absorbed by a molecule can cause a bond to vibrate similarly to a diatomic oscillator, or a “ball-and-spring” model (Raghavachari, 2001), as shown in figure 3.1. The vibration frequency ν (cm^{-1}) is determined by equation 3.1.

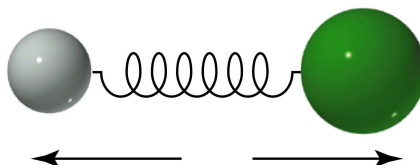


Figure 3.1 Ball-and-spring model

$$\nu = \frac{1}{2\pi c} \sqrt{\frac{k}{m}} \quad (3.1)$$

where c is the speed of light and k is the force constant ($5 \times 10^5 \text{ dynes cm}^{-1}$), and m is derived from equation 3.2:

$$m = \frac{m_1 m_2}{m_1 + m_2} \quad (3.2)$$

where m_1 and m_2 are the masses of the two nuclei. From quantum mechanics point of view, the “ball-on-spring” model results in an equally spaced energy level, shown in figure 3.2(a). That is, the molecular system can change states by only one quantum level a time. Equations 3.1 and 3.2 are known as “Hooke’s Law”, which is usually used to determine the fundamental vibration frequency of mid-IR, while near-IR is comprised of combination bands and overtones. Hooke’s Law is one of the two Laws that govern the basics of vibration spectroscopy. The other law is called Franck-Condon Principle. The Frank-Condon principle states that electronic transitions tend to take place between vibrational energy levels when nuclear kinetic energies are small. These small variations cause anharmonic oscillations between molecules. Therefore, NIR combination bands and overtones are not precise integral times of fundamental frequencies but the imprecise multiple of fundamentals. In reality, the energy curve of an oscillating molecule is more complicated than the “ball-on-spring” model and looks more like that shown in figure 3.2(b). Thus, it becomes possible for a molecule to change energy by more than one quantum level, thus resulting in higher energy photons that have higher frequencies and correspondingly shorter wavelengths than those of Mid-infrared fundamental changes. The anharmonicity is the cause of overtones and combination bands, and determines the occurrence and spectral prosperities of the NIR bands.

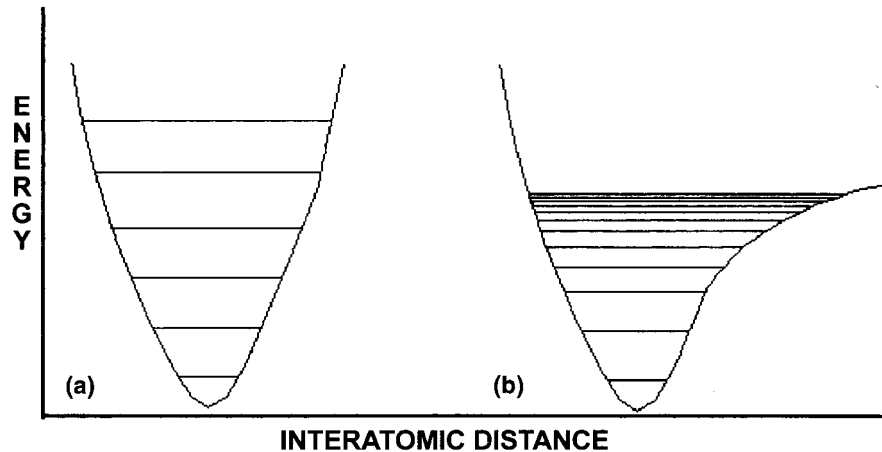


Figure 3.2 Potential energy diagrams for (a) the ball on spring model and (b) the quantum mechanical model of molecular vibrations.

Due to anharmonicity, the NIR spectral region is dominated by absorptions associated with highest anharmonicity bonds involving the lightest atom hydrogen H, or described as XH_n functional groups. The typical active NIR functional groups are C-H, O-H and N-H groups that occur between 4000 and 2500 cm⁻¹. In particular, the O-H functional group or stretch of NIR spectroscopy, has been widely applied in food analysis to determine the moisture level and the state of water in various applications.

Typical NIR spectroscopic instruments include sources of radiation, a means of determining the wavelength and the energy of radiation, and detectors. The NIR sources of radiation varied from common incandescent lamp to tungsten halogen lamps, providing high energy from the visible region to approximately 2700nm. There are three types of NIR detectors: the silicon (Si) detectors, which are fast, low noise and highly sensitive from the visible to 1100nm; the lead sulfide (PbS) detectors, which are relatively slow, but sensitive and with high signal to noise properties from 1100nm to 2500nm; and the recent indium gallium arsenide (InGaAs) detectors, which are both fast and highly sensitive from visible region to 2300nm

(Raghavachari, 2001), but much more expensive than Si and PbS detectors. The NIR spectroscopic measurement instruments include multiple types of diffraction gratings, interference filters, and Fourier Transform Spectrometers (FTIRs).

3.2.2 Typical Applications of NIR Spectroscopy

NIR spectroscopy has been widely used in many areas, including industrial process control, chemistry, medical sciences, and agricultural products and foodstuffs inspections. Near infrared spectroscopy technologies have been used in polymer and plastic industry for monitoring chemical reactions and product stream for quality and environmental protection purposes (Siesler, 1996; Fischer et al., 2000; Eisenreich et al., 1996).

In basic science studies, such as chemistry, near-infrared spectroscopy has also become a powerful tool. Employing near-infrared spectroscopy for water content and sediment analysis has become a matter of keen interest. Researchers have been using near infrared reflectance spectroscopy to investigate the sediment composition (Korsman et al. 1999), pH value variations (Korsman et al. 1992), carbon, carbonate, nitrogen, and phosphorus contents (Malley et al. 1996, 2000; Nilsson et al., 1996) in water chemistry.

Besides chemistry and industrial applications, near-infrared spectroscopy has been successfully applied in the biotechnology field. With the development of photodiodes and semiconductor lasers, near infrared techniques have made much progress. Using near infrared dyes, DNA and protein analysis become feasible (Sowell, 2002). Near infrared laser radiation and absorption characteristics have been

used to localize cellular DNA damage within nanometre dimensions (Meldrum et al. 2003). A near infrared fluorescence imager has been constructed to obtain lifetime and intensity images for DNA sequencing gel slab applications (Lassiter et al., 2000). Near infrared technology has also been used in the recently emerging field of single-molecule detection experiments. By using the less expensive diode lasers, the background signals are greatly reduced in the near infrared wavelengths (Raghavachari, 2001). Applications ranged from the determination of single DNA fragments (Wabuyele et al., 2001), to imaging and analysis of activities and roles of a particular molecule for clinical detection purposes (Jaffer, 2004), and to the identification of specific genes in complex genomic mixtures (Castro and William, 1997).

Although applying near infrared spectroscopy in the medical sciences field is relatively new due to the complexity of the samples and intense water absorptions, NIR technology has been found very important and has been increasingly used in clinical chemistry, medical diagnosis and in skin and tissue studies. In the most exciting and elusive areas of clinical research such as gene therapy of cancer (Shah et al., 2004), detection of breast cancer (Chen et al., 2004), and determination of human blood constituents (Spanner and Niessner, 1996), near-infrared fluorescence (NIRF) reflectance spectroscopy, near-infrared diffuse optical spectroscopy (DOS) and diffuse optical imaging (DOI) show promise as noninvasive clinical techniques. In research on brain tissue (Raj et al., 2004), and breast tissue (Shah et al., 2004), and skin studies like skin wound repair (Danno et al., 2001), near infrared spectroscopy and instruments also play important roles.

Despite the rapid development of near infrared spectroscopy instruments and applications in different fields, the first and foremost modern near infrared spectroscopy application was recognized as developed in U.S. Department of Agriculture, Beltsville, Maryland in the mid to late-1960, largely by Karl Norris when measuring the composition of wheat, soy and other agriculture products. Modern near-infrared spectroscopy requires low-noise spectrometers, computerized control of the spectrometer and data acquisition, and the use of multivariate mathematical and statistical computer algorithms to analyze the data (Raghavachari, 2001). Karl Norris put all these together and the whole technology got its “kick” from that initial start. Now near infrared spectroscopy has become a standard method and routine analysis for determining protein, moisture, oil, and other contents of interest in wheat (Miralbes, 2003), soybeans (Bennett et al. 2003), crops and seeds (Wu, et al. 2002, Perez-Vich et al., 1998), grains (Delwiche et al., 1998), barley (Fontaine et al., 2002) and other agricultural products. Similarly, near infrared spectroscopy is also used for quality measurements for foodstuffs. For instances, near infrared technology is employed for the determination of protein, fat, lactose and total solids in milk (Laporte and Paquin, 1999), the identification of moisture, protein, oil and salt content of fish meat (Zhang et al., 2000), the measurements of the alcohol content for beverages such as beer (Coventry and Hunston, 1984) and wine (Burns and Gump, 1993), and monitoring the manufacture of processed food such as cheeses (Curda and Kukackova, 2004), cocoa butter and chocolate (Bolliger et al., 1999).

Beyond specific technology fields, near infrared spectroscopy and instruments are widely used in commercial industrial and popular technology fields. The origin of

near infrared absorbing dyes have been used for applications such as optical disks, CD-Rs, laser printers, electronic cameras, NIR cutoff filters (800nm to 1100nm), etc. Table 3.1 summarizes the different applications of NIR dyes for popular technologies. Those popular products in return have been used in different areas and served for different purposes.

Table 3.1 Applications of NIR dyes for popular technologies (Raghavachari, 2001)

Light source	Characteristic	Application
Diode laser, 780-840nm	Thermal decomposition	Optical disk, CD-R, optical card
	Photoconductivity; charge generation	OPC; laser printer; laser plate making
	photosensitivity	direct plate making (photoengraving)
	Thermal energy transfer	Dye diffusion thermal transfer
Sunlight (thermal light)	Reflection index	Transparent bar code; forgery preventive agent
	Heat absorption	Heat-shielding material
	Heat retention	Agricultural film, heat retaining fiber
	NIR absorption	Sunglasses, goggles
	Sun light absorption	Photovoltaic devices
Halogen lamp, LED	NIR absorption (800-1100 nm)	Electronic camera; automatic photographic exposure meter; NIR cutoff filter for PDP
	Fluorescence	Forgery-preventive agent; dye laser; probe
	photo initiation	Photoresist, photosensitizer
	Photosensitization	IR photography

3.2.3 NIR Technology in Fruits and Vegetables

Fruits and vegetables used to be unsuitable for NIR measurements because of the high moisture content and relatively large size. However, with the development of

high-performance NIR instruments, applying near-infrared techniques to monitor the quality of intact fruits and vegetables has become more and more popular. According to literature, near infrared spectroscopy has been applied to measure the firmness and sugar content of sweet cherries (Peirs et al., 2002), to determine the soluble content, firmness and titratable acidity of Jonagold apples (Downey, 2004), to determine soluble solids content of peaches (Peiris et al., 1998), to evaluate the sugar content of fresh melons (Sugiyama et al., 1999), and similar quality measurements of various fruits and vegetables. Despite the quality issues such as texture, flavor, and appearance, there is another important factor that influences the sorting and grading processes of fresh products – defect inspection. Near-infrared reflection spectroscopy has been applied widely in fruit defect inspection.

Usually the fruit surface will reflect only a fraction of incident near-infrared radiation as regular reflectance, while the remaining radiation will transmit through the surface. The internal cellular structure of the fruit may scatter part of the incident radiation into all directions and absorb a portion of the near-infrared energy at some wavelengths. If the internal cellular structure changes, the absorption varies. As a result, the near-infrared radiation reflected from a fruit changes accordingly at those absorption bands. For instance, when a bruise occurs, cell wall destruction and chemical changes in the fruit tissue may change the light scatter in the bruised area, leading to a difference in reflectance when compared to non-bruised fruit. Using a sensor to measure the reflected near-infrared radiation can provide information that indicates any changes of internal cellular structure, and that reveals the concealed quality beyond the surface of a fruit.

Applying NIR to detect defects on fruits and vegetables has become popular in the past few decades. NIR sensing systems have been used as non-destructive tool to detect bruises on apples (Tao, 1996), peaches (Miller et al.,1991), potatoes (Scanlon et al., 1999), etc. Because of the fast speed and relatively high signal-to-noise ratio, the NIR sensing system has been adopted by many fruit packing industries to improve efficiency and quality along high-speed fruit packing lines.

3.2.4 Mid-Infrared sensing and imaging Applications

Infrared spectrum ranging from 3 μm to 15 μm is generally considered as middle infrared or thermal infrared radiation, and has been widely used to measure emitted energy of objects. By using advanced optical detectors and electro-optic components, the emitted energy can be converted to a temperature indicator for targets of interest. The relationship between the radiation intensity and the object surface temperature is described by the Stefan-Boltzmann law as follows:

$$E = s e T^4 \quad (3.3)$$

where E is the radiation intensity of an emitter; s is the Stefan-Boltzmann constant ($5.7 \times 10^{-8} \text{ W/m}^2\text{K}^4$); e is emissivity, a material property of the object, which is often available in the literature; and T is the absolute surface temperature of the object. The intensity emitted depends on the fourth power of the surface temperature of the object.

Since every object emits the maximum IR energy at specific wavelength, the measurement of a particular material should require an IR sensor equipped with the appropriate optical assembly and infrared detectors. For instance, a sensor operating

at 3.43 μ m can be used to optimize the measurement of surface temperature of polyethylene (Harrick, 1960), while a sensor operating at 5 μ m usually is suited for glass measurement (David, et al. 2002), and sensors operating at 1-micron are generally used to measure metals and foils (Register, 1998). Today, with the development of high quality optics, advanced microelectronics, and embedded software technologies, high-resolution, high-speed and high-accuracy infrared sensors have become available. For example, the high-performance InGaAs photon sensors have adjustable and calibrated emissive settings over 0.1-1.0 micron spectral resolution at a response time less than 1 millisecond and temperature measuring accuracy at 0.1 centigrade (Indigo Systems, 2000). Thus, high speed online sensing and imaging applications with the high performance thermal infrared sensors are becoming popular. For instance, thermal infrared imaging has been used for quality inspections including examination of insulation settings, detection of moisture damage, verification of concrete integrity, evaluation of possible heat loss, searching for cooling system energy leaks, etc on residential buildings, plants facilities, and refineries. It has long been a successful tool used by the military and law enforcement agencies. The applications extend to day/night border patrol, coast surveillance, contraband detection, night vision, search and rescue, etc. Thermal infrared imaging has also recently been utilized in such medical applications such as blood flow vascular scan, blood circulation imaging, cancer research, exercise or therapeutic massage verification, etc.

The non-contact characteristic of thermal infrared imaging is another important advantage, especially for the measurement of the surface temperature on

cooked and other food materials. The nondestructive, high-speed, automatic monitoring and accuracy make mid-infrared imaging the preferred method in food inspection industries. Since traditional temperature sensors could not be applied in microwave heating, Goedecken et al. (1991) introduced a thermal infrared imaging method to continuously monitor the surface temperature of food in a microwave oven. Cuccurullo et al. (2002) proposed a technique using IR thermography to measure the surface temperature of a microwave oven. Fang and Shah (1998) used thermal IR imaging to investigate the heat transfer through air/water and oil/water interfaces. Their objective was to investigate the effect of surfactant monolayers on the heat transfer process through the interfaces. Ibarra et al. (1999) developed a method using IR imaging to estimate the internal cooking temperature in chicken breasts.

The thermal IR imaging technique has also been used to assess the ripeness of fruits. In an early work, Danno et al. (1980) used an IR vidicon camera to measure the surface temperature in fruits for evaluation of the grade of maturity. Based on the analysis of thermal infrared images, Hellebrand et al. (2001) explained that the transpiration process was related to the surface temperature changes of fruits, and the maximum value of transpiration resistance coincided with the stage of ripeness. One important work on apple defect detection using infrared thermal imaging was conducted by Varith et al., 2001. The difference in thermal conductivity, specific heat, thermal diffusivity, and emissivity between bruised and sound tissues caused divergent surface temperatures (Varith et al., 2001). Varith et al. used a ThermaCamTM PM390 in their experiments and indicated that, in bruises, thermal

diffusivity is 14.3% higher than in sound tissues, and yielding about 1-2⁰C higher during 30-180 second after the beginning of heating (Varith et al., 2001). After this period, the surface temperature of bruised or sound tissues reached thermal equilibrium. They found that it was easier to detect the bruises using a heating treatment than a cooling treatment. However, Varith et al. (2001, 2003) was more focused on studying the possibility of using infrared thermal imaging to detect bruised issues and touched little on other persistent problems that occur during online apple defect inspection.

3.3 On-line Automated Defect Detection of Apples

3.3.1 On-line System Requirements

According to a recent National Agriculture Statistics report, in the past ten years (from 1994 to 2003), the United States produced an average of \$1,540.7 million worth of apples each year, while the fresh market accounts for approximately \$885 million (USDA, 2004). In fact, the unit price of apple has continuously increased during the last four years. Taking statistical data from 2002 as an example, the fresh market utilized 5366.2 million pounds of apples, about 62.9% of the total production of that year. With a unit price of 18.8 cents per pound, the fresh market value exceeded \$1,000 million (USDA, 2004). This means every 1% increase of good apple inspection accuracy could produce a nearly \$10 million payback for the apple industry.

In the industry, fresh produce like apples must go through numerous processing steps such as cleaning, sorting, and packing to enhance their quality and shelf-life before they are shipped to the consumer market. A typical apple packing

line can be divided into various processing stages, including dumping apples into water flow tank, clearing, waxing, and drying the apples, applying electronic inspection to apples by size, weight, color and shape, selecting apples with defects, and at last packing the apples into bags. Among those operations, except for the defect inspection process that requires human inspectors, other processes are automatically done by packing machines. Apple defects can be divided into more than ten categories: alternaria blotch, scab, rot, pox, spot, rust, flyspeck, hail injury, powdery mildew, blotch etc (Biggs, 1999). Some defects are not easy to accurately classify or be recognized by untrained eyes. Moreover, the huge number of apples passing through the packing lines have posed considerable difficulties for human inspectors, which could lead to significant inspection error.

3.3.2 Challenges for on-line system design

There is a strong demand for cost-effective automated defect detection equipment to increase the defect detection accuracy and throughput in modern apple packing houses. In the early 1970, Stiefvater (1970) summarized that reliable identification algorithms, non-destructive sensing, and high speed sorting are three criteria for detecting defects and bruises of apples. Since 1970s, much work has been performed in the area of defect detection. Brown and Segerlind (1970, 1974, 1975) began using a near-infrared reflectance method to detect bruises on apples. In US Patent No.3.867.041, they compared lights reflected from bruised and unbruised portions of apples and found that in the near-infrared spectrum, the reflected light from the bruised portion was much weaker than that from the unbruised portion. From then on, using optical techniques to detect apple defects became popular.

Although other sensing techniques like X-ray (Diener et al., 1970; Schatzki et al., 1997), nuclear magnetic resonance (NMR) (Chen et al., 1989), and thermal infrared (Varith, 2001) have been explored, near-infrared sensing is the dominant method used in the past three decades.

With rapid advances in optics and computer technology, use of image sensors and digital computers for automatic defect inspection has grown into a particularly active research area. Graf (1982) used a “matrix camera” to record apple images. Tylor, Rehakugler and Throop (1983, 1986, 1989) used digital line-scan cameras to detect apple defects. Digital frame grabbers were adopted later (Heinemann et al., 1995; Tao et al., 1995; Wen and Tao, 1997). The advantages of using digital imaging systems for apple defect detection are that those systems are fairly accurate, consistent and nondestructive (Chen et al., 2002). Nevertheless, with the abundant apple images, effective computer algorithms dedicated to identify defective apples from good ones have become the focus of many studies. Image analysis algorithms such as image enhancement (Slaughter et al., 1986), feature extraction (Sarkar et al., 1985; Pla et al., 1993), statistical classification (Shahin et al., 1999), and neural network classification (Bochereau, 1992). have been applied in apple defect inspection or similar areas.

Satisfactory detection accuracy and effective image processing algorithms have led to the development of online real-time systems. In the middle 90s, Crowe and Delwiche (1996a, b) published a real-time hardware and software solution for a prototype apple bruise detection machine. From then on, practical challenges have become major topics in this research field. As Tao (2001) indicated, in practice a high

performance automated apple defect detection system requires: 1) complete surface examination of each fruit; 2) high inspection rate of 10 fruit per line per second or higher; 3) sophisticated segmentation and classification algorithms with adequate accuracy to distinguish defects; and 4) stems and calyxes of apples must be distinguished from true defects. Special algorithms have been developed to solve practical problems encountered in apple inspection. For instance, the non-uniform intensity distribution due to the spherical geometry of the fruit has caused high detection error rates. Tao (1996, 1998) developed a “spherical transformation” algorithm to successfully eliminate the “annoying” effect on apple reflectance images caused by the curved surface of the fruit.

Another example of practical challenges is the complete surface inspection problem. In order to guarantee a complete surface coverage of each apple online, special mechanical conveying equipments and imaging system are required. Laykin et al. (1999) presented a prototype using a specially constructed “wire-frame” cups to carry the fruit. They applied three cameras to capture three different views of one fruit simultaneously. Therefore, most of the surface areas of the fruit can be scanned. The drawback of this method is the fixed structure of the “wire-frame” cup, which might not be suitable for possible various shapes and sizes of fruit, must be eliminated in the three-view images. The typical mechanical conveying solution in this case is to use roller conveyors. Bi-cone rollers (Crowe and Delwiche, 1996a) were used to rotate the fruits as they are moving along the conveyor. The roller conveyors have been widely accepted by the industry and have been constructed flexibly into single (Crowe and Delwiche, 1996a) and multiple lanes (Tao, 1996).

Currently, the major challenge in practical apple defect detection is how to distinguish defects from stem-ends and calyxes. Automated surface blemish detection systems for apples can be confused by the stem, calyx and concavities of the fruit. If the stem and calyx are incorrectly classified as blemishes or bruises, a false identification will occur.

Various approaches have been investigated into this persistent problem. Wolfe and Sandler (1989) reported a stem detection algorithm, which utilized the prominent and concave shapes of stem-ends and calyxes. However, this method could be ineffective if a clear side view of the stems is not available. Other researchers (Miller and Drouillard, 1997; Davenel et al., 1988; Throop et al., 1997) utilized mechanical systems to orient the fruit, so that the stems and calyxes were at known positions. For these methods, the fruit position (as it appears within the field of view of the cameras) on the conveyor was critical to the final recognition process. If the positions were fixed or known to the imaging system, optimal performance could be achieved. However, on a typical packing line, fruits are found in random positions. It is impossible to predict the exact positions of each fruit when they are passing the camera. Due to the randomness of the fruit orientation, it is more difficult when scanning multiple apples in the viewing area. Campins et al.(1997) concluded that it is impossible to use mechanical orientation methods to solve the problem for *all* apple inspection in real-time systems. Other approaches were needed to solve the problem. Similar solutions to other fruits were presented. Miller and Delwiche (1991) approached a similar problem related to automatic fresh peaches grading. The surface cavity of a peach was identified using the variance of gradient within a region of

interest. The reported classification error rate for identifying the stem-end of peach as a defect was about 30%. Outline views have been used to determine the orientation of oranges, blueberries and peppers (Pla and Juste, 1995; Wolfe and Sandler 1985), but in apple detection, it was difficult to locate the accurate positions of stems and calyxes through different views.

Another technique was to use structured light to detect the 3D shape of apple surfaces (Yang, 1996; Graydon, 1999; Penman, 2001). The concavity of stems and calyxes could be identified by calculating laser light stripes. Actually, the light stripes showed not only the concavity, but convexity and occlusions as well. This method implied potential problems: 1) the intensity and density of stripe lights was hard to control; 2) the orientation of stems and calyxes could affect the efficiency of the 3-D information calculated through laser projection of stripe lights; 3) even if the laser stripe lights could locate the stems and calyxes perfectly, bruises and blemishes could not be identified by laser beams. In this approach, additional sensing devices (near-infrared sensors) for defect detection were required. It could raise other difficult problems such as system synchronization, target tracking, and image registration; and 4) it might not be suitable for multi-lane real-time implementations.

Wen and Tao (2000) developed a NIR/MIR dual-camera imaging method to identify the stem-end and the calyx in apple defect detection. In their study, a middle infrared spectrum ranging from 3.4 μm to 5 μm or 8 μm to 12 μm were proved sensitive to stem-ends and calyxes but not to true defects, while the NIR camera, ranging between 700 and 1000nm was sensitive to both true defects and stem-ends and calyxes of apples. Both MIR and NIR images were taken for each apple at the same

time. True defects were extracted by combining the two images. They reported a 100% detection of good apples, 99.34% of calyxes, 98.86% of stem-ends and 96.67% of defective apples. However, the effectiveness test was conducted in offline apple detection. For automatic online implementation of apple sorting, system integration and image processing techniques need to be developed to meet the requirements for real time packing lines.

3.4 Machine Vision System

Machine vision is an engineering technology that combines mechanics, optical instrumentation, electromagnetic sensing, digital video and image processing technology. As an integrated mechanical-optical-electronic-software system, machine vision has been widely used for examining, monitoring, and controlling a very broad range of applications. Graves and Batchelor (2003) summarized more than 20 machine vision applications that were classified by tasks in the natural product industry, more than 15 in manufacturing industry, and 7 other machine vision tasks applied to various situations such as security and surveillance, medicine and health screening, military, and traffic control and monitoring.

One of the most significant challenges to machine vision engineers on natural product inspection is the product variability. Unlike the manufactured parts encountered in many industrial applications, natural products have different sizes, shapes, colors, and textures in the captured images, and the defects on the products vary in terms of severity and location (Graves and Batchelor, 2003). These variability problems, among other challenges, should be addressed in the design of a machine

vision system by an integrated solution of optical, electrical, mechanical and algorithmic approaches.

3.4.1 Machine Vision as a controlled system

A successful machine vision system should be reliable, fast, and consistent. As an engineering technology, machine vision is focused controlling and optimizing the image sensing process, maximizing available useful information, and easing the subsequent image processing tasks. On the tradeoff of performance and speed, machine vision engineers tend to push for maximum throughput as long as the system performance is satisfactory according to certain criteria, such as a better error rate than human inspectors (Chen, 2003). In a typical machine vision system, everything should be under control and well designed.

The mechanical design for a specified machine vision system usually is uniquely structured to suit the inspection of a particular product. For instance, the conveyor belts in a poultry bone detection machine vision systems are usually flat, with no texture, and made of USDA approved plastic materials (Chen, 2003; Jing, 2003). While prototype machines for chicken defect and disease inspection in the chicken plants use hooks to hold the birds when they are dangling from moving chains and passing through light beams (Chao et al., 2000). On the other hand, most conveyor belts for a modern apple packing line are roller conveyors made of special dark colored rubber (Tao, 1996).

The lighting system, a critical part of a controlled machine vision system, much be carefully designed. The ultimate purpose of lighting design is to provide a

consistent scene eliminate the appearance of variations, and yield appropriate, application-specific lighting. Proper selection of lighting sources (incandescent, fluorescent, halogen, Xenon, LED), lighting arrangements (backlighting, front lighting, side lighting, structured lighting, ring lighting), and lighting geometry (point lighting, diffuse lighting, collimated lighting) is the “key to value” (Zuech, 2004).

Primary factors that influence the selection is whether the object under inspection is: 1) flat or curved; 2) absorbing, transmissive or reflective; and 3) the nature of the feature to be imaged in comparison with the background. For instance, backlighting is usually used for detecting objects that are translucent, such as hatching eggs (Das and Evans, 1992) or used to measure the geometric dimensions of obscured object, such as measuring the shoot height or root diameters of pine to estimate the pine seedlings (Wilhoit et al., 1994). The side light scatter can be used to determine the cellular granularity (Jain et al., 1991). Structured light can be used to form a 3-D shape of apple surfaces for stem/calyx detection (Yang, 1993). Moreover, controlled lighting design sometimes acts as an active sensing means that can “create” new information. Laser stripes of structured lights combined with X-ray imaging on deboned chicken meat inspection is a successful example of generating “extra” information in machine vision systems (Chen, 2003; Jing, 2003).

Because of a controlled lighting system design, intelligent image processing technology applied to a machine vision system is normally simplified and can achieve high accuracy. Those algorithms tend to maximize the utilization of pre-obtained object properties such as the appearance, geometry, surface issues, shape, size, color, and positions, as well as the effect of lighting sources. Compared with computer

vision research in uncontrolled imaging environments, machine vision systems in controlled environments benefit from greatly simplified problems like image segmentation, classification, occlusions, and image registration. For instance, the rule-based decision-making method, which is quite effective under controlled condition (Bartlett, 1988), is rarely used in the computer vision pattern recognition field due to uncontrolled possibilities. In short, a major key to a successful machine vision application is to start with a good contrast, repeatable image that is not affected by ambient light or the surroundings.

3.4.2 Machine Vision as a Real-Time System

Real-time capability is an essential requirement in many machine vision applications. It is essential for the processing system to respond to the incoming image data in a timely manner, in particular, for synchronized multi-sensor systems. Missing a single line of image sometimes may cause image registration or hardware synchronization problems in the system. Laplante and Stoyenko (1996) summarized that real time imaging systems involves three major tradeoffs: performance versus image resolution, performance versus data bandwidth, and synchronization versus number of concurrent tasks. They pointed out that besides adopting faster hardware, using appropriate software architecture is usually more important to ensure reliability and functionality of the overall system, and to maximize the potential of the available hardware. The design of appropriate software architecture emphasizes the re-usability of shared resources between concurrent tasks and intermediate results. However, most of these techniques require special control in lower level software architecture. By far,

in most machine vision applications useful techniques such as double buffering and parallel processing are popular (Chen, 2003; Jing, 2003).

Double buffering is an image processing technique using two image buffers to ensure data integrity without interfering with real-time image acquisition. The basic idea of double buffering is similar to queuing techniques in computer engineering. Two image buffers are assigned, one of them is used for new image grabbing while the other is used for processing, and the two buffers work in an interlaced manner. It requires that the maximum processing time for one frame is shorter than the minimum acquisition time for a frame; otherwise, the image data being processed could be contaminated. Handshaking signals are used to indicate the current status of buffer processing. This simple mechanism guarantees that at any time, the image buffer being processed is not being updated by another source, thus data integrity is ensured.

To maximally exploit the hardware computing power, it is often helpful to process the images in a parallel manner. Parallel processing refers to the concept of speeding-up the execution of a program by dividing the program into multiple fragments that can execute simultaneously, each on its own processor core. In a typical real-time multi-processor imaging system, data throughput is affected by the following factors: 1) the acquisition frame rate of the sensor and the image grabber and processing speed of the onboard image processor if there is one; 2) data bandwidth for transferring the image stream to the host CPU(s); 3) processing speed of the host CPU and data bandwidth between CPU and memory. Relatively slow data transfer speed in the data buses usually causes a “bottleneck” effects in image

processing. Multi-thread and parallel processing over several processors may release the bottleneck crisis and use the idling time slots on the host CPUs or onboard processors. Computation power of the onboard processor and host CPU can be employed more efficiently if there are multiple processing threads working in parallel, and the overall throughput and responsiveness of the overall system would be improved with the same hardware.

3.4.3 Future Trends of Machine Vision

A typical machine vision system consists of one or more optical sensors, illumination sources appropriate for the specified sensing, a necessary mechanism for presenting the objects, one or more image digitizers to acquire images, and one or more digital image processors or computers to process data. With the development and integration of modern mechanic, electronic, computer and sensing technologies, traditional components of a machine vision system have been advanced along many fronts. Computer processor architecture has been improved dramatically. Very long instruction word (VLIW) architecture has been applied in media and image processor, where the instruction-word length has increased, so that multiple operations can be executed in a single cycle. The VLIW processors are usually configurable and optimized for targeted compact system, and are suitable for most data-centric applications with high performance and low cost (Managuli and Kim, 2002; Bae et al., 2002). The sensitivity and resolution of cameras have increased. New sensing instruments such as uncooled infrared cameras are now commercially available. With the development of VLSI design, computational sensors have emerged. Analog and

digital integrated circuits that are sensitive to measure the outside stimulus (such as light) are designed, and algorithms that are developed to mimic one aspect of a biological system (such as vision) are integrated into one single chip. Computation and sensing are tightly combined to achieve a miniature, self-contained, autonomous, and intelligent sensing system (Brajovic, 2004; Brajovic and Kanade, 2004). The micro-electro-mechanical systems (MEMS) sensor industry has made continuous improvements to develop reliable and low cost “sensors on chip” systems (Motorola, 1998; Shaw, 1998). Moreover, many recognition and tracking algorithms have been developed from 3D image matching to artificial neural networks. Technologies, such as wireless communication, and modern control techniques have been included in machine vision systems, arose from applications in biomedical engineering (Daumas et al., 2003; Chauhan et al., 2003; Raczkowsky et al., 2003), industrial control (Toyserkani et al., 2003;), home robotics(Bonizzi et al., 2003; Acosta et al., 2003), and agriculture (Martín-Herrero et al., 2003; Dunn et al., 2003).

In the inspection of natural products such as vegetables, fruits and other biological materials, the differences in the characteristics of light absorption by the materials are very important (Chen, 2003). A hyperspectral imaging technique that combines the advantages of spectroscopy and imaging techniques will have many potential applications in the fresh produce inspection industry.

3.5 Hyperspectral Sensing and Imaging

3.5.1 Brief Overview

Hyperspectral Sensing and Imaging (HSI) exploits the fact that all materials, due to the differences of their molecular compositions, reflect, absorb, and emit electromagnetic energy in distinctive patterns at specific wavelengths. This characteristic is called *spectral signature*. In principle, the spectral signature can be used to uniquely characterize and identify any given material over a sufficiently broad spectral band (Shaw and Manolakis, 2002). Hyperspectral data/images acquired over selected wavebands consist of spectral information that may cover dozens or even hundreds of contiguous narrow bands for the purpose of signature analysis. The spatially and spectrally digitized information can be considered a three-dimensional data cube, with two-dimension of spatial coordinates and a third dimension of spectral band. The development of proper processing algorithms to analyze the high-resolution data cube has become the key to success of many hyperspectral sensing and imaging applications.

The processing algorithms can be organized into four types according to their tasks: target detection, change detection, classification and unmixing. Target detection means seeking a unique spectral signature that belongs to some object or material. The objective of change detection is to find the significant changes between two hyperspectral scenes of the same geographic region. The goal of classification is to label each pixel in a hyperspectral image into clusters of pre-specified types of categories (classes). Unmixing means evaluating the fraction of the pixel area covered

by each material present in the scene or decompose a mixed pixel into a collection of constituent spectra, which is typically used in remote sensing.

The typical procedures of HSI analysis include: 1) image display, which presents a view of the data set in an image space so that the analyst can explain and mark classes of data easily; 2) class definition, this operation is to identify the informational data into desired groups; 3) feature extraction, which applies algorithms to determine a feature subspace that is optimal for discriminating between specified classes defined. An initial set of data training is usually required; 4) reformatting. In this step, based on the feature subspace, a new data set is generated with reduced dimensionality; 5) initial classification. Classifiers are used to segment data cube into defined classes; 6) finalize training, which means to inspect the initial classification result and identify potential improvements. If needed, new features will be added to the training set; and 7) final classification. The step is to re-classify the data based on the new training set.

3.5.2 Optimal Band Selection and Combination Problem

Hyperspectral imaging has emerged as a powerful tool in earth remote sensing. Recently, it has also been utilized as a non-invasive inspection method in medical, biological, agricultural and industrial areas (Heitschmidt et al., 1998; Levenson et al., 1998; Lu and Chen 1998; Willoughby et al., 1996). Lu and Chen (1998) pointed out that only two or three essential spectral bands were required for on-line imaging applications to identify unwholesome conditions in food products. Kim et al. (2001) established a laboratory-based hyperspectral imaging system that combined the

features of imaging and VIS/NIR spectroscopy to simultaneously acquire spectral and spatial information for various food commodities. These studies suggest a need for defining the optimal bands spectral combinations for on-line inspection implementations.

The topics of band selection and combination are concentrated on establishing a formal methodology, which enables optimal utilization of specific spectral bands. In general, the selected band(s) should *reduce* the data dimensionality while *preserving* the most important information contained in the lower dimensional data space.

Hyperspectral band selection and combinations have become a powerful tool and gained enormous research interest for safety and quality inspection of fruit and poultry products. Lu and Chen (1999) used hyperspectral imaging to detect the bruises in apples; Kim et al. (2002a, 2002b) used the hyperspectral tool for fecal contamination detection on apples; Heitschmidt et al. (1998) used hyperspectral analysis for fecal contamination of poultry products; and Chen et al. (1998), Park (1998) and Windham (2001) demonstrated the methods of using VIS/NIR spectroscopy for detecting defects in chicken carcasses. The common aspect of these studies is that the PCA method is used for optimal band selection and band combination over the hyperspectral bands. The optimal band(s) is defined as the one(s) that preserves the most energy among the hyperspectral data cube. In other words, the selected band(s) presents the best representations of the original data.

However, in different applications, the definition of the “optimal band” varies. Accordingly, the method used in solving the band selection problem should vary too. For instance, in remote sensing applications, in order to obtain the optimal bands that

maximum the signal to noise ratio (SNR), modified PCA methods were used. Green et al. (1988) developed a maximum noise fraction method to maximally remove the noise in the selected band; Lee (1990) used a noise-adjusted PCA method to select the optimal band. The two methods, although with different names, are mathematically equivalent. Compared with the PCA, the results of the modified methods identified the optimal components with maximum SNR.

Therefore, in order to select the optimal band in hyperspectral analysis, the first step is to define 'optimality'. Casasent (2000, 2001) pointed out that the discriminating information of features was very important; therefore, minor components should be used for band selection and combination. Using the hyperspectral imaging system developed by USDA-ISL for most food safety and quality applications, the optimal band(s) should preserve both the information, if not equally, on data cube energy and on low probability objects, or unwholesome objects. The optimal band is accordingly defined as the band that contains the maximum information and simultaneously separates the different features maximally from the original data. Since the PCA method in no way guarantees that the resulting transformation will preserve the low probability object information, a modified method is proposed in this study to achieve better performance in satisfying the optimal band selection and combination criteria.

CHAPTER 4 A NOVEL INTEGRATED PCA AND FLD METHOD OF HYPERSPECTRAL IMAGE FEATURE EXTRACTION FOR CUCUMBER CHILLING DAMAGE INSPECTION

4.1 Introduction

Chilling damage to produce such as cucumbers usually happens when the produce are stored at low temperatures. The primary cause of the chilling damage is thought to be the injury of plant cell membranes (Saltveit and Morris, 1990). Chilling damage is a result of low temperature over time. Usually, chilling injury can be recoverable if the produce stays below the critical temperature for only a short period of time. But if exposure to the low temperature is prolonged, the damage is irreversible. Detection of chilling damage is difficult, especially at its early stages. The symptoms of injury usually develop after the produce is placed in a warmer environment. Sometimes symptoms develop slowly and are difficult to detect visually. In order to find an effective way to detect chilling injury for automated inspection of fruit and vegetables, a hyperspectral-imaging method is used.

Hyperspectral sensors have been used to sample the spectral reflectance from objects. The rich spectral response collected provides sufficient information to identify the spectral reflection peaks and absorbing troughs of material (Shaw and Manolakis, 2002). The entire spectrum region used for sensing spans from the visible region through the near infrared and is divided into hundreds of narrow and contiguous bands. The spectral interval can be as narrow as a few nanometers in

wavelength. As a result, over 100 spectral bands or channels are usually used at the same time. By adding a dimension of spectral information to two-dimensional spatial images, hyperspectral data can be perceived as a three-dimensional data cube. Recently, hyperspectral imaging has become a powerful tool and is of enormous interest to researchers in fruit safety and quality inspection. Kim et al. (2001) established a laboratory-based hyperspectral imaging system combining the features of imaging and visible/near-infrared (Vis/NIR) spectroscopy to simultaneously acquire spectral and spatial information for various food commodities; Kim et al (2002a, 2002b) used hyperspectral imaging methods for fecal contamination detection on apples; Heitschmidt (1998) used hyperspectral analysis for fecal contamination of poultry products; and Chen et al, (1998), Park (2002) and Windham (2001) showed methods of using hyperspectral imaging for detecting contamination of chicken carcasses.

Lu and Chen (1998) found that only two or three essential spectral bands were required for on-line imaging applications to identify unwholesome conditions in food products. Hyperspectral imaging is used as a research tool to determine those essential bands. All the spectral data is studied. Band selection and combination strategies are applied. Because in commercial systems applications, two or three spectral bands are usually required for real-time inspection, the validity of the band-selection and combination strategy identified by hyperspectral sensing research becomes important. The selected essential bands should not only maintain any valuable details that are needed, but also simplify the successive discrimination and

classification procedures. This research is focused on developing a band combination method that can be applied to hyperspectral research on fruit and vegetable inspection.

A hyperspectral image cube can be considered as a high dimensional feature space. Each feature is represented as a spectral image, and the reflection properties from wholesome and unwholesome objects are associated as different patterns. The hyperspectral band selection problem then can be viewed as a feature extraction problem in statistical pattern recognition. The well-known linear transforms or projection pursuit methods for feature extraction and dimensionality reduction are principal component analysis (PCA) and linear discriminant analysis (LDA). PCA is widely used in fecal-contaminated apple inspection (Kim, 2002) and quality and safety inspections of other fruit and vegetable. However, Talukder and Casasent (1998) point out that PCA, as an unsupervised method, is not necessarily good at drawing distinctions between patterns. In this paper, the objective is to present a new method that combines the PCA and the Fisher's Linear Discriminant (FLD) methods to aid in the criteria development for selecting spectral bands for multispectral imaging applications. This new method and the individual PCA and FLD methods are each applied to cucumber chilling injury inspection. The detection results obtained by using the new method are presented and compared with PCA and FLD, respectively.

4.2 Material and Method

4.2.1 Sample Materials

Cucumbers were freshly picked from a farming field. Ninety cucumbers were divided into 30 groups of 3 cucumbers each. Each group was placed in a plastic bag punched with holes to allow for air circulation. In temperature-controlled cold storage rooms, fifteen of the bags were stored at 0°C and the other fifteen at 5°C. On each day over a period of 15 days, one bag was moved from each cold storage room to an air-conditioned laboratory room at 18-20°C. Each day, hyperspectral images were collected for the 6 (2 groups of 3) newly-moved cucumbers, and also for all cucumbers previously moved from the cold storage. The last two groups were moved after 15 days in cold storage and image collection continued for 6 days afterwards. Chilling injury was categorized into four different damage levels: trace, slight, moderate, and severe. For cucumbers stored at 0°C, symptoms of trace chilling injury first appeared on cucumbers that had spent 4 days in cold storage and then 2 days at room temperature. For cucumbers stored at 5°C, symptoms of trace chilling injury first appeared on cucumbers that had spent 5 days in cold storage and 1 day at room temperature. Early trace and slight chilling injury was observed. Some cucumbers that showed early trace and slight levels of chilling damage subsequently appeared to recover after several days at room temperature. Typical samples of these injury levels are shown in Figure 4.1. The dark spots on the cucumber images in Figure 4.1(c) and (d) represent the severe skin damage and decay developed from chilling injury.

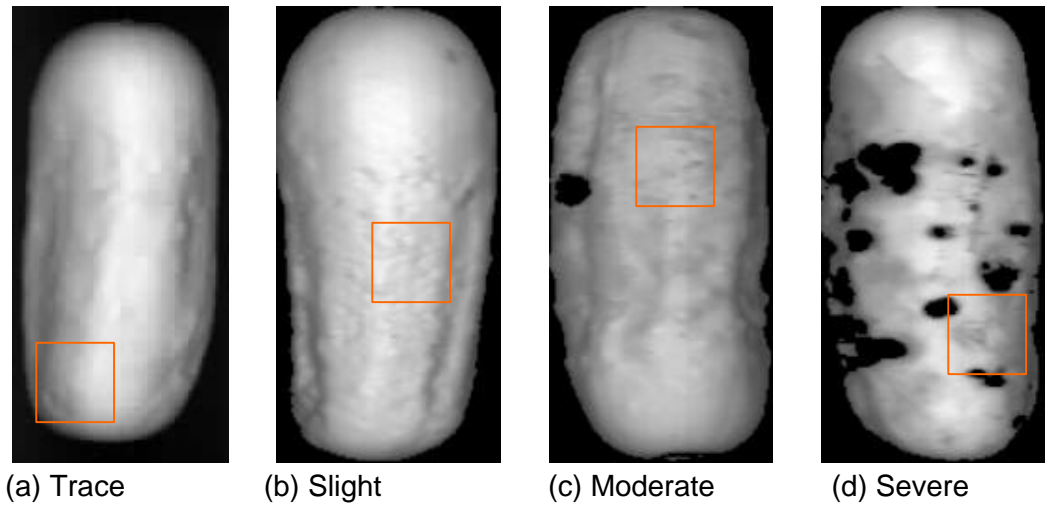
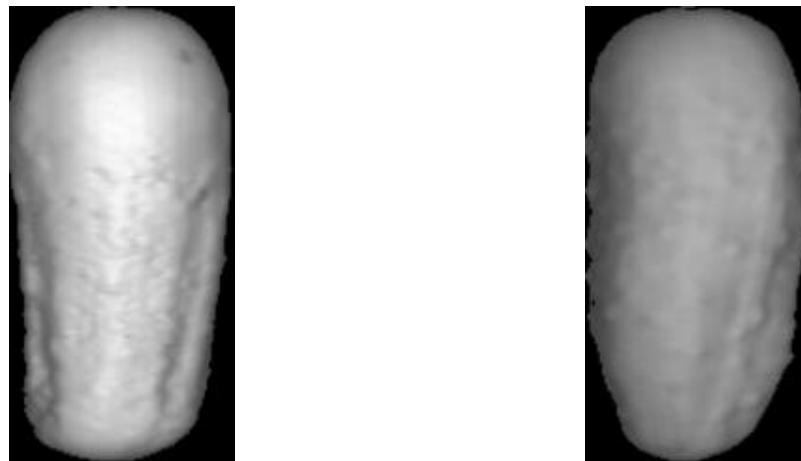


Figure 4.1 Four levels of chilling injury (presented in the rectangular area) of cucumbers detected in this study. (a) trace chilling injury (b) slight chilling injury (c) moderate chilling injury (d) severe chilling injury. The images used were 800nm near infrared image.



(a) slight chilling damaged cucumber (b) bumpy good cucumber

Figure 4.2 The NIR reflectance images of a slightly chilling damaged cucumber and a good one with bumpy skin. The two images show the similarity in appearance of the two cucumbers. The images were taken at 800 nm. (a) A cucumber with slight chilling damages (b) A healthy cucumber with bumpy skin.

A large degree of variation in both color and skin smoothness can exist between individual cucumbers. These natural differences increase the difficulty of detecting chilling damage even during the human visual inspection process. For instance, bumpy skinned cucumbers can be easily mistaken to have trace or slight chilling damage due to the visual similarities, as shown in Figure 4.2. It had become the most challenging part of our experiment for effective detection. On the other hand, the cucumber samples also varied in sizes and shapes in their hyperspectral images. In order to keep the input data consistent, only a portion of each cucumber image was used for the input image samples. The size of the region of interest is 45 pixels by 45 pixels. This size covered the average spot area of chilling damage. For an individual cucumber sample, the different levels of chilling injury may appear on different portions of the cucumber skin and thus may produce different image samples for training or testing purposes. Data collected for the 90 cucumber samples during three weeks' time provided a huge number of input image samples. Moreover, since the cucumbers developed different types of chilling injuries unevenly, different numbers of samples were chosen for training and testing of the algorithms, as summarized in Table 4.1. Three experiments were conducted on testing different methods with different types of cucumber samples.

Table 4.1 Cucumber Sample Diversity

Sample class	Number of sample images	Type of cucumbers	Total number of sample images
<i>Defective Cucumber Samples</i>	20	<i>Trace</i>	140
	50	<i>Slight</i>	
	35	<i>Moderate</i>	
	35	<i>Severe</i>	
<i>Good Cucumber Samples</i>	90	<i>Good with bumpy skin</i>	140
	50	<i>Good smooth</i>	

4.2.2 Hyperspectral Sensing System

A laboratory-based hyperspectral sensing and imaging system established by the USDA Instrumentation and Sensing Lab (ISL) was used to scan each sample. For a detailed description of this equipment, please refer to Kim et al (2001, 2002a). In this study, only reflectance measurements were analyzed. The illumination for reflectance imaging was provided by two 150 W halogen lamps. The equipment was operated in a line-by-line scan mode at a line length of 460 pixels. The scanned wavelengths ranged from 447.3 nm to 951.2 nm with a 4.5 nm interval, for a total of 112 spectral bands. Once a single line was scanned, a 112x460 (spectral by spatial) pixel image was generated. Due to the maximum length of the cucumber samples, 300 lines were accumulated for each cucumber. During the scanning process, the system was operated in a darkened room to prevent interference from ambient light.

Each pixel value in the 1x112 spatial-by-spectral image is proportional to reflectance factors of the sample at that pixel position. The reflectance factor was defined by dividing the reflected radiation intensity at each pixel position of a sample

by that of a known reference under the same illumination situation. For system calibration, a white Spectralon panel (Labsphere, Inc.) with nearly 99% reflection ratio was used as the reference. To obtain a proper dynamic range of the image data, the reflectance factors were expanded by a fixed number and then assigned to be the pixel values of the spatial by spectral image.

4.2.3 Feature Extraction with Integrated PCA-FLD Method

Principal component analysis (PCA), also known as the Karhunen-Loeve transform, uses orthogonal axes for dimensionality reduction by performing an eigen-decomposition of the spectral covariance matrix of the data. Let S_t represents the covariance matrix, and S_t can be obtained by:

$$S_t = \frac{1}{N} \sum_{k=1}^N (x_k - \mathbf{m})(x_k - \mathbf{m})^T \quad (4.1)$$

where \mathbf{m} is the mean vector of a pixel set, and N is the sample size. The dimension of S_t is $N \times N$. The eigen-decomposition transform is to maximize the energy of the projected samples, denoted as:

$$E_{\text{pca}} = \mathbf{f}_m^T S_t \mathbf{f}_m \quad (4.2)$$

where, \mathbf{f}_m is the one of the transform vectors that was used to project the data samples, and $m=1 \dots N$. Each eigenvector corresponds to a unique combination of bands and the set of eigenvectors is orthogonal. By performing the eigen-decomposition of the covariance matrix, it can be demonstrated that the transformed data, compared with the original data, has minimized residual mean square error. More specifically, the

first eigenvector corresponding to the largest eigen value, explains more of the variance of the data than any single band of the original image. Similarly, the first two eigenvectors explain more of the data's variance than any pair of the original bands, and so on for large number of eigenvectors and bands. The magnitude of the eigenvalue indicates the energy residing in the data along the direction parallel to the corresponding eigenvector. The larger the eigenvalue, the higher the energy it represents. Hence, to reduce the original N-dimensional data to a lesser dimension, M, one can project the original data to the M eigenvectors corresponding to the largest M eigenvalues. By taking the first few significant compositions, this transform results in a lower-dimensional multivariate feature vector, that still preserves most of the energy in the original, higher-dimension system.

Fisher's Linear Discriminant (FLD) method is an effective, class-specific method that projects the scatter of data to make them more reliable for classification. Two matrices are introduced in the FLD: one is the between-class scatter matrix, denoted as S_b , and another is the within-class scatter matrix S_w . The between-class scatter matrix S_b is defined as (Belhumeur et al., 1997):

$$S_b = \sum_{i=1}^c |c_i| (\mathbf{m}_i - \mathbf{m})(\mathbf{m}_i - \mathbf{m})^T \quad (4.3)$$

and the within-class scatter matrix is defined as:

$$S_w = \sum_{i=1}^c \sum_{x_k \in c_i} (x_k - \mathbf{m}_i)(x_k - \mathbf{m}_i)^T \quad (4.4)$$

where \mathbf{m}_i is the mean vector of class i, \mathbf{m} is the mean of total samples, c is the number of classes, c_i represents the ith class and $|c_i|$ is the number of samples in class

i. The optimal data projection can be obtained by choosing the transform-vectors \mathbf{f}_m that maximizes the ratio of the projected between-class samples to the projected within-class samples, denoted as E_{fld} , and defined:

$$E_{\text{fld}} = \frac{\sum_{m=1}^M \mathbf{f}_m^T S_b \mathbf{f}_m}{\sum_{m=1}^M \mathbf{f}_m^T S_w \mathbf{f}_m} \quad (4.5)$$

Note that the PCA method does not guarantee the representation of the feature class separability of the selected band. On the other hand, the FLD method, though is effective in class segmentation, is sensitive to noise and may not convey enough energy from the original data.

In order to design a set of transformation vector-basis that can provide supervised classification information well, and at the same time, preserve enough energy from the original data cube, a new method is proposed to combine the equation (4.1) to (4.4) to construct an evaluation equation called Integrated PCA-FLD Method. A weight factor K is introduced to adjust the degree of classification and energy preservation as desired. The constructed evaluation equation is given as:

$$E_{\text{evl}} = \frac{\sum_{m=1}^M \mathbf{f}_m^T [KS_t + (1-K)S_b] \mathbf{f}_m}{\sum_{m=1}^M \mathbf{f}_m^T [KI + (1-K)S_w] \mathbf{f}_m} \quad (4.6)$$

where $K \in [0,1]$, and \mathbf{I} is the identity matrix. In equation (4.5), if the within scatter matrix S_w becomes very small, the eigen-decomposition becomes inaccurate. Equation (4.6) overcomes this problem. If the previous situation happens, by adjusting the weight factor K toward 1, the effects of S_w can be ignored, which means the principal components are more heavily weighted. On the other hand, if the K value is chosen small, which means more differential information between classes is

taken into account, the ratio between S_b and S_w dominates. The integrated method magnifies the advantages of PCA and FLD and compensates the disadvantages of the two at the same time.

In fact, the FLD and PCA methods represent the extreme situation of equation (4.6). When $K=0$, only the discrimination measure is considered, and the equation is in fact equal to FLD (equation (4.5)). If $K=1$, only the representation measure is important, and the evaluation equation is equivalent to PCA method (equation (4.2)). To find the transform that provides equally well on representation and discrimination, one can find the set of \mathbf{f}_m that maximizes equation (4.6) where $K=0.5$. The solution of \mathbf{f}_m is called the generalized eigenvector that was obtained by setting the derivative of equation (4.6) with respect to \mathbf{f}_m to be zero. We have,

$$\left(\frac{KS_t + (1-K)S_b}{KI + (1-K)S_w} \right) \mathbf{f}_m = \mathbf{I}_m \mathbf{f}_m \quad (4.7)$$

Where, λ_m represents the eigenvalues, and \mathbf{f}_m is the corresponding generalized eigenvector.

For the hyperspectral dimensionality reduction, suppose that the original feature space is with N dimensions, then the reduced M ($M < N$) dimensional features can be formed by selecting the M generalized eigenvectors corresponding to the M largest eigenvalues obtained from equation (4.7). Note that K value changes between 0 to 1, which shifts the weight between PCA and FLD. For a given K value, a maximized (6) is supposed to give an optimal projection on the original feature space. The projected samples become the best in representation and classification at the proportion determined by K . For any application, an optimal proportion between PCA

and FLD exists, and by searching the K value from 0 to 1, one can find the optimal K that achieves the best classification rate of the samples. The changes of the classification rate by different K will be discussed in the next section.

The transformation matrix T (NxM) is formed by selecting M generalized eigenvectors as the column vectors in the matrix. The linear transform is defined as:

$$Y = T^T X \quad (4.8)$$

Where X represents the original feature space with the given NxJ dimension. N represents the features and J is the sample size. Y is the transformed feature space with MxJ dimension. Y consists of the new features (or bands) that obtained from the linear combination of all the original features/bands for all pixels. Since T consists of M eigenvectors that are corresponding to the M largest eigenvalues, Y can provide a better classification and representation ability than any subset of M bands of the original data set X.

In this study, M=1 is chosen. Only the eigenvector corresponding to the largest eigenvalue of (7) is used in the feature extraction. In this case, Y represents a single feature vector (we call it the first principal feature vector) that is generated by linear combination of original N features by using the integrated PCA-FLD method. Similarly, by applying PCA or FLD method individually, one may obtain the first principal feature vector for PCA or FLD, respectively, wherein PCA the first principal feature vector is in fact the first principal component. Though the physical meaning of the first principal feature vector in the integrated PCA-FLD method is less clear, it may provide the best discriminative feature compared with any individual feature in the original N feature space.

All methods mentioned above aim to establish a good transformation matrix to define the similarity or difference among patterns. When the original hyperspectral data cube is transformed, spectral feature vectors are obtained for each image sample selected. A classifier is designed to determine the category of input image samples. For spectral feature vectors that belong to one image sample, both mean and standard deviation of the feature vectors are calculated. The ratio of the standard deviation over the mean is used as the numerical input variable to a k-Nearest Neighbor classifier algorithm. The k-Nearest Neighbor algorithm is used to determine the k samples in the training set that are closest to the X^{th} unknown sample in the testing set. Because patterns with similar attributes should be assigned to a same class, samples with closer ratios are classified as the same category. Therefore, if a majority of the k nearest neighbors belongs to the “good cucumber” class, then the X^{th} sample is classified as a good cucumber, otherwise it is classified as an injured one. We used $k=15$ in the classifier.

4.3 Results and Discussion

Figure 4.3 shows the averaged reflectance intensity over the wavelength curves for six types of cucumbers. The main difference lay in the visible range from 500 nm to 580 nm, and near infrared range above 700 nm (the visible range represents the color of cucumber pigment). As shown in figure 4.3, cucumbers with severe and moderate chilling injury had greater absorbance within this spectral range and were easier to distinguish from the wholesome ones. On the other hand, the cucumbers with trace or slight damages showed little difference from the healthy

cucumbers. In particular, over most of the spectral range, the curves of bumpy-skin good cucumbers were mixed together with those of trace or slightly injured cucumbers. It became much more challenging to differentiate them prior to band combination.

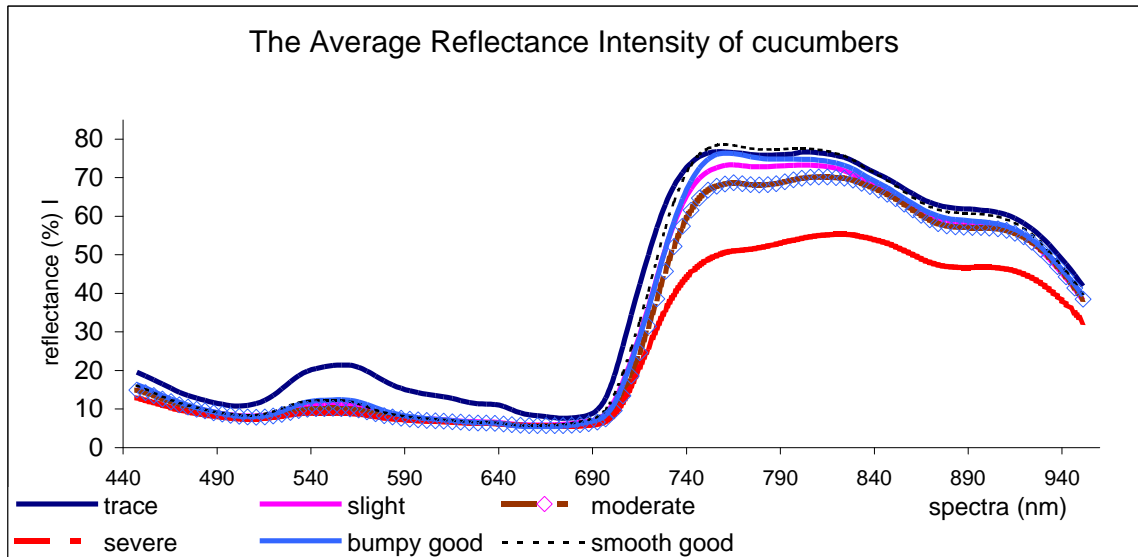
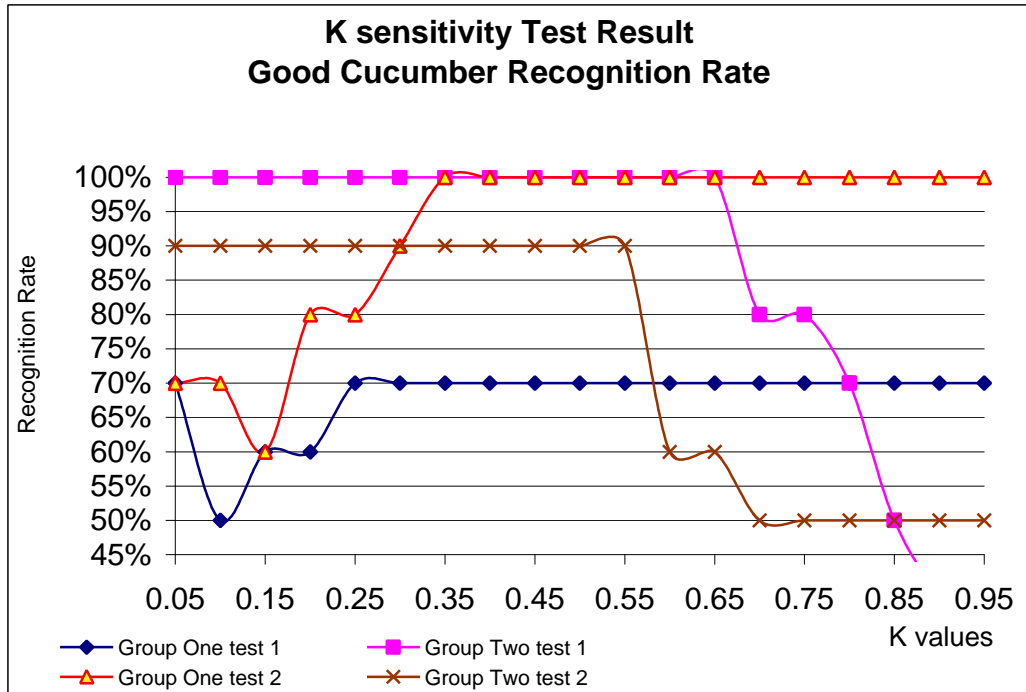
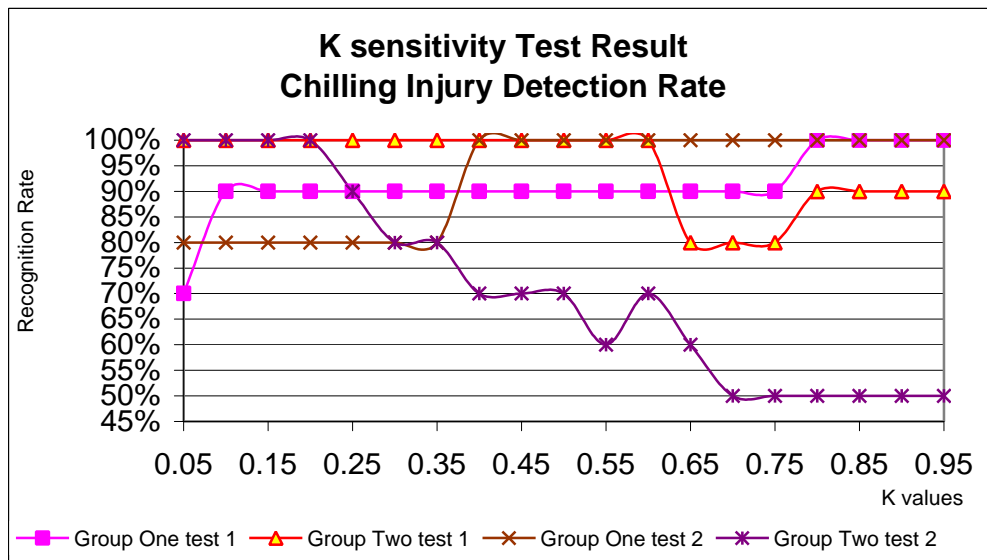


Figure 4.3 The hyperspectral reflectance effect on wholesome (bumpy good and smooth good) cucumbers and unwholesome (with chilling injury level of trace, slight, moderate, and severe) cucumbers.



(a)



(b)

Figure 4.4 (a) The good cucumber recognition rates versus K values for four evaluating tests, where each test used 20 different image samples. (b) The Chilling injury detection rate versus K values for the same four validating tests as in (a).

In the new method, the K value was used to adjust the balance between the representative and classification abilities of the projection matrix, and therefore increased the flexibility of the method. For different image samples, however, the optimal K values should differ. An effective method for K value selection was needed. In this study, we searched the K value from 0 to 1 at a step of 0.05. When the K value was changed, the recognition rates varied. As an example, figure 4.4 showed the sensitivity of K value versus the classification rates for two groups in a total of four tests using a small set of only 20 image samples. The samples used for the four tests are shown in table 4.2. The overall classification rate changed gradually over the K values. For different samples, the optimal K values differed. In group 1 tests, where the defective cucumbers were easier to distinguish from the good ones, the optimal K values were in the range of 0.35 to 0.95. In group 2 tests, since the two classes of image samples were similar, the optimal K values were in the range of 0.05 to 0.60. The overlapping range of optimal K was from 0.35 to 0.60. In most cases of this study, a K value in this range gave the best performance. But as shown in figure 4.4(b), in the test of detecting the trace-injured cucumbers from the bumpy good ones, the optimal K value was from 0.05 to 0.25. A K between 0.35 and 0.6 resulted in classification errors.

Table 4.2 Samples Used for Optimal K Value Tests

Sample Group	Test	Type of Cucumbers	Image Sample Total Number
One	Test 1	Moderate and smooth good	20
	Test 2	Severe and smooth good	20
Two	Test 1	Slight and bumpy good	20
	Test 2	Trace and bumpy good	20

In general, by choosing the optimal K values, both the representation and classification effects were properly weighted for the testing samples. The small set sample tests can be considered a validating process before the training and the testing process. Those image samples were called validating image samples, which were used to determine the variable parameters (in our experiments, the optimal K value) in the method before final application to the training and testing processes.

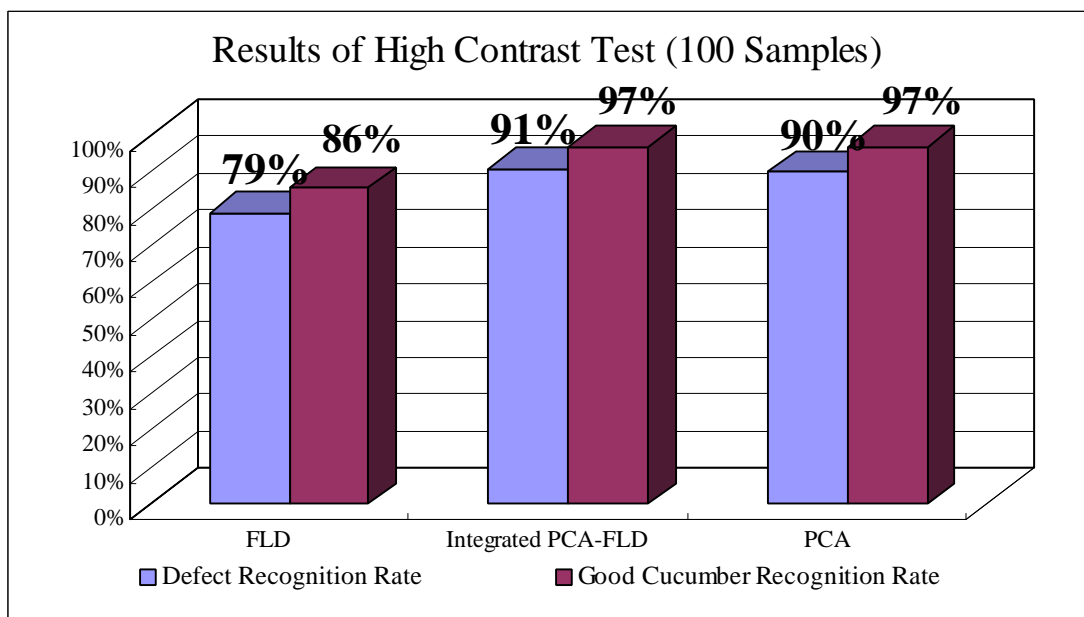


Figure 4.5 Chilling injury detection rates and good cucumber recognition rates were shown by using FLD, PCA and integrated FLD-PCA methods for the first experiment, where 20 image samples were used for training and the other 80 image samples were used for testing. The rates were calculated based on the total 100 testing cucumber image samples.

The image samples used for these experiments are listed in table 4.3. In the first experiment, 50 good smooth-skinned cucumber images and 50 badly injured (with moderate and severe degrees of damage) ones are selected. From among these, 20 good cucumber image samples and 20 injured ones are used for training and then tested together with the remaining 60 samples. The total 100-sample testing results

shown in figure 4.5 are obtained by choosing the optimal K value at 0.60. The result indicated that the PCA method and the integrated PCA-FLD method achieved a similar better performance compared with the FLD method. Note that the sample classes used in the first experiment were well separated ones. The solution was dominated by the principal components. So the PCA method becomes good at classifying data that are well distinguishable, and this is consistent with Kim's (2002) result. On the other hand, since FLD maximizes the E_{fld} ratio shown in equation (4.5), which is small in this case, it becomes unreliable and noise sensitive, and leading to the poor performance in this situation.

Table 4.3 Samples Used for the Experiments

<i>Experiment No.</i>	<i>Sample Type</i>	<i>Image Sample Num.</i>	<i>Training Set</i>	<i>Testing Set</i>
<i>High Contrast Test</i>	<i>Good smooth</i>	<i>50</i>	<i>20</i>	<i>50</i>
	<i>Moderate</i>	<i>25</i>	<i>10</i>	<i>25</i>
	<i>Severe</i>	<i>25</i>	<i>10</i>	<i>25</i>
<i>Low Contrast Test</i>	<i>Good with bumpy skin</i>	<i>30</i>	<i>30</i>	<i>30</i>
	<i>Trace</i>	<i>10</i>	<i>10</i>	<i>10</i>
	<i>Slight</i>	<i>20</i>	<i>20</i>	<i>20</i>
<i>Mixed Contrast Test</i>	<i>Good with bumpy skin</i>	<i>60</i>	<i>20</i>	<i>40</i>
	<i>Trace and Slight</i>	<i>40</i>	<i>10</i>	<i>30</i>
	<i>Moderate and Severe</i>	<i>20</i>	<i>10</i>	<i>10</i>

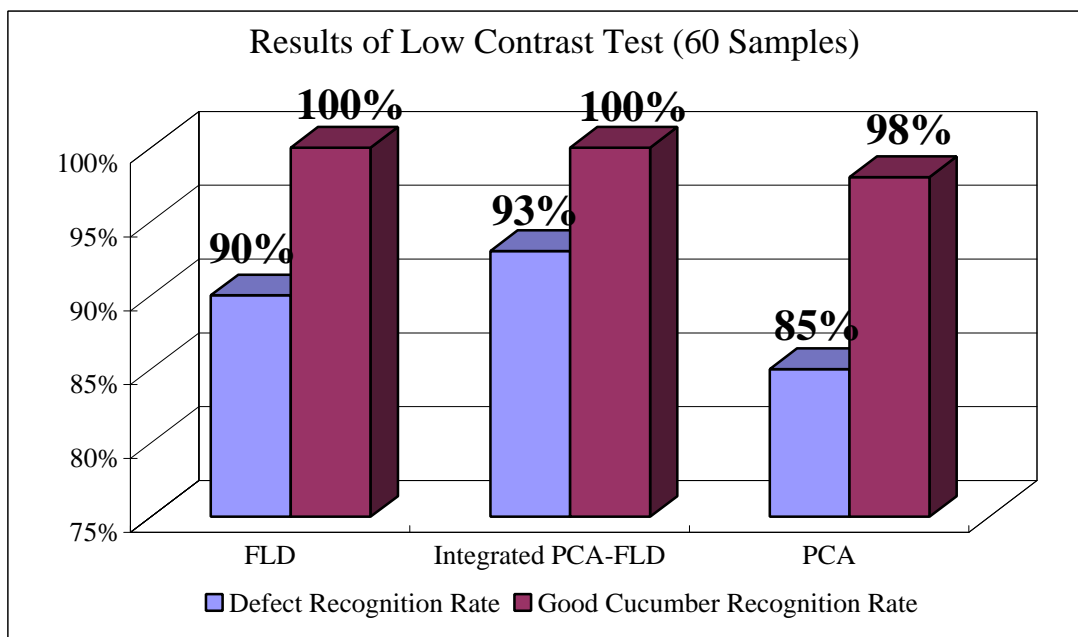


Figure 4.6 Chilling injury detection rates and good cucumber recognition rates were shown by using FLD, PCA and integrated FLD-PCA methods for the second experiment, where a total 60 cucumber image samples were used as training samples and the same 60 cucumber images were tested.

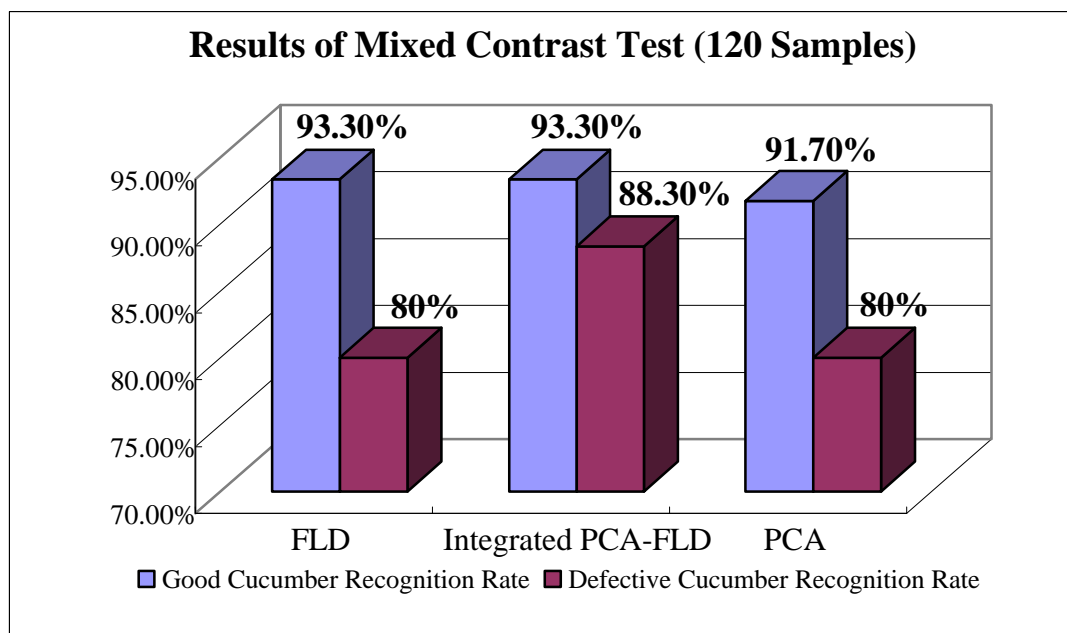


Figure 4.7 Chilling injury detection rates and good cucumber recognition rates were shown by using FLD, PCA and integrated FLD-PCA methods for the third experiment, where 40 image samples were used as training samples and another 80 image samples were used as testing samples. The rates were calculated based on the 80 testing image samples only.

More challenging samples were trained and tested in the second and third experiments as listed in table 4.3. The recognition results are shown in figure 4.6 and figure 4.7, respectively. In the second experiment, 60 samples were used for training and the same samples were used for testing, therefore the recognition rates for both good and injured cucumbers were high. In this case, the K value was chosen at 0.20. Since these two classes had very similar spectral characteristics, the differentiating information played a more important role in classification. Therefore, FLD solution showed better performance than PCA. By using the FLD method, the defect recognition rate achieved 90%, and the good sample recognition rate was 100%, which were, respectively, 5% and 2% higher than those of using PCA method.

In the last experiment, 40 samples were used for training, and an additional 80 samples were tested. The samples were diversified and covered all types of injured cucumbers mentioned before. In this case, the K value was selected at 0.20. The combined PCA-FLD solution got 93.3% injured cucumber recognition rate and 88.3% good cucumber recognition rate. In all these experiments, the integrated PCA-FLD solution got the best recognition results compared with those of the other methods.

Table 4.4 Summary of Three Feature Extraction Methods

<i>Method</i>	<i>Property</i>	<i>Comments</i>
<i>PCA</i>	<i>Linear Transform, eigenvector-based</i>	<i>Good representative, good for high-contrast data classification</i>
<i>FLD</i>	<i>Linear Transform, eigenvector-based</i>	<i>Good for discrimination on low contrast data classification</i>
<i>Integrated PCA-FLD</i>	<i>Linear Transform, eigenvector-based</i>	<i>Good for both representation and discrimination, need to choose proper K values</i>

Table 4.4 summarizes the three methods discussed above. All these methods are considered transformation-based feature extraction methods. The original features are linearly combined to produce new projected features at a lower dimension. The new projected features compared with any subset of original features at the same dimension have a better performance in some aspects. For instance, the new projected features generated by the PCA method are good at pattern representation, and also good at differentiating the obviously separated patterns. But for similar patterns, the FLD method performs better in classification purpose. However, since the distinguishing information between two classes in FLD is more heavily weighted, FLD is more sensitive to noise and less stable than PCA. The integrated PCA-FLD method overcomes the drawbacks of the previous two methods while it preserves the advantages of both. Moreover, the new method provides more flexibility in dealing with different sample patterns by adjusting the K value properly.

4.4 Conclusions

In this study, we proposed a novel integrated PCA-FLD method for hyperspectral feature extraction and applied it to cucumber chilling injury detection. The integration process was neither a simple combination of the two methods nor using them sequentially during the entire procedure. The new method was derived based on a constructed evaluation equation that combined the representation and classification effects together. Based on our sample data, better recognition performance was achieved by using the new method.

We concluded that for hyperspectral band combination, integrated effects of both representation and classification should be taken into account. The principal

components preserved the most energy of the original data, and provided good performance in recognizing obviously separated classes. The discriminant analysis contributed to classifying similar patterned classes. By properly adjusting the weight factor K , the integrated PCA-FLD method was more flexible in processing with different sample patterns and the result became robust to noise. This method can be extended to other hyperspectral imaging applications for safety and quality inspections.

CHAPTER 5 COMPARISON OF PATTERN RECOGNITION METHODS FOR HYPERSPECTRAL IMAGING AND BAND SELECTION

5.1 Introduction

Hyperspectral imaging technology has been used in many areas, including remote sensing (Landgrebe, 2002), microscopic analysis (Schultz, *et al*, 2001; Huebschman, *et al*, 2002), genetic analysis (Sinclair, *et al*, 2004), homeland security (Houser, 2002; Vogel, 2003), food safety (Kim, *et al*, 2000; Kong, *et al*, 2004) and fruit/vegetable inspection (Mehl, *et al*, 2004; Lu and Peng, 2004). More and more research interests have been put on advanced hyperspectral imaging systems and pattern recognition methods for hyperspectral data analysis.

In a typical hyperspectral imaging system, the reflection image data for each pixel is captured over various spectral bands, forming a so called *image cube* for the subject and background, i.e., for each pixel in the view, both spatial (two dimensions) and spectrum (one more dimension) information are acquired and recorded by the imager. The vast amount image data can provide more information about the object than ordinary monochrome or multi-spectral imaging methods. Due to its superior performance in terms of spectral resolution, hyperspectral imaging technology is becoming more and more popular in many inspection applications.

It is obvious, however, that the overwhelming information captured by hyperspectral imaging system can be used only if it can be processed and/or

understood, so that useful insights can be drawn from the hyperspectral image. In a complete hyperspectral inspection system, if we think of the hyperspectral imaging subsystem as the eye of a human, which captures rich information of the subject at various spectra, then the pattern recognition subsystem would represent the visual cortex of the brain, which processes the incoming information, understands the context, and makes decision. The field of pattern recognition itself is a well-established one and there has been many pattern recognition methods proposed for different applications, each could lead to a unique recognition performance. It is self-evident that in order to successfully apply hyperspectral technology in the application of produce inspection, it is important to adopt appropriate pattern recognition methods to draw sensible conclusions from the vast amount of image information yielded by the hyperspectral imaging system. In this paper, the main interest is to study the pattern recognition aspects of hyperspectral inspection techniques, specifically hyperspectral inspection of fruit and vegetables.

In general, the major tasks of a typical pattern recognition system include data preprocessing, feature extraction/selection, and pattern classification, as shown in Figure 5.1. In the training mode, the system will *pre-process* the incoming training patterns, *extract* and *select* the features which can lead to a reasonable recognition performance, and then *learn* the classification rule from these training samples. On the other hand, in the testing mode, the test patterns will go through the preprocessing step first, then certain features will be calculated, and at last the pattern will be assigned a label based on the classification rules learned during the training phase.

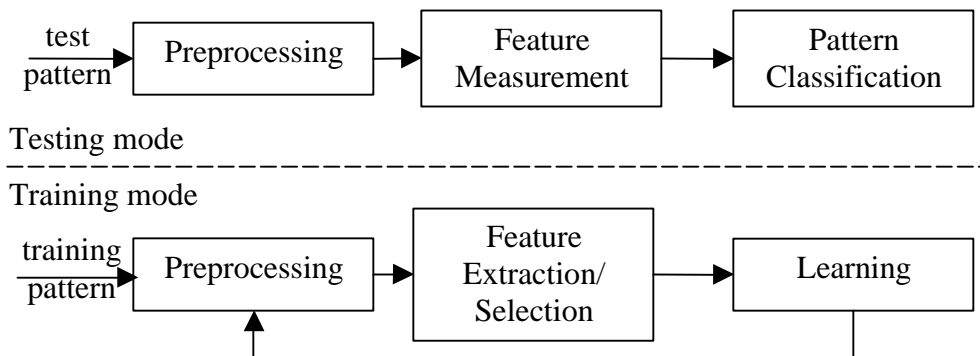


Figure 5.1 Model for statistical pattern recognition [Jain et al.,2000].

In the following part of this section, some of the most popular methods for *pre-processing, feature extraction, feature selection, and pattern classification* will be briefly reviewed.

1) *Pre-processing*. For hyperspectral imaging applications, depending on the nature of the image data, preprocessing can involve many possible processing tasks, including noise removal, image enhancement, intensity calibration, and any other operations which could lead to a better representation of image patterns. In practice, problems such as random noise and optical distortion with the original data can often pose severe adverse affects to the subsequent processing stages, thus appropriate preprocessing steps are necessary to correct or relieve these issues. For example, image noise is usually inevitable even for the most advanced imaging devices and noise in the hyperspectral images can cause difficulties or errors in the downstream processing stages. Depending on the nature of image noise, various two dimensional

filters can be used to smooth the original image and remove or suppress the embedded image noise.

2) *Feature extraction.* The purpose of feature extraction and selection operations is to construct and select the most *salient* features from the original feature space. Features, also known as attributes or measurements, are used to represent the patterns. If a pattern is represented by a set of d features, it will be processed as a d -dimensional feature vector. Generally, in image processing fields, if the object of interest can be separated from the background through segmentation, the features can be defined using the geometric characteristics of the object, such as the size, length, and width etc. In the application of hyperspectral imaging, since there are so many spectral bands involved, the dimensionality of the original feature space is often very large (usually more than 100), which requires highly efficient feature extraction and extraction methods to reduce computation complexity and minimize classification error. For this propose, researchers often use some other feature extraction methods especially the projection based methods, such as principal component analysis which can conveniently and dramatically reduce the dimensionality of feature space to less than 10 while still preserving most of the image energy.

In many hyperspectral applications, it is desirable to extract the texture features for pattern recognition. In image processing, texture refers to replications, or symmetry of certain patterns. In a set of hyperspectral images, the difference of image texture often implies a change in the physical and chemical properties on or underneath the surface. The study on texture analysis has been an active and vast research topic, and many methods were proposed over the years. Representative

texture analysis methods include the co-occurrence method, Gaussian Markov random field method and Gabor wavelet method. The co-occurrence method computes the relative frequencies of co-occurrence of grayscale pairs in the neighboring pixels. The co-occurrence method performs well in many applications, and it is believed that the demanding computational complexity is its main drawback. Another typical texture analysis method is called the Gaussian Markov random field (GMRF) method, which models neighborhood of any pixel in the textured image as a Gaussian Markov random field using random process theories, then estimates the parameters of the model and discriminates different textures based on the estimated parameters. The third method for texture analysis is based on Gabor functions, which can be related to biological vision systems. It is reported that Gabor functions were successfully applied to model the response of simple cells in the visual cortex (Daugman, 1985) and it is found by many researchers that the Gabor wavelet based texture analysis can provide very good performance compared to other texture analysis methods (Tuceryan and Jain, 1990; Tsatsanis, et al, 1992; Laine and Fan, 1993; Dunn, et al, 1994; Heeger, et al, 1995; Bashar, et al, 2003; Deng, et al, 2003; Deng, et al, 2004; Xiang, et al, 2003).

3) *Pattern classification.* As shown in figure 5.1, the final stage in a typical pattern recognition system is the pattern classifier, which assigns the incoming pattern to one of several (or more) categories, based on the d -dimensional feature vector of the pattern and one or more decision rules. There have been many types of pattern classifiers developed for different applications and some of them can be used in the application of hyperspectral inspection of agricultural produce. The choice of a

pattern classifier is crucial to the overall performance of the pattern recognition system, because it can make a significant difference in terms of final recognition results, even for the same set of samples and the same representation of feature vectors.

To date there has been numerous research efforts on pattern classifiers, and it is not possible to cover the scope of pattern recognition in its entirety in this paper; however, an overview of various pattern classifier is necessary. The large number of pattern classifiers can be categorized in different ways, including whether learning is using labeled samples (supervised versus unsupervised), and whether the decision rules are generated directly (geometric approach versus probabilistic density based approaches).

If the learning process of a pattern classifier is based on labeled samples, the process is called supervised learning, otherwise it would be unsupervised learning. Typical examples of pattern classifiers working in the supervised mode include many methods of discriminant analysis, cluster analysis is one typical unsupervised method. In many applications, if the labels of the categories are available, it is possible to train the classifier to learn about the structure of the patterns, and to generate a classification boundary. On the contrary, if the information about the labels is not available, the training process of the classifier would be unsupervised. In some cases of unsupervised learning, even the number of the classes is not known before hand, thus need to be estimated during the learning phase.

An important and unique class of pattern recognition methods is artificial neural networks, which itself has evolved to a well established discipline. Artificial

neural networks can be further categorized as feed forward networks, feedback networks, and self-organization networks. Compared with the *conventional* pattern recognition methods, artificial neural networks have several advantages. Firstly, neural networks can learn the intrinsic relationship by example. Secondly, neural networks are more fault tolerant than conventional computational methods; and finally, in some applications, artificial neural networks are preferred over statistical pattern recognition because they require less domain related knowledge of the specific application.

In this paper, the research interest is focused on the effects of various methods of preprocessing, feature extraction and pattern classification on the final recognition results in hyperspectral imaging inspection applications. In the following chapter, the various methods of pattern recognition experiments are described first, and the experimental results are presented later.

5.2 Material and Method

5.2.1 Image acquisition

Golden delicious apple samples and fresh picked cucumber samples were used in this study. Samples were stored in cold storage rooms before performing the experiments. Samples selected for testing were placed on a tray on a conveyor, and passed along a fixed path at constant speed while being line-scanned by the hyperspectral sensing system. Because the hyperspectral system was designed as a line-scan device, for each single scan, a two dimension line-spectrum data set was

generated with one dimension of line pixels and the other dimension of spectral band. Accordingly, assume a sample image was assigned with N rows, then for each apple or cucumber sample, N-number of two dimensional line-spectrum data were collected by a computer connected with the hyperspectral sensing system. Those data were the original three-dimensional hyperspectral data. In this way the hyperspectral sample data were captured for each apple and cucumber testing samples. The detailed systematic *specs* of reflectance mode of the system were introduced in the “hyperspectral sensing system” section in Chapter 4.

For a better data illustration and many other presentation and research purposes, a software tool was designed to re-arrange the original three-dimensional hyperspectral data into a conventional hyperspectral data cube. In the three-dimensional data space, each datum represented the reflectance radiation intensity of a particular spectral band at a particular pixel position. The data should be normalized by a standard references under the same illumination setup to form a reflectance factor at each pixel position. The normalization process can be expressed as,

$$R_{\text{factor}}(x, y, z) = \frac{I(x, y, z) - I_{\text{dark}}(x, y, z)}{I_{\text{ref}}(x, y, z)} \times 10000 \quad (5.1)$$

where $I(x,y,z)$ represents the reflectance radiation intensity of spectral band z at pixel position (x,y) ; $I_{\text{dark}}(x,y,z)$ represents the random noise of the sensor at band z and pixel position (x,y) when no light reflectance; $I_{\text{ref}}(x,y,z)$ represents the radiation intensity of a white Spectral panel with a known reflectance factor at band z and pixel position (x,y) under the same illumination situation. $R_{\text{factor}}(x,y,z)$ is the normalized reflectance factor that is used for each pixel (x,y) at band z . In Equation (5.1), the scaling factor 10000 was used to boost the dynamic range of the reflectance effects.

The re-arranging and normalization processes are called the calibration process of the original hyperspectral data. After the calibration, the 3-D data cube is considered a 3-D image cube.

5.2.2 Image preprocessing

After the hyperspectral images of the cucumbers and apples are recorded, the image data need to be preprocessed prior to subsequent processing steps.

5.2.2.1 Noise removal

The image noises in the hyperspectral images can lead to difficulties, even errors, in the downstream processing steps. It is noteworthy that the image normalization mentioned above cannot remove the image noise, because although the process of image normalization changes the grayscale of each pixel, it cannot change the intrinsic image patterns composed of adjacent pixels. In general, the image noises can be removed or significantly suppressed using 2D filters. In this study, the calibrated images are processed with a 3×3 median filter and a 5×5 2D Gaussian filter sequentially to remove the image noise. The median filter is defined as

$$I'(x,y)=\text{median}(N(x,y)) \quad (5.2)$$

Where (x,y) are the coordinates of a image pixel, $N(x,y)$ is its 3×3 neighborhood, and $I'(x,y)$ is the grayscale at the pixel after filtering. Median filter is known for excellent performance of removing *salt-and-pepper* image noise.

The general form of a 2D Gaussian filter kernel is

$$G(x, y) = \frac{1}{2\pi s^2} e^{-\frac{x^2+y^2}{2s^2}} \quad (5.3)$$

where σ is the standard deviation of Gaussian distribution. Choosing $\sigma=1.0$ and truncating the kernel to a 5×5 square block (since the distribution outside the block is effectively zero), for numerical implementation, the convolution kernel of the Gaussian filter is represented by the 5×5 matrix (tile):

$\frac{1}{273}$	1	4	7	4	1
	4	16	26	16	4
	7	26	41	26	7
	4	16	26	16	4
	1	4	7	4	1

Figure 5.2 5×5 Gaussian filter with $\sigma = 1.0$

5.2.2.2 Dimension Deduction

The collected hyperspectral image data are in the form of a three dimensional image cube, with two spatial dimensions (horizontal and vertical) and one spectral dimension (from band 1 to band 112 in this study). In order to make it convenient for subsequent processing steps, the spatial dimensions are reduced from two to one by cascading the rows in the hyperspectral image cube, as shown in figure 5.3. As shown in figure 5.3, if the original hyperspectral image cube (in figure 5.3 (a)) has n_{col} columns, n_{row} rows and n_s distinct spectra, the 2D representation after dimension reduction will have $n_{col} \times n_{row}$ pixels, and each pixel has n_s spectra. This 2D representation makes it convenient for later feature extraction operations.

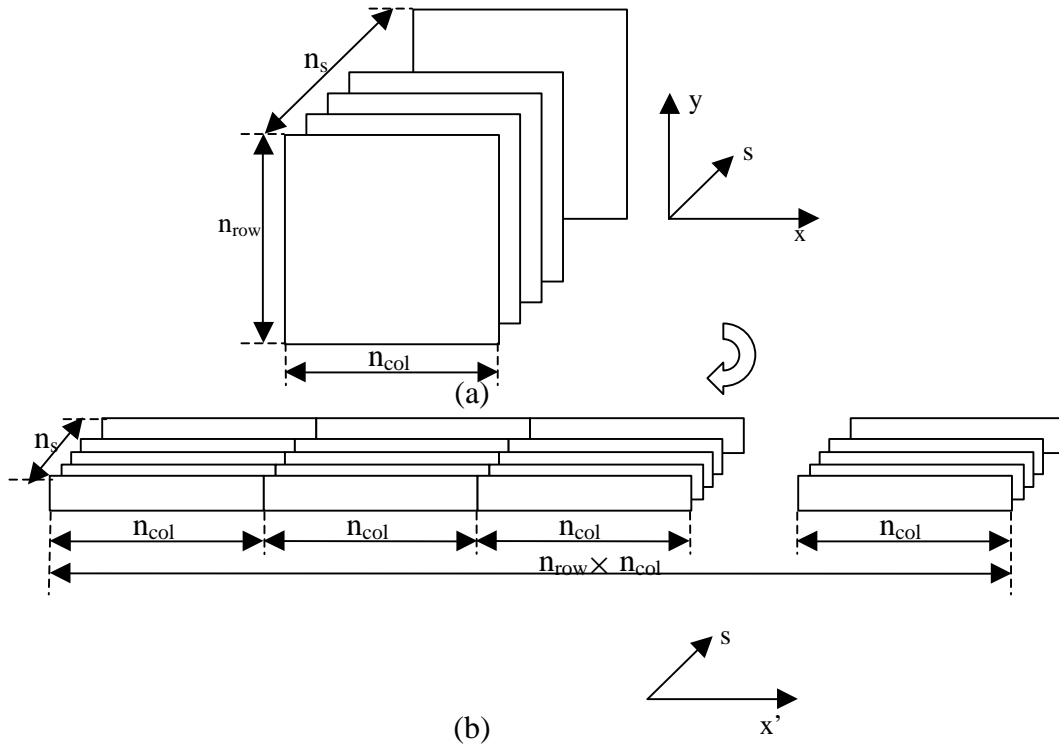


Figure 5.3 Dimension reduction of hyperspectral image cube. (a) The original hyperspectral image cube and three-dimensional coordinates system, where axis x and y are the spatial dimension and axis s is the spectral dimension. (b) The 2D image representation after dimension reduction, and the 2D coordinate system, where axis x' is the transformed spatial dimension and axis s is the spectral dimension again.

5.2.2.3 Log transform

After the image cube is reduced to 2D representation, each pixel is taken through a log transform, which is defined by:

$$L(x',s)=\log_{10}[I(x',s)+1] \quad (5.5)$$

Where $I(x',s)$ is the pixel grayscale in the 2D representation of hyperspectral image, and $L(x',s)$ is the log transformed pixel grayscale. The major motivation of

adopting log transform is that complicated algebraic operations (such as multiplication, division, power and root operations) of original grayscales at different spectral bands can now be modeled using simple algebraic operations (addition and subtraction) of the transformed grayscale.

5.2.2.4 Gabor wavelets for texture analysis

As mentioned above, texture features can be useful in certain hyperspectral image processing applications. If the area of interest, such as a patch of fruit defect, shows little grayscale difference from normal surface areas in the hyperspectral image, but manifests a subtle and unique pattern of textures, we can use texture analysis methods to distinguish it from the *normal* neighborhood. In the case of cucumber chilling damage detection (refer to Chapter 4), although the severely damaged area can be identified using intensity based method fairly easily due to significant grayscale variation, the mildly and trace damaged areas remains challenging. Fortunately, this problem can be addressed using texture analysis, because of the texture abnormality in the mildly and trace damaged areas.

In this section, the Gabor wavelet method is selected to preprocess the images in order to enhance the texture information. The procedures are introduced as follows. The two dimensional Gabor function $g(x,y)$ can be defined as (Manjunath and Ma, 1996)

$$g(x, y) = \left(\frac{1}{2\pi\sigma_x\sigma_y} \right) \exp \left[-\frac{1}{2} \left(\frac{x^2}{\sigma_x^2} + \frac{y^2}{\sigma_y^2} \right) + 2\pi j W x \right] \quad (5.6)$$

where σ_x and σ_y are the standard deviation of x and y , respectively, and W is the phase shift on the direction of x . The Fourier transform of $g(x,y)$ is

$$G(u, v) = \exp\left\{-\frac{1}{2}\left[\frac{(u - W)^2}{\sigma_u^2} + \left(\frac{v^2}{\sigma_v^2}\right)\right]\right\} \quad (5.7)$$

where $\sigma_u = -1/2\pi\sigma_x$ and $\sigma_v = -1/2\pi\sigma_y$.

Then using $g(x,y)$ as the mother wavelet function, a class of self similar functions called the *Gabor wavelets* can be obtained through dilations and rotations of $g(x,y)$ using the following generating function:

$$g_{mn}(x,y) = a^{-m} g(x', y') \quad (5.8)$$

where $a > 1$, m and n are integers, $x' = a^{-m}(x \cos \theta + y \sin \theta)$, $y' = a^{-m}(-x \sin \theta + y \cos \theta)$, $\theta = n\pi/K$, and K is the total number of orientations (Manjunath and Ma, 1996). For a given image $I(x,y)$, the Gabor wavelet transform is

$$W_{mn}(x, y) = \int I(x_1, y_1) g_{mn}^*(x - x_1, y - y_1) dx_1 dy_1 \quad (5.9)$$

where $*$ stands for complex conjugate. For the purpose of classification, for each region of interest, we use the mean μ_{mn} and standard deviation σ_{mn} of the transform coefficients to construct the feature vectors, where

$$\mu_{mn} = \iint |W_{mn}(x, y)| dx dy \text{ and}$$

$$\sigma_{mn} = \sqrt{\iint (|W_{mn}(x, y)| - \mu_{mn})^2 dx dy}.$$

As mentioned above, the total number of orientations is K , and if the total number of scales is S , then the feature vector can be defined as:

$$\bar{f} = [\mu_{00}, \sigma_{00}, \mu_{01}, \sigma_{01}, \dots, \mu_{0,K-1}, \sigma_{0,K-1}, \dots, \mu_{S-1,K-1}, \sigma_{S-1,K-1}] \quad (5.10)$$

which has $2KS$ elements in total.

5.2.3 Statistical pattern recognition

The general steps of statistical pattern recognition include feature extraction, feature selection, and classification. In this study, different methods of feature extraction/selection are adopted, and their results are fed to different classifiers.

5.2.3.1 Feature extraction and selection

In the feature extraction stage, several projection-based methods are studied, including principal components analysis (PCA), Fisher linear discriminant (FLD), and integrated PCA/FLD (Cheng et al, 2004) methods. The PCA method maximizes the energy:

$$E_{\text{pca}} = \phi_m^T S_t \phi_m, \quad m=1, \dots, N \quad (5.11)$$

where ϕ_m is the m^{th} projection vector, N is the total number of spectra, which is equal to n_s (see figure 5.3), and S_t is the total scatter matrix defined as

$$S_t = \sum_{k=1}^n (x_k - \mu)(x_k - \mu)^T \quad (5.12)$$

where n is the total number of samples, x_k is a N dimensional sample vector, and μ is the mean vector of all of the x_k sample vectors.

The FLD method maximizes the energy:

$$E_{\text{fld}} = \frac{\sum_{m=1}^M \phi_m^T S_b \phi_m}{\sum_{m=1}^M \phi_m^T S_w \phi_m} \quad (5.13)$$

where M is the a desired number of dimensions (certainly $M \leq N$), and S_b is the between scatter matrix, defined as

$$S_b = \sum_{i=1}^c |\chi_i| (\mu_i - \mu)(\mu_i - \mu)^T \quad (5.14)$$

where c is the number of classes of the samples, χ_i is the collection of samples in the i^{th} class, $|\chi_i|$ is the number of samples χ_i , and μ_i is the mean of all samples in the i^{th} class.

S_w in equation 3.2.12 is the within scatter matrix, defined as

$$S_w = \sum_{i=1}^c \sum_{x_{k,i} \in \chi_i} (x_{k,i} - \mu_i)(x_{k,i} - \mu_i)^T \quad (5.15)$$

The integrated PCA/FLD method maximizes the following energy

$$E_{\text{evl}} = \sum_{m=1}^M \frac{\phi_m^T [KS_t + (1-K)S_b] \phi_m}{\phi_m^T [KI + (1-K)S_w] \phi_m} \quad (5.16)$$

Where constant $K \in [0,1]$, and I is the $N \times N$ identity matrix. More details of the above feature extraction methods can be found in (Cheng, et al, 2004).

Another projection based feature extraction method is called Fisher's between-within method, and is often referred to as canonical discriminant analysis (Johnson, 1998). The canonical discriminant analysis uses a dimension reduction technique to find one or more linear combinations of the original features (or prediction variables) to provide maximum separations between the sample classes (Johnson, 1998). The coefficients of the linear combination(s) are the eigenvector(s) of the largest eigenvalue(s) of the matrix $(S_b + S_w)^{-1} S_b$, where S_b is the between scatter matrix and S_w is the within scatter matrix.

After applying any of the above projection methods, the features are extracted. In order to select the suitable features, two kinds of selection index are tested in this study, i.e., eigenvalue criterion and discriminatory power.

If an eigen analysis method, such as the above mentioned PCA or FLD based method, is used to extract the features, then the eigenvalue criterion can be adopted to

the select feature, i.e., the features with the largest eigenvalues are selected. This criterion is straightforward and convenient to apply if eigenvalues are available.

Another important feature extraction method is based on discriminatory power criterion, where in general, the features with the most discriminatory power will be selected. In this study, the discriminatory power of a specific feature is measured by its F value in an analysis of variance (ANOVA) or an analysis of covariance (ANCOVA) (Johnson, 1998). ANOVA is used if the feature is the only one under consideration, and ANCOVA is in order if there are other feature(s) serving as covariate in the discriminant analysis. In this study, we use a stepwise selection procedure instead of exhaustive search to find the desired features. Although an exhaustive search method could guarantee the optimal solution, its demanding computation complexity at large number of possible features makes it unfeasible for this study. For the stepwise selection method, the features are included in or excluded from the *selected feature pool* step by step based on the F values in ANOVA or ANCOVA. In the beginning, several threshold values need to be set for significance levels. At the first step, the features with the largest F value in ANOVA will be selected as long as it is statistically significant at the predetermined level. In each of the following steps, the features already in the *selected feature pool* will first be tested for statistical significance, and the insignificant ones will be omitted. Then all the features outside the *selected feature pool* will be tested for statistical significance, and those with a significance level higher than the predetermined threshold will be included in the *selected feature pool*. The selection process will stop if no more features can be omitted from or added to the *pool* (Johnson, 1998).

5.2.3.2 Classification

In this study several types of popular pattern classifier are implemented on the hyperspectral imaging samples, and the results are compared with each other. The classifiers tested in this study are a k-means classifier, a linear discriminant classifier, and a feed forward neural network. It is noteworthy that the k-means method is the typical unsupervised statistical classifier, the linear discriminant method is a typical supervised statistical classifier, and the feed forward network is a typical artificial neural network, in other words, we are comparing the classification performances of the typical unsupervised/supervised statistical classifiers and artificial neural network in this study.

5.2.3.2.1 K-means classifier

The k-means classifier is a typical unsupervised classifier. In general, the k-means method assumes that the samples belong to k disjoint classes, and the centroids of each of the classes in the feature space can be found in an iterative manner. K-means method will attempt to minimize the following target function (Jain et al., 2000)

$$J = \sum_{i=1}^k \sum_{n=1}^{n_i} |x_{i,n} - \mu_i|^2 \quad (5.17)$$

Where μ_i is the mean of the feature vectors of the samples in the i^{th} class, $x_{i,n}$ is the feature vector of the n^{th} sample in the i^{th} class, and n_i is the total number of samples in the i^{th} class. Details of the iterative searching algorithm used in the k-means method can be found in (Duda et al., 2000). In this study, the number of classes is two, thus $k=2$ here for the k-means method.

5.2.3.2.2 Linear discriminant

Linear discriminant method is another widely used method for pattern classification, and it is adopted in this study to classify different patterns. Linear discriminant method can effectively discriminate two multivariate normal populations with equal variance-covariance matrices. For the linear discriminant method in two-class case, the classification rule can be stated as (Johnson, 1998):

Given a sample feature vector \mathbf{x} ,

Choose class 1 if $\mathbf{b}'\mathbf{x}-\mathbf{k}>0$ and choose class 2 otherwise

where vector $\mathbf{b}=\Sigma^{-1}(\mu_1 - \mu_2)$, vector $\mathbf{k}=(\mu_1 - \mu_2)\Sigma^{-1}(\mu_1 + \mu_2)/2$, Σ is the variance-covariance matrix of the population, and μ_1, μ_2 are the mean vectors of class 1 and 2 respectively. During the training phase, \mathbf{b} and \mathbf{k} are learned from the training samples.

5.2.4 Artificial neural network

The statistical pattern recognition method uses statistical properties and criteria to differentiate data patterns. Another type of pattern recognition method which has been widely utilized is the artificial neural network method. Neural networks are designed to have the ability to learn complex nonlinear input-output relationships, using sequential training procedures, and adapt themselves to the input data.

The artificial neural network (ANN) used in this study is a multilayer feed forward network with one hidden layer (Hu and Hwang, 2002), and trained using the supervised back propagation approach. The designed neural network is fed with the preprocessed intensity and log data, and is trained to differentiate good apples, defective apples and stem-calyxes from the hyperspectral data cubes.

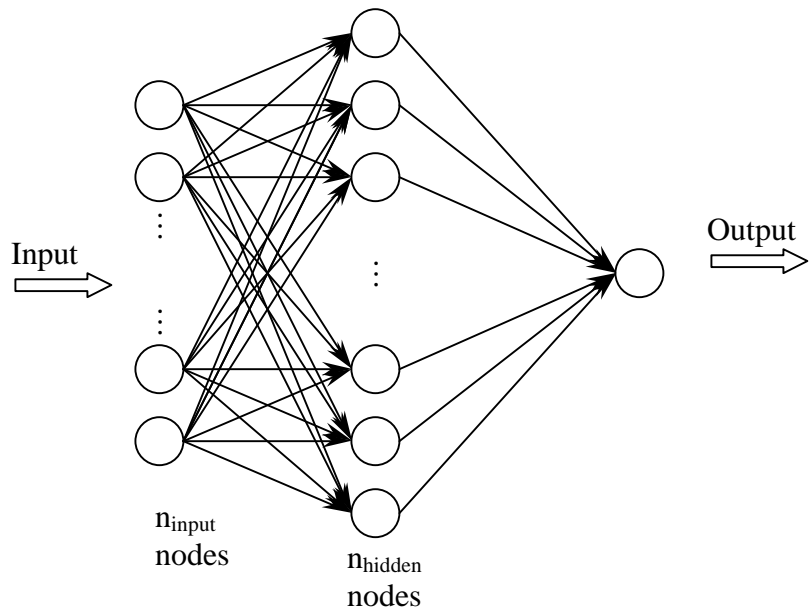


Figure 5.4 The multi-layer feed forward artificial neural network used in this study.

As shown in figure 5.4, this ANN has n_{input} nodes for input, n_{hidden} nodes in the hidden layer, and one node for output. In this study, various selections of n_{input} and n_{hidden} are tested and compared.

5.3 Results and Discussion

A total of 96 golden delicious apples were selected as testing samples in this study. Those apples were evenly divided into 16 groups. Among the six apples in each group, there was at least one good apple; one apple was positioned to show its stem-end, one to show its calyx, and the remaining of the apples were defective ones. A typical group of apple samples is shown in figure 5.5.

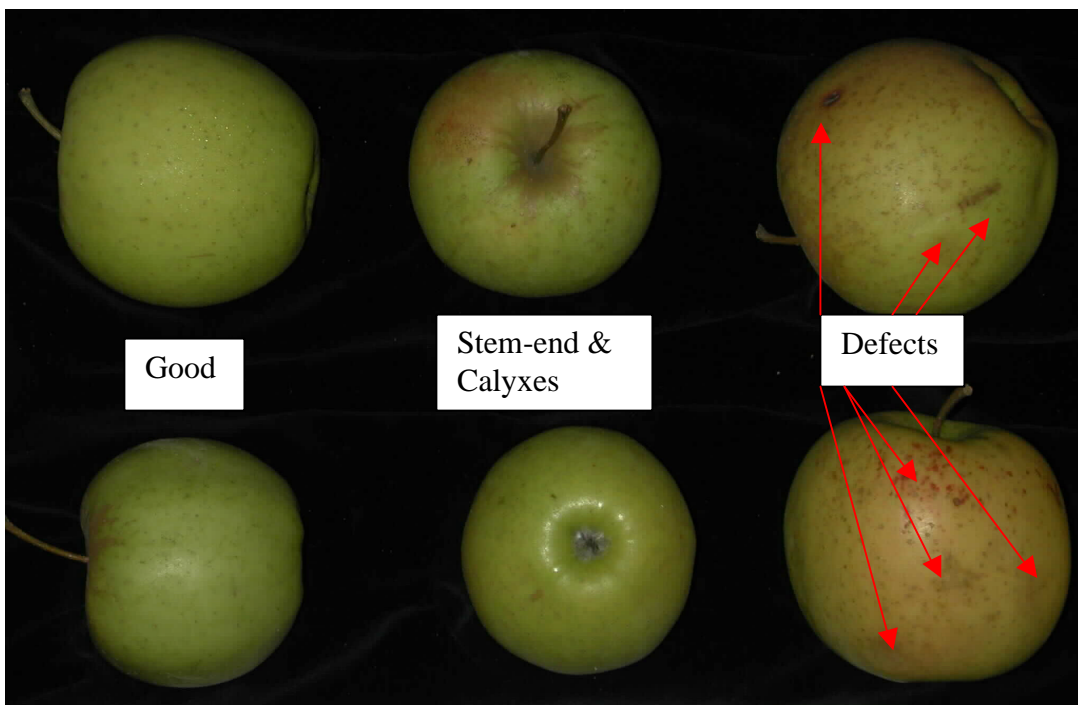


Figure 5.5 Typical apple samples used for this study.

During the experiments, patches of apple images were extracted and used as image input samples to pattern recognition algorithms. Table 5.1 summarized the properties and parameters of the apple samples used for this study.

Table 5.1 Summary of properties and parameters of input apple samples

Features	Parameters
Sample Type	Golden Delicious Apple
Total number	96
Image Patches	Total number: 199 Patch size: 60x60, 40x40, 20x20
Good Sample Patches	27
Stem-end Patches	18
Calyx Patches	22
Defective Sample Patches	132
Defects Type	Bruise, insect holes

5.3.1 Band Selection Method

5.3.1.1 Direct Comparison

From a statistical pattern recognition point of view, four band selection methods are applied. Those methods are PCA, FLD, integrated PCA-FLD, and canonical analysis method. In order to compare the performance of those methods, a direct way is to compare their detection rates.

The PCA, FLD, Integrated PCA-FLD, and canonical methods are projection-based methods. The original high dimensional dependent images data are projected to an orthogonal lower dimensional space in a way that desired properties are emphasized. For the PCA method, the designed property is the representation of the total energy of the original data. The FLD method focuses on the discriminant

property only. The integrated PCA-FLD method weights the representation and classification properties by different K values. The canonical method is similar to the FLD method that emphasizes the discriminant properties of the original data. The difference is that the FLD method directly compared the between and within sample effects, while the canonical method combines “between sample” and “within sample” effects in the comparison. From a practical point of view, it is possible that the within matrix in the FLD method becomes singular if the sample size is not big enough, however, combined with between matrix in the denominator of the canonical method, the singularity problem is largely alleviated.

Figure 5.6 shows the test results of the sensitivity of the K values versus the defect classification rate for the integrated PCA-FLD method. Two pre-processing methods were applied to the original image data cube and produce two input data sets: one is the raw image data; the other is log transformed image data. The defect classification rate changes dramatically with raw data but little with log data. The optimal K value is in the range of 0.1 to 0.5 for raw data input. While when using a simple nonlinear log transform, the optimal K value expands from 0.1 to 0.9. The log data set results in a consistently higher detection rate compared to the raw data results.

Figures 5.7 and 5.8 compare the four projection-based methods by presenting the good sample detection rate and defective sample detection rate from raw data set and log transformed data set, respectively. According to these figures, the PCA method yields lowest detection rate for both raw and log input data sets, while the FLD and the integrated PCA-FLD methods tend to present the best detection performances.

The detection rates shown above were the results of using the first principal feature vector (Cheng et al., 2004) as the projection vector for feature extraction and utilizing the K-means method as the classifier. The extracted feature is a new vector that linearly combined all the original feature bands. The first principal feature vector coefficients represent the “contribution” of individual feature band towards the final extracted feature, therefore, the most distinguished feature bands can be selected by sorting the absolute values of the coefficients of the first principal feature vector. Table 5.2 (a), (b) shows the selected three most distinguished feature bands and their linear combination coefficients by different methods from two input data sets, respectively. The selected feature bands from different methods are mostly overlapped, which means the discriminant power of the original data are mainly concentrated to those feature bands. The coefficients differ dramatically, which means the projection directions of those feature data are the major difference between different methods.

Unlike the previous projection-based methods, the stepwise discriminant analysis method tries to solve the band selection problem from a totally different point of view. It is a search-based method, a more straightforward solving strategy to this problem. The search criterion is based on the p-value of the selected bands. Similarly, if selecting only three feature bands, for different input data sets: raw or log, defect detection rate and good apple detection rate are shown in figure 5.7 and figure 5.8 respectively. The selected feature bands and their coefficients are presented in Table 5.2.

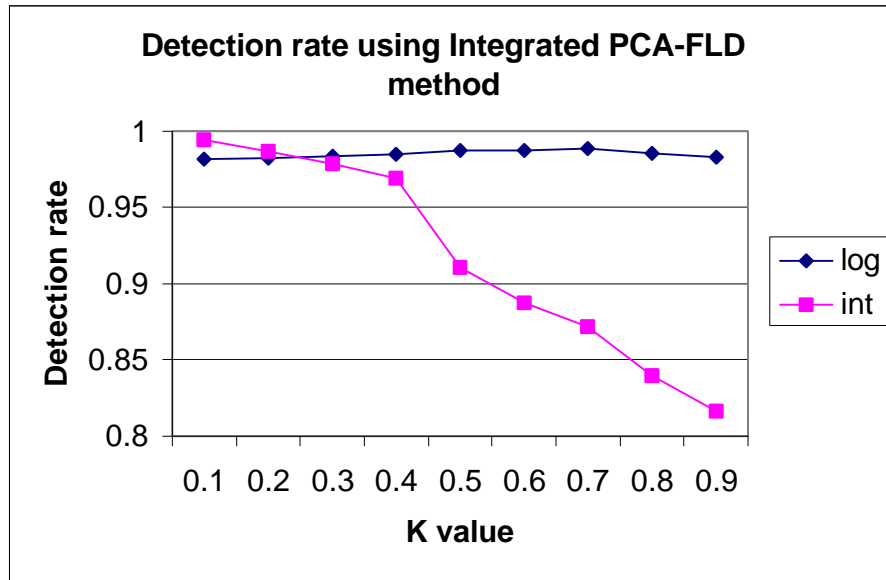


Figure 5.6 Defect detection rate of integrated PCA-FLD projection with different K values for raw data and log transformed data.

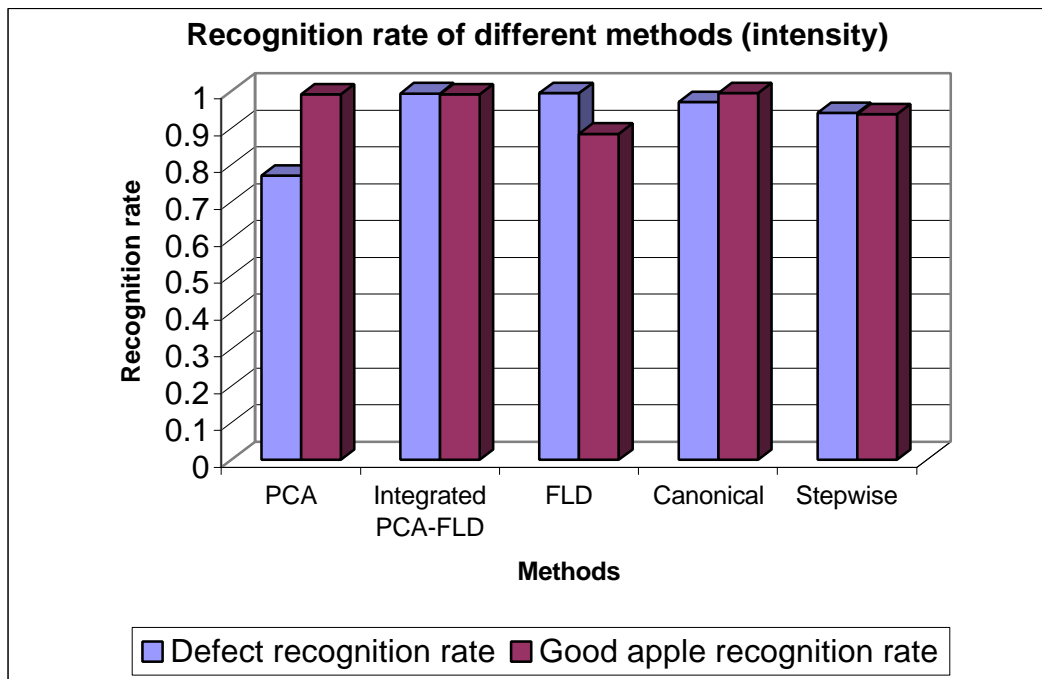


Figure 5.7 Good apple recognition rate vs. defect recognition rate of five band selection methods for raw data set.

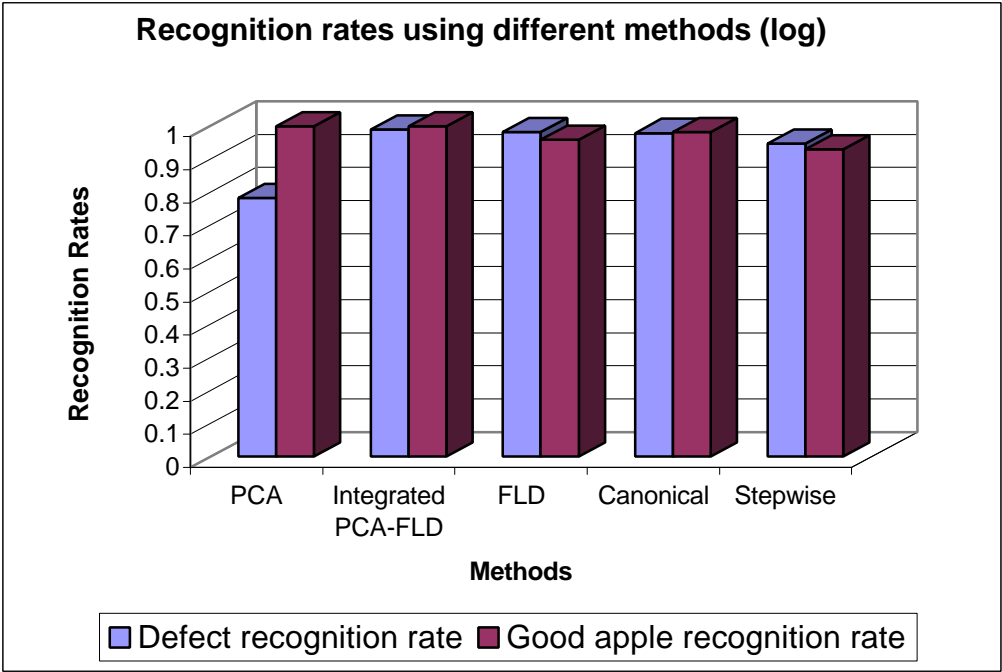


Figure 5.8 Good apple recognition rate vs. defect recognition rate of five band selection methods for log data.

Table 5.2 Best three-band combinations given by different band combination methods for (a) raw data set and, (b) log data set.

<i>Method</i>	<i>Selected Components</i>			<i>Coefficients</i>		
PCA	12	13	14	0.218744	0.22561	0.22582
Integrated PCA-FLD	12	18	23	0.11278	0.34067	0.15609
FLD	12	18	23	0.094359	0.28502	0.13059
Canonical	12	18	23	0.008171	0.015944	0.006428
Stepwise Analysis	12	21	27	-	-	-

(a)

<i>Methods</i>	<i>Selected Components</i>			<i>Coefficients</i>		
PCA	16	17	23	0.254402	0.236239	0.225929
Integrated PCA-FLD	17	18	23	0.181449	0.167734	0.179259
FLD	12	18	23	0.094359	0.28502	0.13059
Canonical	2	18	23	0.21057	0.31442	0.39212
Stepwise Analysis	1	13	21	-	-	-

(b)

5.3.1.2 Discriminant power comparison

The stepwise discriminant analysis method can be considered as an integrated process of feature selection and pattern classification. In this process, the most distinguished features vectors (or variables) are selected based on their discriminant power, and the patterns are classified using linear discriminant rules.

Despite the detection and classification results, most importantly, the stepwise discriminant analysis provides a byproduct -- the discriminant power to indicate the individual feature vector from the input feature space. If the input feature space is formed by extracted feature vectors are obtained by different projection methods, the stepwise discriminant analysis method can provide the discriminant power of each extracted feature vector. Therefore, in this study, the stepwise discriminant analysis method is used as an alternative way to compare the discriminant power of the previously mentioned four different projection methods.

Because the canonical method is very similar to FLD method, only PCA, FLD and integrated PCA-FLD methods are compared for discriminant power. Assume that for each projection method, the projected feature space contains N extracted feature vectors, and for the integrated PCA-FLD method, K value ranging from 0.1 to 0.9 are considered. Therefore, with the three methods, a total of eleven N feature spaces are examined as the input to the stepwise discriminant analysis, where $N = 112$. If one applies the PCA, FLD or integrated PCA-FLD method (with different K values each time, $K=0.1$ to 0.9) individually, followed by stepwise discriminant analysis, the first principal feature vectors in each method are associated with the highest discriminant powers compared with other extracted features in its own feature space. The second

and third principal feature vectors are associated with the second and third highest discriminant powers, respectively. Figure 5.9 shows the discriminant power (the F value) of the first principal feature vector of each method with different input data sets: raw data and log data.

If we combine all the 11 feature spaces into one large feature space and use it as the input to a stepwise discriminant analysis, the discriminant power of each extracted feature can be compared. Figure 5.10 presents the results of the discriminant power for the first principal feature vector in each method with two different input data sets. The result shows that using the PCA method, the discriminant power of the first principal feature vector (that is first principal component) is much lower compared with other extracted features using the other two methods. While simultaneously, the first principal component still remains the highest discriminant power among other principal components in the PCA.

Figures 5.11 and 5.12 give the results of defect recognition rate and good sample recognition rate using different feature extraction methods with two different data set inputs. Both results show that the integrated PCA-FLD method and the FLD method have over 98% recognition rates on both defects and good samples, while in PCA method, except for the defect detection rate with log transformed input that is slightly above 90%, all other conditions produce detection rates below 90%.

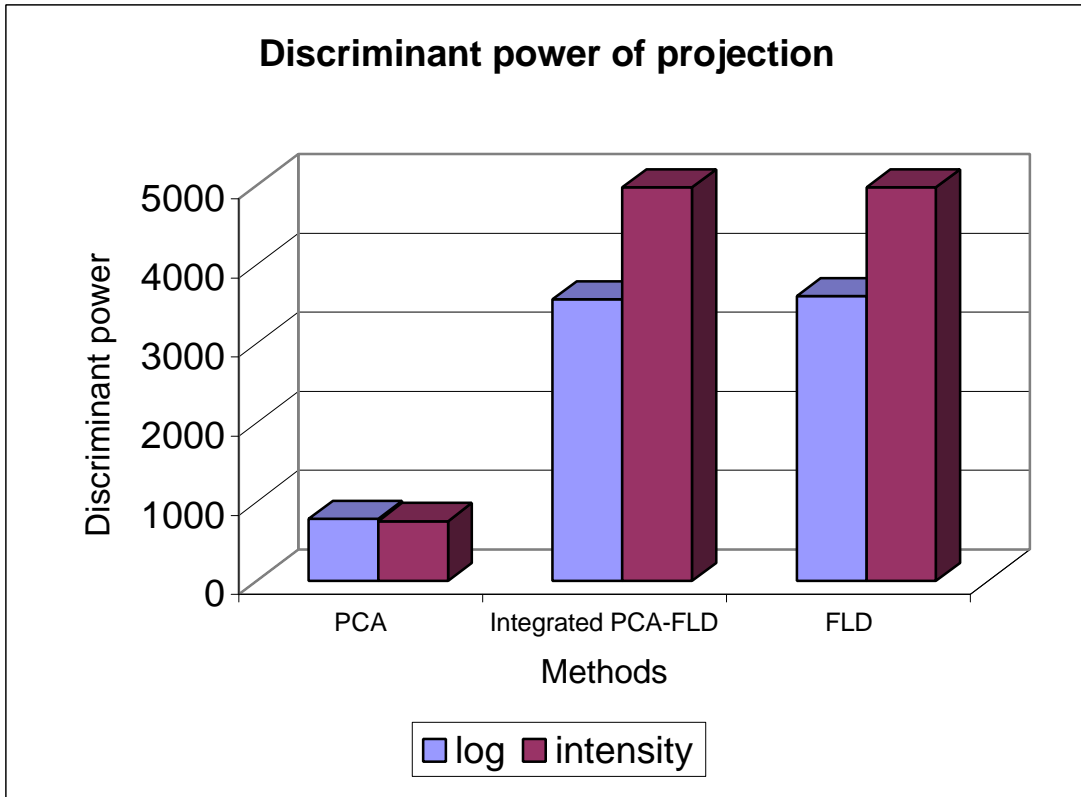


Figure 5.9 Discriminant power of three different projection methods: PCA, integrated PCA-FLD and FLD, when applied individually with raw data and log data.

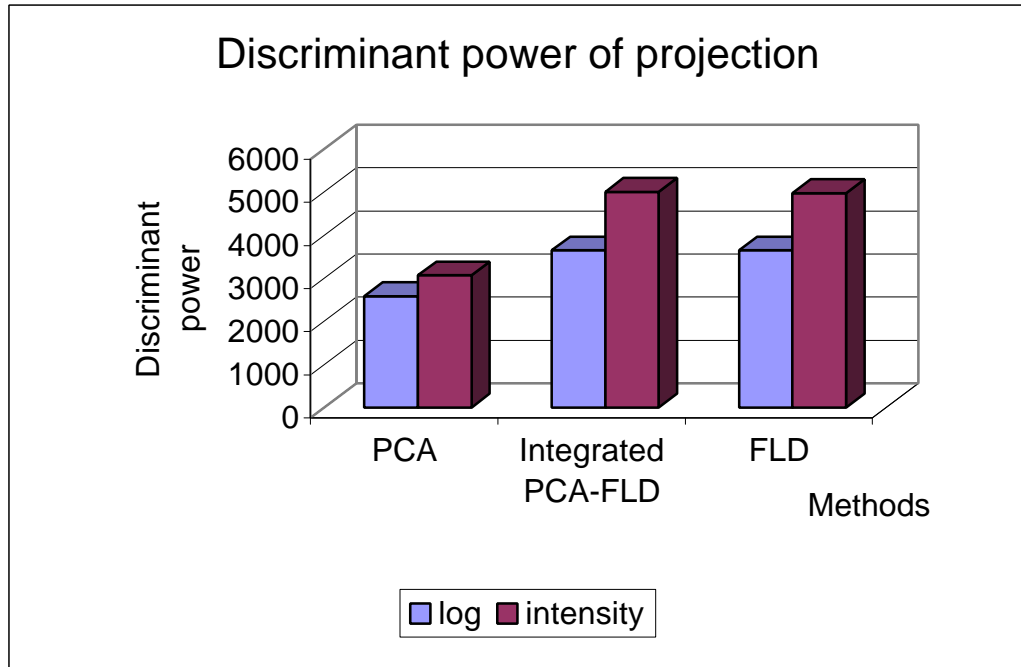


Figure 5.10 Discriminant power of different projection methods: PCA, integrated PCA-FLD and FLD, when compared under one large feature space with different input data: raw data and log data.

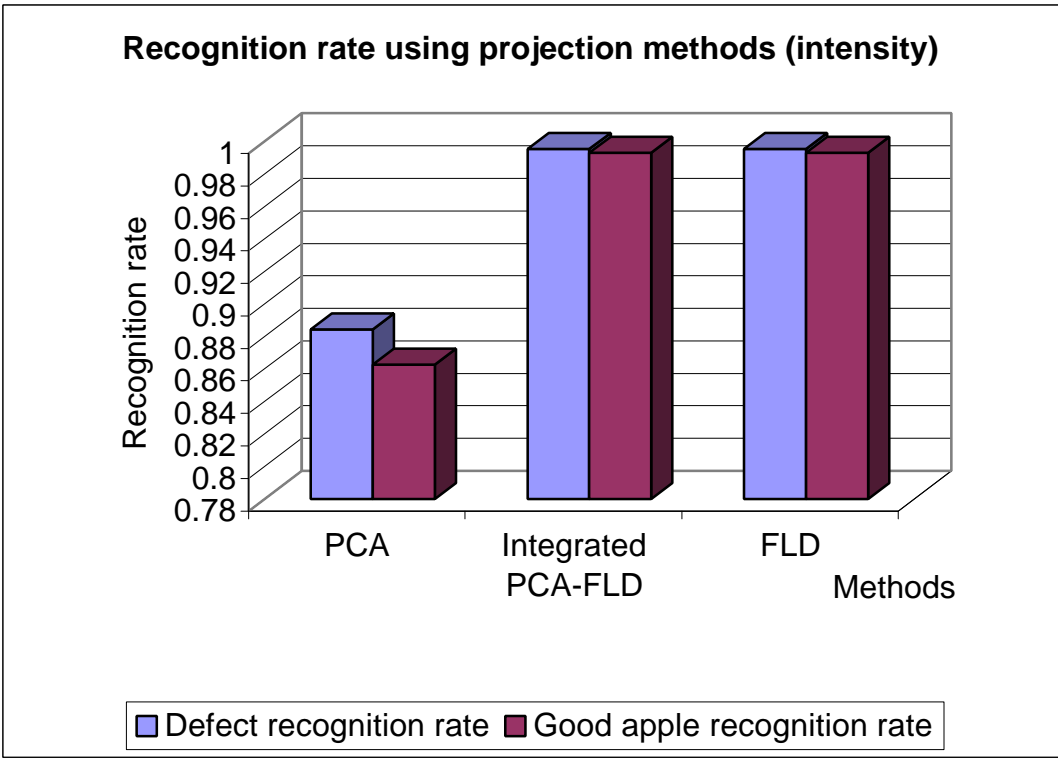


Figure 5.11 Good apple recognition rate and defect recognition rate using different projection-based methods followed by stepwise discriminant analysis with raw data input.

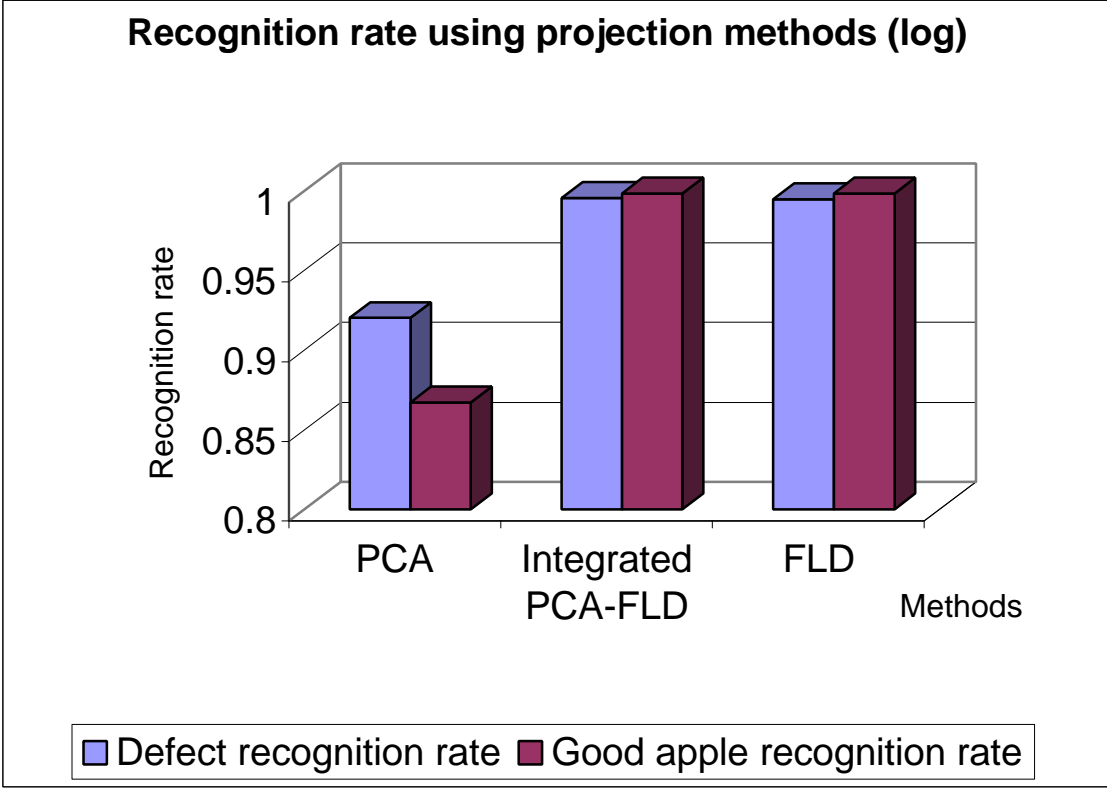


Figure 5.12 Good apple recognition rate and defect recognition rate using different projection-based methods followed by stepwise discriminant analysis with log data input.

5.3.2 Neural Network Classifier

In order to test the feed-forward neural network classifier, three scenarios are analyzed. In the first scenario, a neural network is used to differentiate good apples from defects. In the second situation, a neural network is used to differentiate apple defects from calyxes/stems. In the third scenario, three-class samples are trained and classified by a neural network. The three classes are good apples, apple defects, and calyxes/stems.

In this study, all the input samples for the neural networks are hyperspectral image pixel values. Due to the continuity of the hyperspectral sensing, without losing the generality, 28 spectra out of the 112 available spectra were selected. The spectra were “downsampled” at 1:4 ratio, that is, spectra 1, 5, 9, ..., 109 were selected to form the pixel value vector. Thus the training and testing samples for the neural network are sets of 28-element vectors (the network has 28 input nodes). In order to further explore the impacts of input data characteristics on neural network behavior, two types of inputs are tested separately for the neural network, i.e., the original pixel grayscale values and the log transformed grayscales values. The training and testing of the neural network in the three scenarios are summarized in the following.

In the case of good apples vs. defects, the training curve of the feed forward network with one hidden layer of 500 hidden neurons is shown in figure 5.13, where the training performance is defined as the mean squared error (MSE) between the actual neural network output O_{actual} and the desired network output O_{desired} , and the training curves under raw intensity input and log transformed input are shown in the same graph. As shown in figure 5.13, both networks converges after 300 epochs of

training, while the network with log transformed input *learns* faster than the one with intensity input, because as shown in the graph, the slope of *log* curve reduces significantly at around the 110th epoch while the change happens to the *intensity* one as late as the 150th epoch.

For the feed forward neural network, the number of neurons in the hidden layer (referred as hidden neurons in this study) is an important parameter determining the learning and generalization ability of the neural network (Freeman and Skapura, 1991). In order to explore the relationship between the classification performance and the number of the hidden neurons, detection rates of neural networks with number of hidden neurons from 1 to 500 are collected using the testing samples. As shown in figure 5.14, in the problem of classification between good apples and defects, for both the *log* input and the *intensity* input networks, the detection rate rises rapidly to a level of about 97% when the number of hidden neurons passes 8. It is interesting to note that when the number of hidden neurons gets larger and larger, the detection rate doesn't improve much, and after certain point, specifically, after 180 neurons for the *intensity* input network and 300 neurons for the *log* input network, the detection rate actually starts to decline. This phenomenon can be explained as over training of the neural network, which often happens when there are too many neurons in the hidden layer (Russell and Norvig, 2002).

For the classification of apple defects vs. calyxes/stems, the training curve is shown in figure 5.15, and the detection rate of different number of hidden neurons is shown in figure 5.16. Similar to the good apple vs. defects problem, the network with *log* input learns faster than the one with *intensity* input. According to figure 5.16, the

detection rate of both input types show a loose correlation with the number of hidden neurons, where the detection rate reaches the peak when the number of hidden neurons is around 80.

In the three-class classification case, again the network with *log* input learns faster than the one with *intensity* input (as shown in figure 5.17). In this case, as shown in figure 5.18 the detection rates for both input types rise to a platform of about 80% when the number of hidden neurons exceeds certain threshold (11 for *intensity* input and 30 for *log* input), and then start to decline after the mark of 200 neurons.

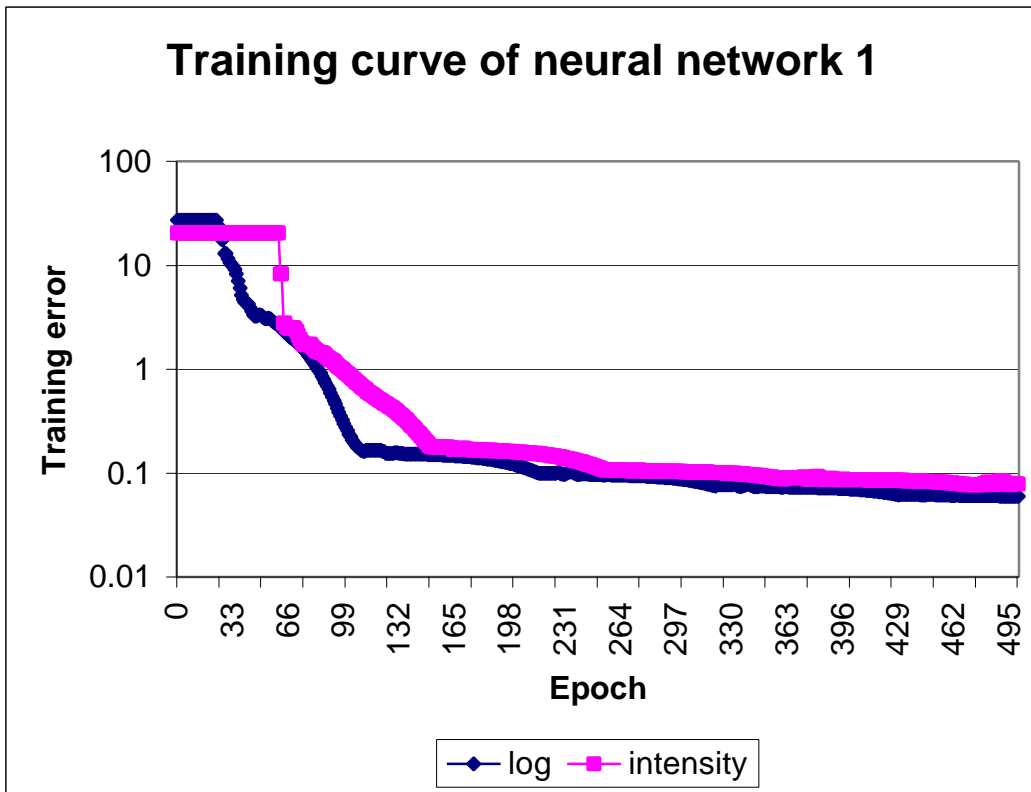


Figure 5.13 Training curve of neural network 1

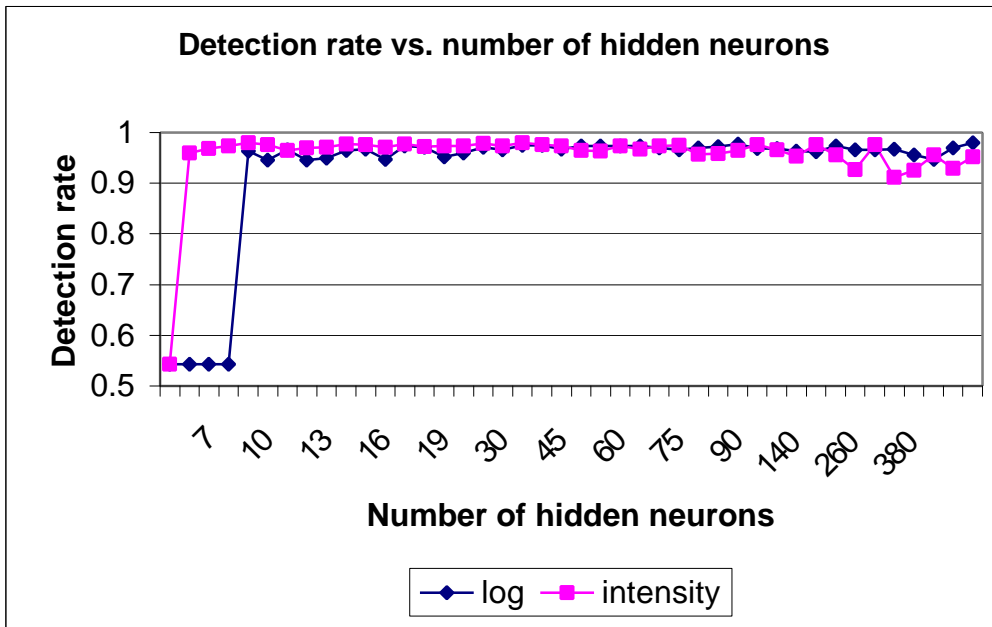


Figure 5.14 Relation between detection rate and number of hidden neurons in neural network 1. This network is trained to differentiate good and defective apples.

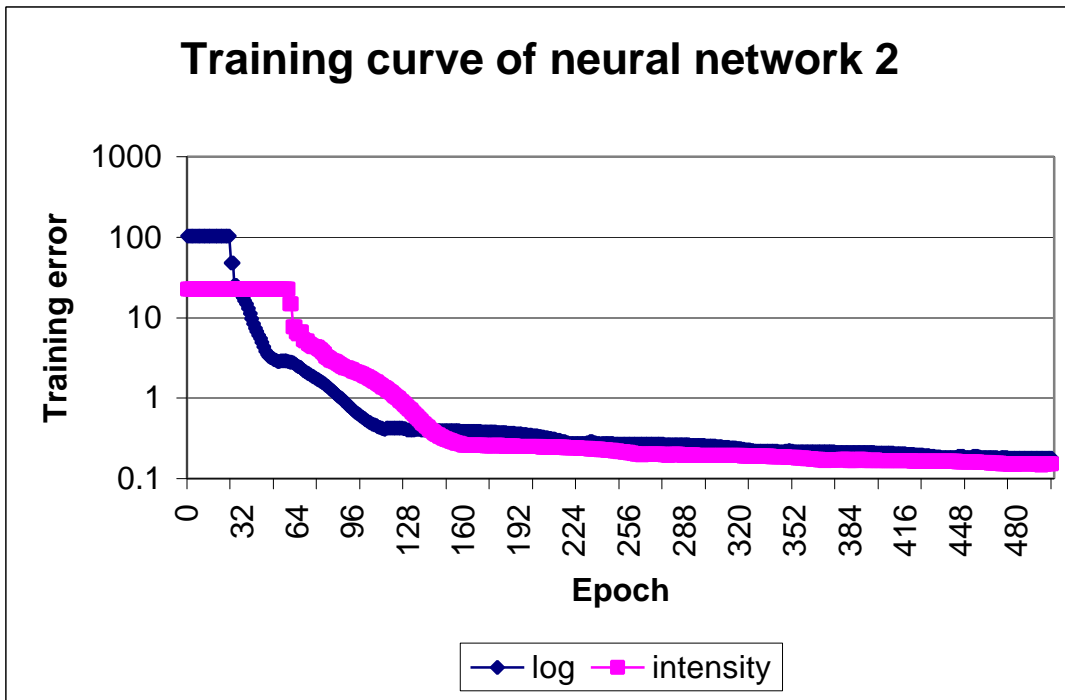


Figure 5.15 Training curve of neural network 2, which is used to differentiate defect on apples from stem/calyx.

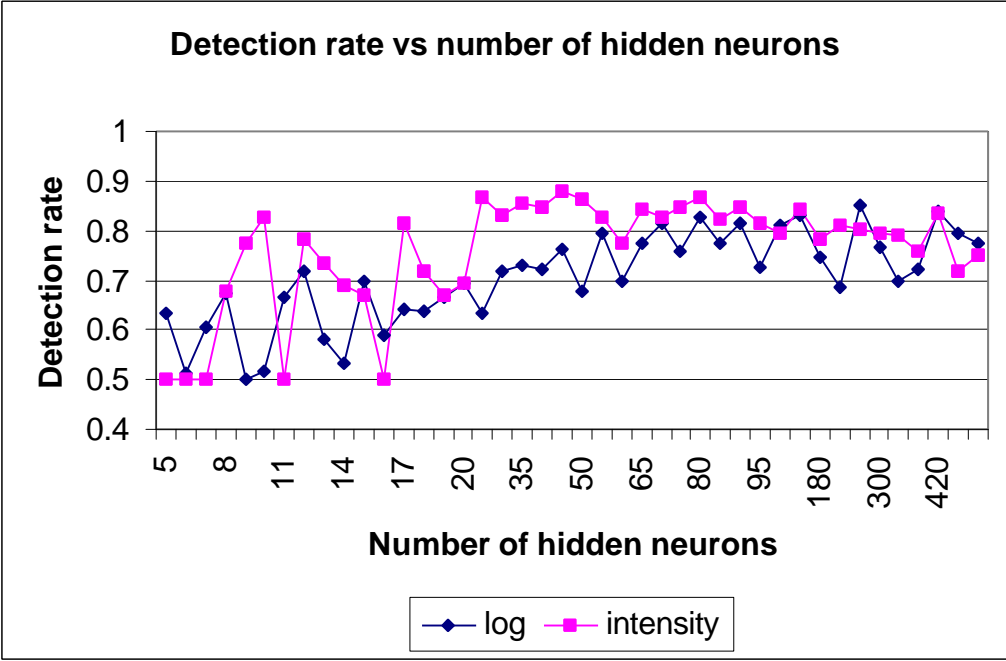


Figure 5.16 Relation between detection rate and number of hidden neurons in neural network 2. This network is trained to differentiate defects on apples from stem/calyx.

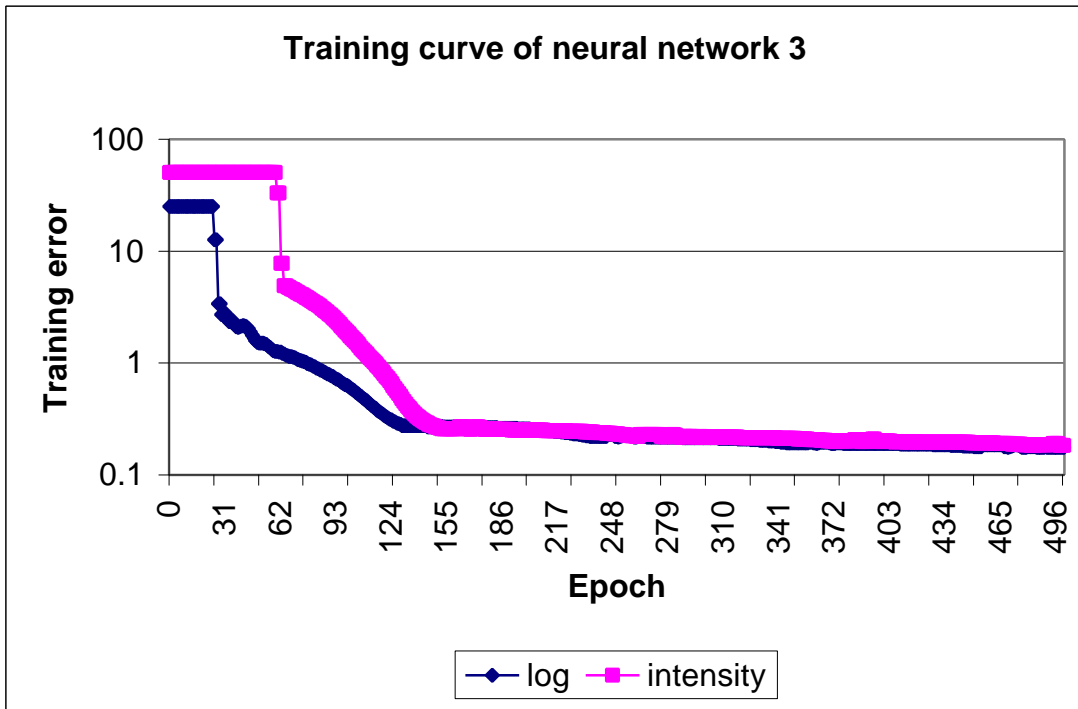


Figure 5.17 Training curve of neural network 3, which is used to differentiate the following three classes of objects, i.e., good apples, defects, and stem/calyx.

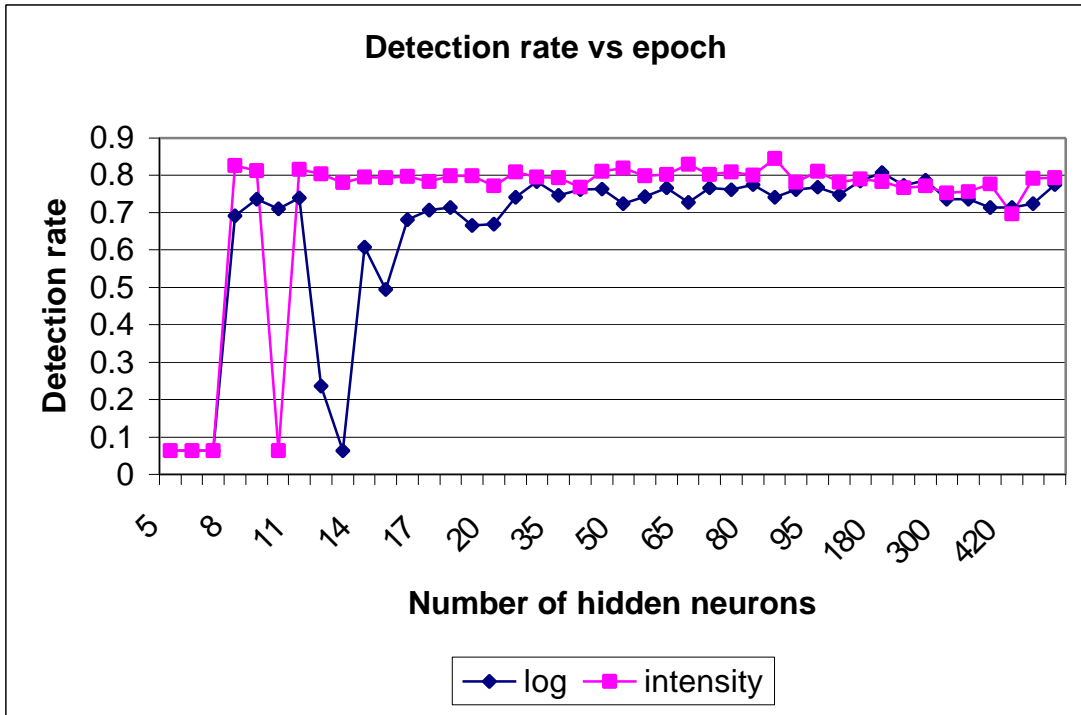


Figure 5.18 Relation between detection rate and number of hidden neurons in neural network 3. This network is trained to differentiate three classes of objects, i.e., good apples, defects, and stem/calyx.

5.3.3 Texture based feature extraction of cucumber images

In some hyperspectral imaging applications the pixel grayscale information is not sufficient to capture the difference between the areas of interest (such as the defects) and the background (such as the normal fruit surface). For example, grayscale features can be used effectively to detect apple defects and severe/moderate chilling damage on cucumbers (Cheng, et al., 2004), but for trace and slight chilling damages of cucumbers, the grayscale features are no longer suitable, as shown in figure 5.19. In the latter cases, the damages show little grayscale difference from the normal cucumber skin, thus the feature vectors based on grayscale information will provide little help in the subsequent processes. On the other hand, it is observed that the trace and slightly damaged areas show a unique texture pattern, which make it possible to use texture based feature vectors to detect these challenging defects.

Gabor wavelet features are used in this study to capture the texture information. As mentioned previously, for a 40x40 hyperspectral image patch, Gabor wavelet transform are calculated for 3 scales and 8 directions, and the values of mean and standard deviation of each transform are used to form a vector with 48 (=3x8x2) elements. After the projection process using the PCA, FLD or integrated PCA-FLD, the transformed feature vectors are provided to a k-means classifier to differentiate the hyperspectral image patches of slight/trace damaged areas and normal areas. The recognition rates of slight/trace chilling damage using grayscale features and Gabor texture features are compared in figure 5.20. It is shown that the texture feature can improve recognition performance on the challenging detection problems, and in terms

of projection methods, the integrated PCA-FLD method and FLD method always outperforms the PCA method.

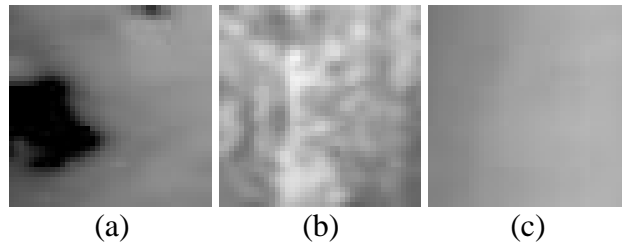
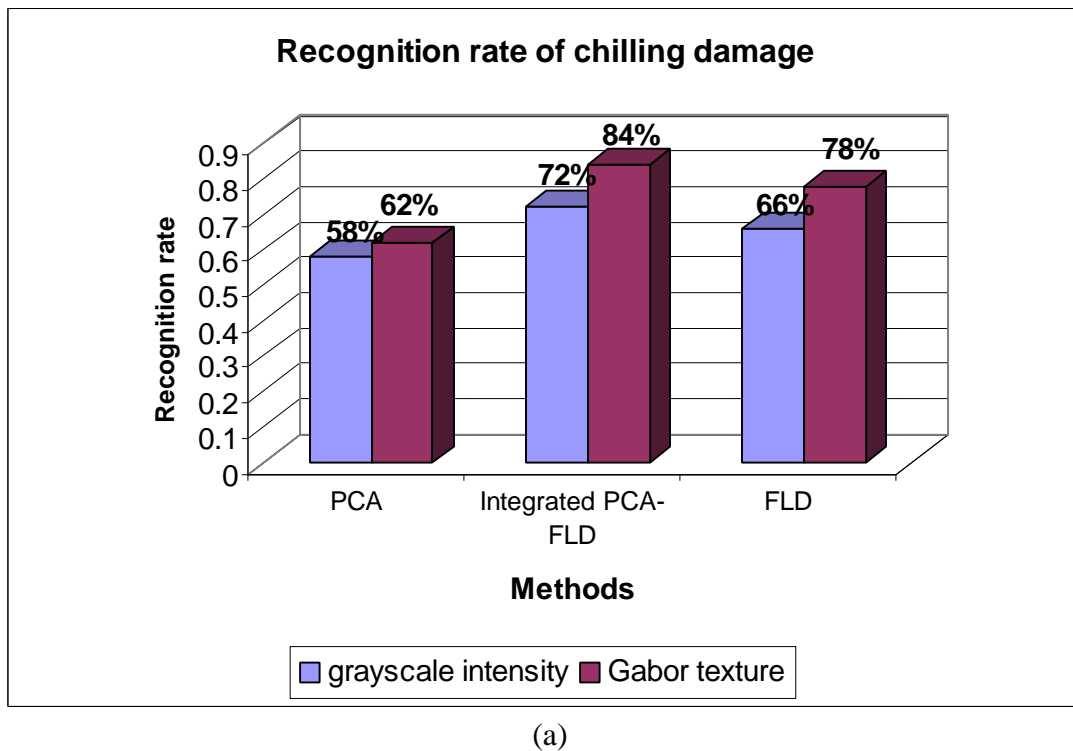
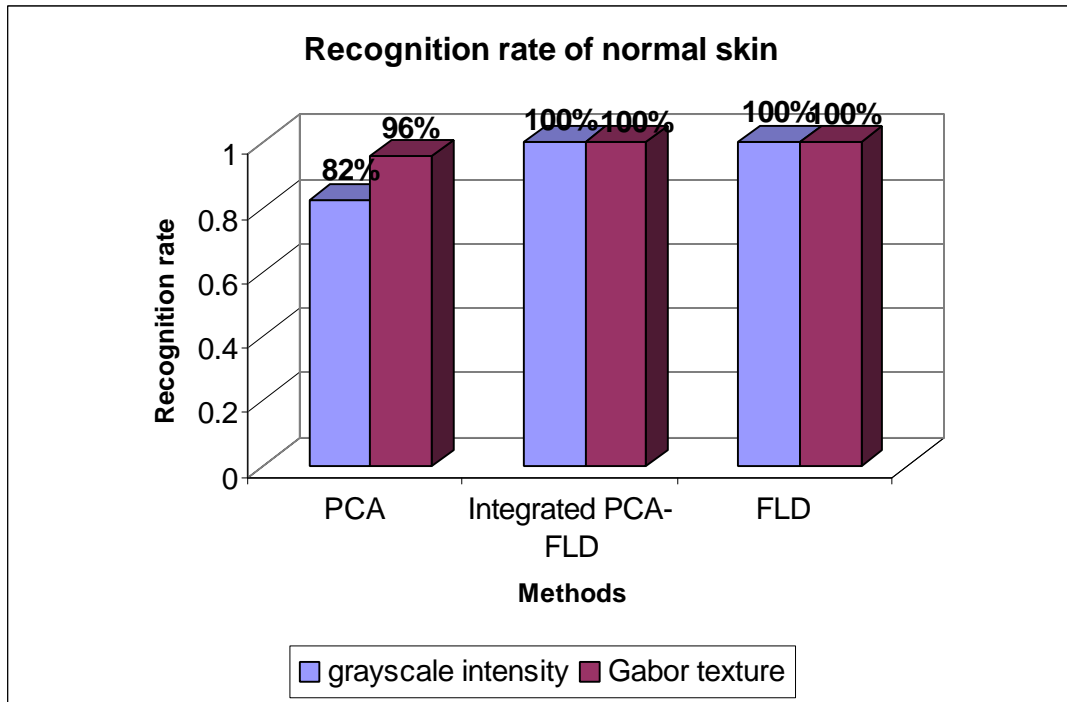


Figure 5.19. Comparison of various degrees of cucumber chilling damages, where (a) shows severe chilling damage, (b) indicates slight chilling damages, and in (c) there is no chilling damage.





(b)

Figure 5.20 Recognition rate of cucumber chilling damages vs. normal cucumber skin using Gabor texture features, where (a) shows the recognition rate of slight/trace chilling damages and (b) shows the recognition rate of normal cucumber skin.

5.4 Conclusions

In this study, at each stage of the processing, various techniques are applied and their performances are compared. In data preprocessing, logarithmic transform and wavelet transform are adopted to reveal intrinsic information of input image data. For band selection, the searching-based stepwise method and the projection-based statistical pattern selection methods are compared. K means method and artificial neural network approach are used as classifiers to identify different feature patterns.

According to the experimented results, the conclusions of this study can be summarized as follows:

1. For the different sample inputs, Log transform can improve the discriminant performance.
2. The results show that the integrated PCA-FLD method outperformed the PCA or FLD method. The reason is that both the representation information and class specific information are included in the integrated PCA/FLD feature.
3. Fisher linear discriminant analysis provides the highest discriminant power of any feature vector. The feature vectors extracted by using integrated PCA-FLD method have 99% of the highest discriminant power.
4. The first principal component of PCA presents the highest discriminant power among other principal components. Compared with FLD and integrated PCA-FLD, the first principal component has the lowest discriminant power, and occupies 22% of the highest discriminant power.
5. Neural network classification method achieves over 95% detection rate to differentiate good samples from defective ones and stems/calyxes. The detection rates are below 90% in classifying the defects and stems/calyxes.
6. Gabor wavelet preprocessing method provides better classification accuracy for slightly-damaged cucumber sample identification compared with raw data inputs.

CHAPTER 6 A NIR/MIR DUAL-SENSOR MACHINE VISION SYSTEM FOR ON-LINE APPLE STEM-END/CALYX RECOGNITION

6.1 Introduction

Apple defect inspection is an important procedure that affects the sorting or grading result in the fruit industry. Because the traditional visual apple-by-apple inspection is labor intensive and prone to human errors and variability, a machine vision system for automatic online defect inspection is needed to speed up the inspection procedure and reduce costs.

Near-infrared (NIR) spectroscopy has been widely used in fruit quality studies because it is quick and noninvasive. Previous research has shown that in the near infrared range between 700 nm and 2200 nm, the reflectance from bruised areas, stem-ends and calyxes of apples is less than that of the non-bruised areas of apples. Therefore, machine vision systems equipped with near infrared imaging sensors have been widely used in research on apple defect inspection and quality estimation. Throop et al. (1995) developed an algorithm to identify both old and new bruises for the 'Red Delicious' apples from NIR images. Bollen et al. (1999) compared methods for estimating the size of apple bruises. Paulus and Schrevens (1999) used image processing tools to quantify the average shape of randomly chosen apple. Leemans et al. (1999) exploited a color vision imaging system and a Bayesian classification method to segment apple defects. One of the persistent obstacles in the

implementation of automatic apple defect detection identified in these studies is how to identify the apple stem-end/calyx. These natural parts on apples normally present similar intensity levels as the true defects in a near infrared image. As such, a computer-based automatic vision system confuses the natural parts of the apple with true defects. This is a serious issue in apple sorting automation, because the orientations of apples along a transportation packing line are unpredictable during the inspection process. The possibility of misclassification is high and unacceptable.

To address this problem, researchers have proposed several possible solutions. Wolfe and Sandler (1985) developed an image-processing algorithm to extract both long and short stems and calyxes. Miller and Delwiche (1991) proposed an orientation algorithm to recognize the surface concavities on three-dimensional information. Yang (1993) used a structured lighting system, in which controlled illumination and cameras were used to reconstruct a stereovision image of objects. Crowe and Delwiche (1996 a, b) designed a real-time defect detection system using structured illumination to detect the stem-ends and calyxes. Most of these methods focused on detecting the natural concave shape or reconstructing the three dimensional information of stem-ends or calyxes which is computationally intensive and time-consuming. In the application of a multi-lane detection system, these methods might not be suitable due to the requirement of real-time speed and accuracy.

Compared with the single-spectrum inspection method that provides limited information for distinguishing the stem-ends and calyxes, multi-spectral detection provides richer information of multiple images from different spectral bands for the same object. Wen and Tao (1996, 1998 a, b, 2000), and Tao and Wen(1999)

discovered that by using a middle infrared (MIR) camera with a spectrum range between $3\mu\text{m}$ and $5\mu\text{m}$, bruised areas of fruit were no longer sensed and only the stem-ends and calyxes of apples remain sensitive to the sensor. A dual-wavelength sensing method was developed and found capable of discrimination of apple stem-ends and calyxes. However, in the dual-wavelength sensing system, the two image sensors are limited to be placed at the same viewing position. In general, for typical online applications, two sensors are usually mounted at adjacent but different positions. The shift between sensing positions leads to differences in pixel registration between the MIR and NIR images. Thus, there is a need for developing dual-image registration and combination/processing algorithm for an online processing purpose.

The objective of this research was to study the feasibility of applying the dual-wavelength method and develop image-processing algorithms for online apple defect inspection. In general, apples are stored in a low temperature environment (usually $3\text{-}4^{\circ}\text{C}$) before being inspected. This study is applied only to apples from cold storage. The algorithms, including dual image registration, image normalization, inverse image transformation, and dual image combination, were applied to eliminate the effect of apple stem-ends and calyxes from the true defect during inspection. These algorithms were studied to expand the dual wavelength method along with the dual image registration and synthesis strategies so that online defect identification accuracy can be improved.

6.2 Material and Method

6.2.1 Machine Vision System

The machine vision system for apple defect inspection consists of a dual-spectrum infrared sensing system and a computer controlled image-grabbing system. A lighting chamber made by Agri-Tech, Inc is used to provide uniform illumination for the infrared sensors. The 120(W) x 100(L) x 25(H) cm chamber is made of lattice-patterned sheet metal, and the V-shaped interior surface of the chamber is painted flat white to provide diffuse light reflection and eliminate shadows (Tao 1995). Lighting is provided by ten warm-white fluorescent lamps, equipped uniformly around a v-shaped surface right above the conveyor. One side of the whole chamber can be opened to allow camera mounting. Two image sensors are mounted inside on the top center of the chamber.

The near-infrared sensor utilized in the system is a Hitachi KP-MI CCD monochromatic camera attached with a Corrion's 700nm interference long-pass filter. The focal length of the camera is 16mm. The middle infrared sensor is an Indigo uncooled thermal camera with a sensitive spectrum range from 7.5 to 13.5 microns. This camera consists of a Boeing Gen II FPA incorporating a 320x240 matrix of microbolometer detectors. The pixel size of the detector is 51 μm x 51 μm and the standard focal length is 25mm. The two infrared sensors are synchronized to obtain the image at the same pace. Both near infrared images (NIR image) and middle infrared images (MIR image) are captured, processed, and analyzed by a host computer equipped with an imaging board (Matrix Meteor/RGB).

A roller conveyor belt is constructed to support and move apples for up to six lanes. The apples are rotating and moving when they are passing through the field of view of the image sensors. The online imaging system grabs the images at a rate of 30 frame/sec, which guarantees that the whole surface of each apple will be covered and processed. A drive controller and speed controller are connected with an optical encoder providing timing signals for both on-line mechanical and electrical synchronization. The system configuration is shown schematically in figure 6.1.

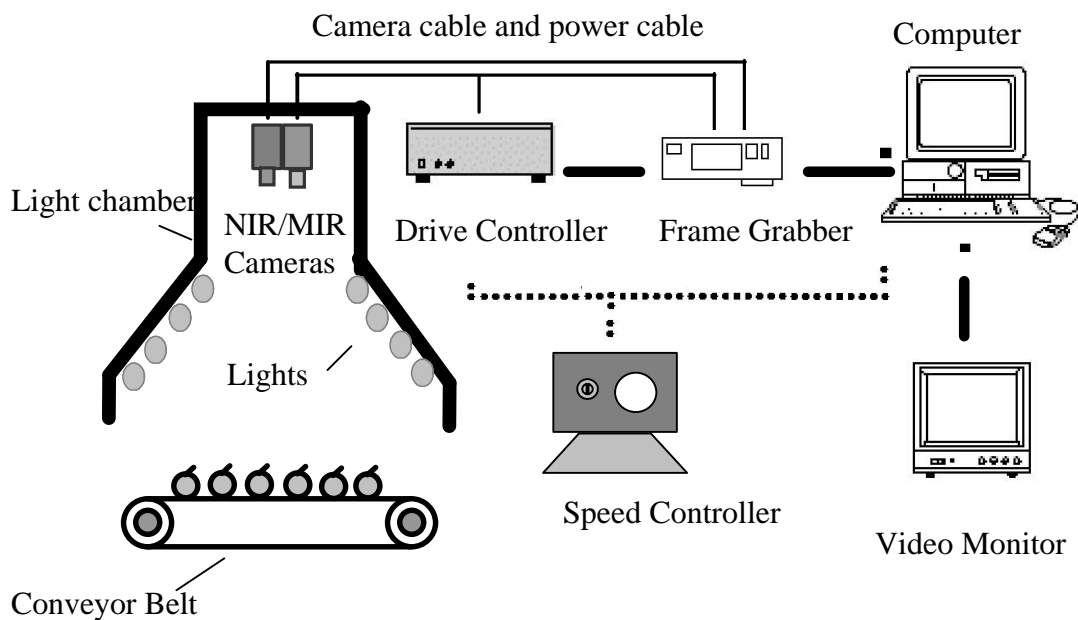


Figure 6.1 Schematic representation of the machine vision system for online apple defect inspection.

Test samples for both good and defective ‘Red delicious’ apples were used to verify the effectiveness of the on-line processing algorithms. The properties of the test samples are given in Table 6.1. A total of 155 apples (19 good apples and 136 defective apples) were selected for the test. Samples were refrigerated at about 4⁰C of

storage temperature before they were tested. Shortly after they were taken out of the cold storage (less than 5 minutes), the samples were randomly placed on the roller conveyor.

Table 6.1 Properties of the samples used for testing the performance of the online dual NIR/MIR sensing system.

Features	Parameters
Sample Type	Red Delicious Apple
Total number	155
Sample Sizes	Radius 79-81 mm Radius 68-70mm
Good Samples	19
Defected Samples	136
Defects' Type	Bruise, insect holes

6.2.2 Dual Imaging Methods

6.2.2.1 Dual-image Registration

Due to the sensor differences in the dual-wavelength sensing system, two images do not have a point-by-point correspondence. Coordination and resolution differences exist between the two sensor images. The near infrared image is at a size of 640x480, while the middle infrared one is 320x240. Proper registration is needed to enable effective information comparison/processing.

A schematic representation of the relationship between the NIR sensor, the MIR sensor and the sensed object is shown in figure 6.2.

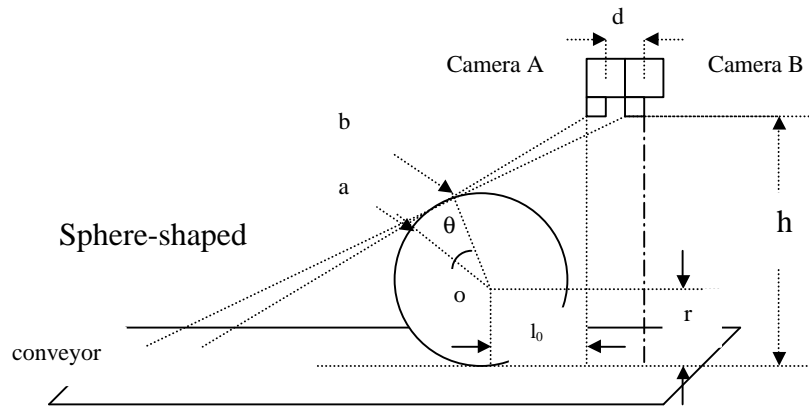


Figure 6.2 Schematic representation of the relationship among the sensing objects, the NIR sensor and the MIR sensor.

In figure 6.2, both sensors, camera *A* and camera *B*, are focused on object *C*. The horizontal distance between camera *A* and camera *B* is the camera gap and is represented by constant d . Let h represent the height from the lens to the conveyor belt and r the radius of the object. Assume the object on the conveyor belt is spherical shaped. Points ‘a’ and ‘b’ are two points on the spherical that represent the tangent limit points of the view of camera *A* and camera *B*. If l_0 represents the horizontal distance between the object’s center and the lens of camera *A*, then l_0+d is the horizontal distance from the object to camera *B*. θ is the angle between points ‘a’ and ‘b’, which represents the ‘blind’ area between sensor *A* and sensor *B*. In the ‘blind’ area, the object is only visible to one of the sensors. θ is determined by the following equation:

$$\mathbf{q} = \sin^{-1}\left(\frac{r}{\sqrt{(l_0 + d)^2 + (h - r)^2}}\right) + \sin^{-1}\left(\frac{l_0 + d}{\sqrt{(l_0 + d)^2 + (h - r)^2}}\right) - \sin^{-1}\left(\frac{r}{\sqrt{l_0^2 + (h - r)^2}}\right) - \sin^{-1}\left(\frac{l_0}{\sqrt{l_0^2 + (h - r)^2}}\right) \quad (6.1)$$

In our application, $h \gg d$, $h \gg r$, $h \gg l_0$, then $\mathbf{q} \approx 0$, which means the blind area between the dual sensors can be ignored. Both NIR and MIR sensors effectively cover the same sensing range on the object.

A two-dimensional (2-D) image-coordinate transformation is necessary to map objects in the original MIR image (OMI) to those in the original NIR image (ONI). The transformation is global since it is applied to the entire image. Suppose pixel (x,y) in the OMI is corresponding to pixel (u,v) in ONI, then

$$\begin{bmatrix} x \\ y \end{bmatrix} = F \bullet \begin{bmatrix} u \\ v \\ 1 \end{bmatrix} = \begin{bmatrix} a & b & x_0 \\ c & d & y_0 \end{bmatrix} \begin{bmatrix} u \\ v \\ 1 \end{bmatrix} \quad (6.2)$$

where, F is the 3×2 transformation matrix. Elements a, b, c, d in F are the factors related to the possible scaling and rotation of the two coordinate systems. The elements x_0 and y_0 represent the displacements in x - and y - axes respectively. F can be solved by picking at least six points in the middle infrared image plane, and obtaining at least six sets of x,y,u,v values for equation (6.2).

The different focal lengths of the two sensors in the system cause the resolution differences (NIR image resolution is 1.09mm/pixel; MIR image resolution is 1.27mm/pixel) between the original near-infrared and middle infrared images. Consequently, the same object appears to have different sizes in the middle infrared and the near-infrared images. In our system, the image size of an object in a middle

infrared image is smaller than that in a near-infrared one. A bilinear interpolation method is used to rescale the middle infrared image. In this way, the system resolution is unified at 1.09mm/pixel. Suppose that the scaling factors in the x and y directions are d_x and d_y respectively, as shown in figure 6.3.

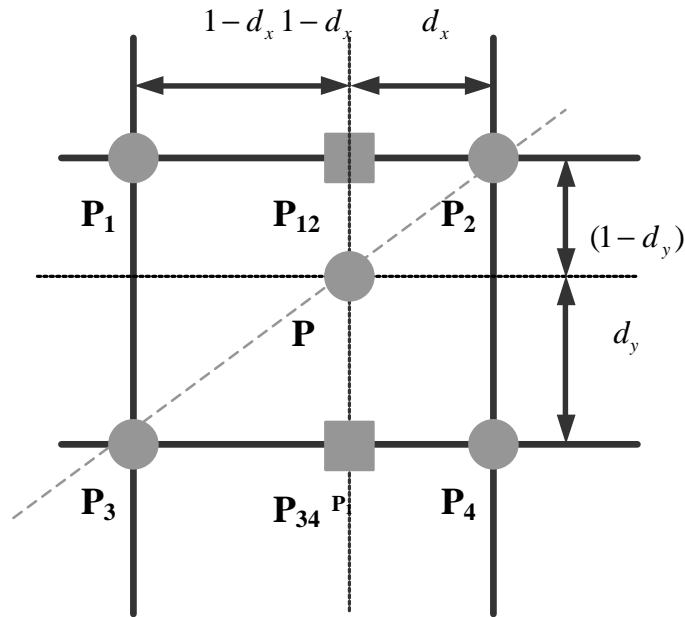


Figure 6.3 Schematic representation of binary interpolation

Bilinear interpolation takes the weighted average of a 2x2 pixel neighborhood as the assigned value to evaluate the interpolated pixel. Weights are determined by measuring the distance from the interpolated pixel to its nearest four surrounding pixels. The value of the interpolated pixel P in figure 6.3 can be evaluated as follows,

$$p_{12} = d_x p_1 + (1 - d_x) p_2$$

$$p_{34} = d_x p_3 + (1 - d_x) p_4$$

$$p = d_y p_{12} + (1 - d_y) p_{34}$$

$$= d_x d_y p_1 + (1 - d_x) d_y p_2 + d_x (1 - d_y) p_3 + (1 - d_x) (1 - d_y) p_4 \quad (6.3)$$

where, p_1, p_2, p_3 and p_4 represent the pixel values in the 2x2 pixel neighborhood of the interpolated pixel P. p is the interpolated value at P. p_{12} and p_{34} are the intermediate pixel values used to derive the value of p .

6.2.2.2 Dual-Image Processing

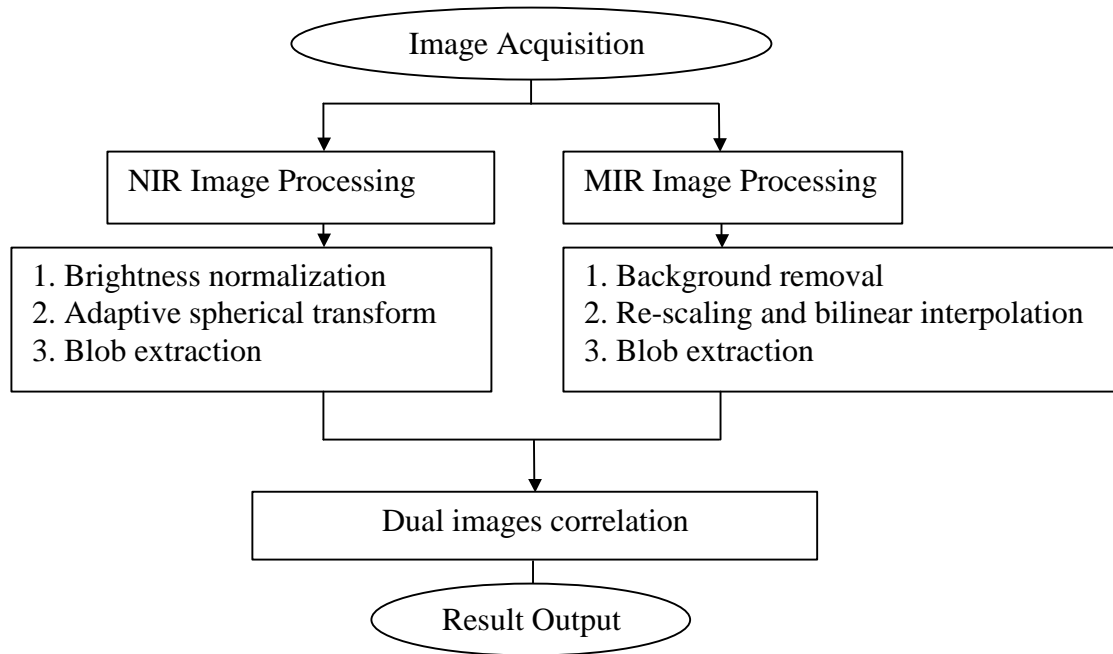


Figure 6.4 The flow chart of the on-line image processing procedure

Figure 6.4 shows the flow chart of the dual sensing image preprocessing and combination schemes developed in this study. Separate processing methods were applied to the dual sensor images, then images were combined after registration and the combination results were evaluated.

6.2.2.3 NIR Image Normalization

In the near-infrared spectrum from 700 to 1000nm, a dark-colored fruit has a lower reflectance than a bright-colored fruit. Different brightness levels cause detection errors, especially for bright-colored defective apples and dark-colored good apples. To avoid these kinds of errors, a normalization operation is applied to the original NIR image (ONI). The details of the method can be found in Wen and Tao (1998). The normalized NIR image (NNI) can be obtained from ONI by eliminating the effect of the brightness variations in ONI:

$$NNI(x, y) = c_0 \frac{ONI(x, y)}{I_{\max}(x, y)} \quad (6.4)$$

where $I_{\max}(x, y) = \max(ONI(x, y))$ for all x, y , and c_0 is a constant equal to 255 in this application (all image intensity levels are encoded using 8-bit of data); I_{\max} is generated by a recursive calculation represented by the following formulation:

$$I_{\max}(x, y)_k = \max\{I_{\max}(x - x', y - y')_{k-1} + B(x', y') \mid (x - x', y - y') \in D_I; (x, y) \in D_B\} \quad (6.5)$$

$$I_{\max}(x, y)_0 = ONI(x, y); k = 1, 2, 3, \dots \quad (6.6)$$

where B is an all-zero 3x3 mask matrix; D_I and D_B are domains of I_{\max} and B , respectively.

6.2.2.4 Adaptive Spherical Transform for NIR Image

Apples are considered to have essentially spherical shapes. The curved apple surface causes inconsistent reflection of the light. As a result, in an NIR image, the intensity distribution on the sensed apples is not uniform. Pixels around the boundary of the apple appear at a much lower intensity than the central pixels. On the other hand, the defect portion of the apples appears at a low intensity in the NIR image. The intensity levels of the two kinds of pixels may be comparable.

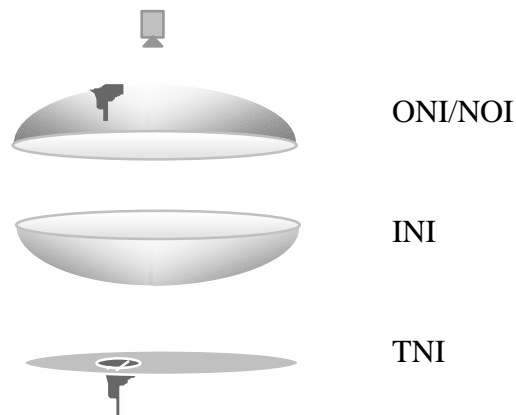


Figure 6.5 Schematic representation for the principle of spherical transformation method

An effective method called “adaptive spherical transform method” is used to distinguish them. The detailed description of this method can be found in Tao (1996) and Wen and Tao (1999). The idea of this method is to transform the edges of spherical objects to an intensity level near the intensity of the center, and thus, to generate a pseudo-plane object image with uniform intensity without losing defect information on the objects. The basic principle can be represented as shown in Figure 6.5. There are three images involved in the transformation process: a normalized near-infrared image ONI/NOI (I_{NN}), an inversed image INI (I_{NN}^{-1}) and a

synthesized image. The inversed image(INI) is a mirror image of NNI with the same shape and image size but without any defects. INI is generated by the following equation:

$$INI(x, y) = c_0 \{1 - R_N(s; (x, y)); (x, y) \in NOI(x, y), s \in S_d\} \quad (6.7)$$

where ‘s’ represents the size of the apples. S_d is a subset of size variation in pixels. $R_N[s;(x,y)]=OOI(s;x,y)/I_{max}(s;x,y)$ is the reflection correction function. The light reflectance on the curved surface differs from point to point. The inversed image INI can be considered as a group of transformation curves varied by different sizes of the objects. The transformation curves of two different sized objects are shown in figure 6.6. The TNI is obtained by combining NNI and INI together:

$$TNI(x, y) = NNI(x, y) + INI(x, y), (x, y) \in s_i \quad (6.8)$$

where s_i represents the pixels within the range of interest in NNI.

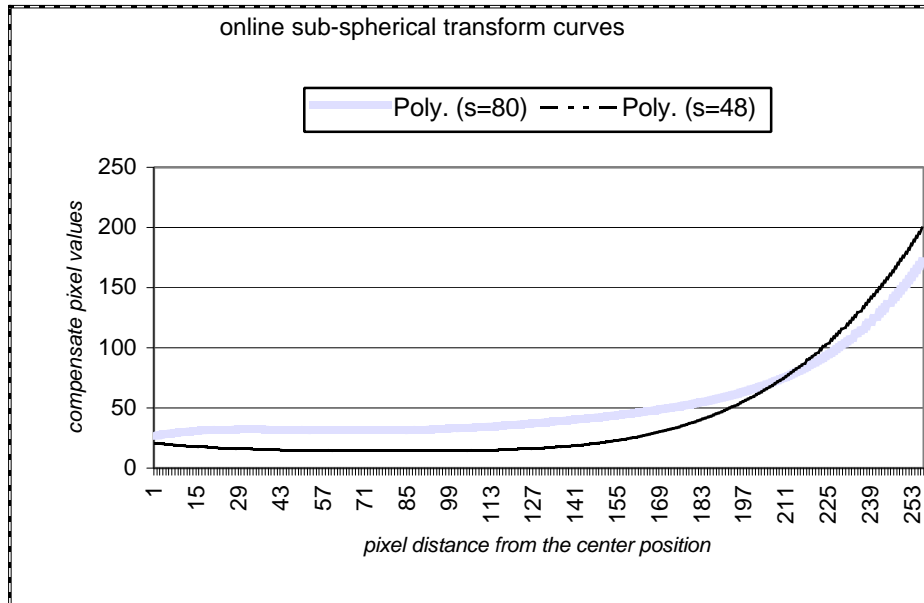


Figure 6.6 Spherical transform curves for two different sized objects.

6.2.2.5 Global Threshold on MIR Image

The mid-infrared sensor is sensitive to detecting the temperature differences on the objects within its field of view. Low temperature objects present less intensity in the mid-infrared image than high temperature objects. According to the different material characteristics and concave shape on both stem-ends and calyxes of apples the temperature in these areas of the apple is lower than in other parts of the apple surface after being refrigerated. As a result, stem-ends or calyxes appear differently from the other part of the apple by presenting a lower intensity level in the MIR image. On the contrary, defects show the same intensity levels as the non-defective parts on the apples.

To extract the stem-ends and calyxes from the original MIR apple images, the background is removed and only the object of interest is considered. A global threshold is used for the original MIR image to obtain the MI image as:

$$MI(x, y) = \begin{cases} OMI(x, y) & OMI(x, y) < T_1 \\ 0 & \text{others;} \end{cases} \quad (6.9)$$

where T_1 is the global threshold value.

6.2.2.6 Blob Analysis on NIR and MIR

Blob analysis is performed to the TNI and MI images separately to classify the pixels into different regions (or blobs). To apply blob analysis, two steps are needed: blob identification and blob labeling. Blob identification is used to categorize pixels into groups according to the similarity of certain features. Blob labeling is used to segment the identified pixels into different blobs according to their spatial positions.

Pixels with similar features are classified into the same group. Feature vectors are used to describe those features. For instance, let x_k be the feature vector for pixel k . Mathematically, x_k is represented as $x_k = [x_{k1}, x_{k2}, \dots, x_{km}]^T$. Similarly, x_j is the feature vector for pixel j , and can be expressed as $x_j = [x_{j1}, x_{j2}, \dots, x_{jm}]^T$. To judge the similarity of the two pixels, the Euclidean distance between two feature vectors, E_{jk} , is calculated as:

$$E_{jk} = \sqrt{(x_{j1} - x_{k1})^2 + (x_{j2} - x_{k2})^2 + \dots + (x_{jm} - x_{km})^2} \quad (6.10)$$

If a threshold feature vector x_0 is given, all pixels in the image can be separated into two groups.

In both TNI and MI, the feature of a pixel is simply equal to the grey level of the pixel. For TNI, the pixels are segmented into non-defective and defective (including stem-ends and calyxes) groups. In MI, pixels are also segmented into two groups: stem-ends/calyxes and blobs, where the blob represents the other portion of the apple. For a given feature vector x_0 , the segmented image is called the blob identification image (BII), which can be obtained by:

$$BII(x_k, y_k) = \begin{cases} 1 & E_{k0} < E_{th} \\ 0 & \text{others} \end{cases} \quad (6.11)$$

Here, E_{th} is a threshold value for Euclidean distance.

Blob labeling is used to identify the connected component in BII. The algorithm seeks to identify connected groups of pixels in BII that all have the same binary value 1, by scanning the entire image from top to bottom and from left to right.

Let $r(x, y)$ represents the blob-labeling image. When the $BII(x,y)=1$, the process of the algorithm used to determine the $r(x, y)$ can be described as follows:

$$r_{ini}(x, y) = 0;$$

$$r(x, y) = \begin{cases} 0 & BII(x-1, y) = BII(x, y-1) = 0; \\ r(x, y-1) & BII(x-1, y) = 1 \& BII(x, y-1) = 0; \\ r(x-1, y) & BII(x-1, y) = 0 \& BII(x, y-1) = 1; \\ r(x-1, y) = r(x, y-1) & BII(x-1, y) = 1 \& BII(x, y-1) = 1; \end{cases} \quad (6.12)$$

After performing the two steps of blob analysis to TNI and MI, blob-extracted NIR images (BNI) and blob extracted MIR images (BMI) are obtained.

6.2.2.7 Dual-image Synthesis

The BNI and BMI images are compared to remove stem-ends and calyxes from true defects in the results. The combination of BNI and BMI is used to decide which blob extracted in BNI represents the stem-end or calyx. In the final combined image (CI), the blobs that represent the stem-ends or calyxes are eliminated, and only the blobs of true defects remain. CI is generated by an iterative calculation as shown below:

$$CI_k(x, y) = \begin{cases} 0 & \text{if } BNI(x, y) = k \text{ and } BMI(x, y) \neq 0 \\ BNI(x, y) & \text{others} \end{cases} \quad (6.13)$$

$$CI_{k+1}(x, y) = \begin{cases} 0 & \text{if } CI_k(x, y) = k; \\ CI_k(x, y) & \text{others} \end{cases} \quad (6.14)$$

where, $k = 1, \dots, N$, represents the N number of blobs in BNI.

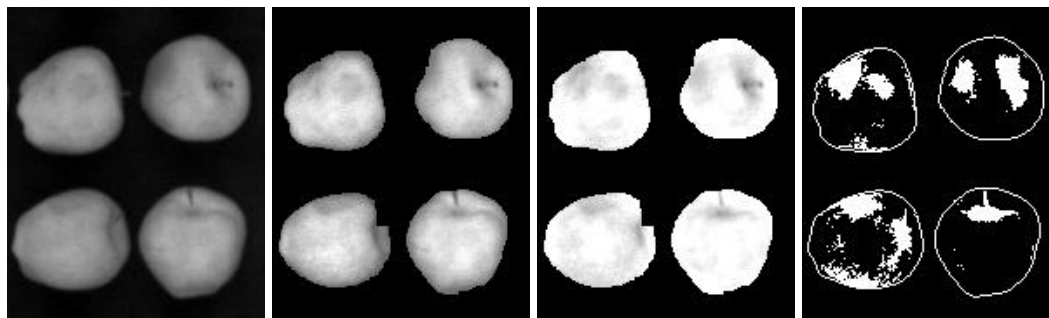
6.3 Results and Discussion

A series of the intermediate images and the final result image are presented in figure 6.7. Figure 6.7(a) represents the original NIR image output from the NIR sensor. The one located on the lower right is a non-bruised apple, which was used as the control. Each of the other three apples has at least one defect (the apple in the upper-left has two defects). Note that except for the apple on the upper left, each of the other three apples has the stem-end shown in the original near-infrared image. The brightness levels of the apples are not uniform. The maximum grey level in the original near-infrared image is typically around 190, and the minimum grey level is 25. The dynamic range of the image is 165.

The normalized NIR image is shown in Figure 6.7(c). Notice that the brightness levels of the apples were adjusted to be the same. The maximum grey level of the image became 255. Thus, the dynamic range of image was widened to be the maximum. However, the boundaries around the apples showed an obvious lower grey levels compared with the center parts.

The adaptive spherical transformation method via equations (6.7) & (6.8) is used to address this problem. As shown in Figure 6.7(e), the grey levels around the boundary area of the apples are boosted to be the same as the center areas. The non-bruised area of the apples is in the same grey level plane, while the grey levels in the defective areas remain unchanged. It becomes much easier to apply the blob feature extraction analysis to the transformed NIR image than to the raw NIR image. The extracted blobs contained true defects, stem-ends and noises that are shown in Figure

6.7(g). Noises are usually small sized blobs, ranging from one to three pixels in area. These small blobs can be eliminated by morphological operations.

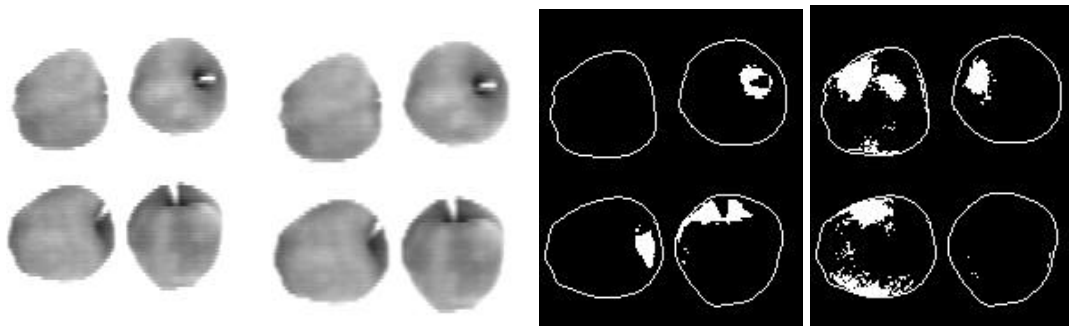


(a)

(c)

(e)

(g)



(b)

(d)

(f)

(h)

Figure 6.7 An example result of dual NIR/MIR sensing algorithm. (a) original NIR image, (b) background removed MIR image, (c) normalized NIR image, (d) resized MIR image, (e) adaptive transformed NIR image, (f) blob extracted MIR image, (g) blob extracted NIR image, (h) dual image combination result image. The boundary lines on the apples in (f), (g) and (h) were artificially added for visualization purpose.

Small sized defects with three or four pixels in area ($3/4 \text{ mm}^2$) are sometimes confused with the noises. Applying the morphological operations to eliminate the noises required the proper threshold value to measure the blob size of the noise. If the

recognition accuracy of small sized defects is important, the threshold value should be small, such as two pixels. If the good apple classification rate is crucial, the threshold value should be larger, such as four pixels. A good tradeoff value should be determined according to different applications.

For the middle infrared thermal sensor, the sensed image is different from the near-infrared one. Figure 6.7(b) shows the image of the same four apples sensed by the thermal camera. The background information removed is shown in Figure 6.7(b). It can be observed that the sizes of the objects in the image are smaller compared with those in the ONI image (Figure 6.7(a)). The registration of the two images involves the operations of coordinate transformation and linear interpolation. The result is shown in Figure 6.7(d), where the objects are of the same sizes as those in the NIR images. In the MIR images, the grey levels of stem-ends are lower compared with the other surface areas of the apples. The defective areas become ‘invisible’ to the sensor. The blob analysis on the MIR image results in the recognition of only the stem-ends of the apples, as shown in Figure 6.7(f).

Based on the given information in Figures 6.7(f) and 6.7(g), the images are combined, compared, and compensated to produce the final result image as shown in Figure 6.7(h). Only true defects are obtained in the result.

During the testing, a total of 36 stem-ends and 48 calyxes are sensed within the field of view for each camera. The final classification rates for the stem-end and calyx are shown in Figure 6.8. About 94% recognition rate of stem-end and 92% recognition rate of calyx are achieved on the test samples.

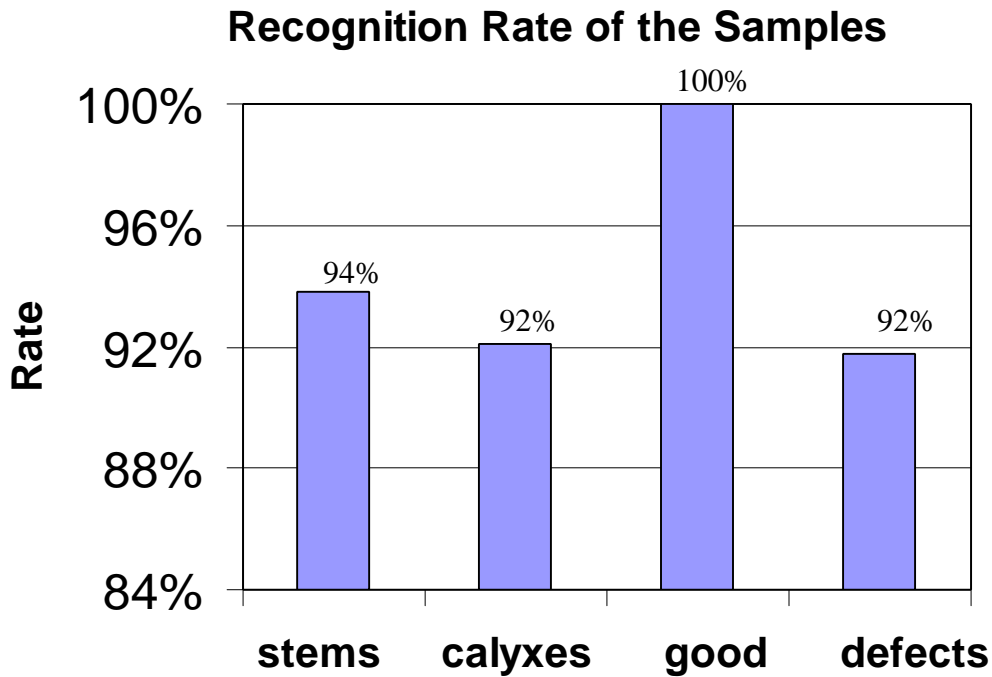


Figure 6.8 The test result of sample recognition rates for online dual NIR/MIR sensing algorithm.

All of the nineteen good apples were classified as good during the test. The classification accuracy of 100% was obtained for good apple inspection on the test. A 92% defective apple classification rate was achieved. The recognition rates on both good apples and defective apples showed the feasibility and efficiency of the dual-sensor method. The misclassification usually happened in two situations. One is when the stem-end or calyx appeared near the edge of the observed apple surface. The other is when small defects appeared very near the stem-ends or calyxes. The first situation could be improved by adjusting the threshold values in the imaging algorithms, while the second situation could be improved by refining the morphological operations.

Another factor that might affect the inspection results is the temperature distribution on the surface of the test samples. The thermal camera is sensitive to

temperature changes above 0.1⁰C. It is impossible to implement absolutely uniform temperature distribution during the processes of the online test. Some apple samples have nonuniform surface temperature distributions. As a result, in the MIR images, nonuniform changes of grey levels were observed. Fortunately, the nonuniform distributions of grey levels in the MIR image were not significant, and the proper selection of the global threshold of the MIR algorithm, by a user, would minimize their influences.

6.4 Conclusions

An on-line dual-sensor NIR/MIR imaging method was proposed and presented in this article. The sensing effects of the dual spectrum system were examined and over 92% classification accuracy was achieved for online apple defect recognition. Using the 700-750 nm wavelength sensor, both defects and stem-ends on the apple were detected. The thermal sensor with 7.5-12.5 microns spectrum was demonstrated to be effective in identification of the stem-ends and calyxes of the apples.

The statistical results on the performance of the algorithms show the feasibility of the dual-sensing methodology. The 100% recognition rate on good apples shows that the system is sensitive on type-I errors. The test result shows that the method of image registration and dual-image combination reduces the possible misclassification rate of the stem-end and calyx to 6% and 8%, respectively. The methodology and algorithms can also be considered as an extension to common inspection strategies and may also be used for other fruits or similar objects.

CHAPTER 7 CONCLUSION

The overall objective of this research has been achieved. The following conclusions are drawn from the research:

1. The testing results show that the integrated PCA-FLD method outperformed the PCA, FLD, canonical, and stepwise discriminant analysis method when they are applied separately on both cucumber chilling damage inspection and apple defect detection. Both representation and classification information are included in the integrated PCA/FLD feature, which are necessary in classifying different patterns in hyperspectral band combination applications.
2. The discriminant power analysis shows that the first principal feature vector of FLD has the highest discriminant power, while the first principal feature vector of integrated PCA-FLD has a discriminant power 1% lower than the highest discriminant power of FLD. The first principal component of PCA presents the highest discriminant power among other principal components. Compared with FLD and integrated PCA-FLD, the first principal component has the lowest discriminant power: 22% of the highest discriminant power of FLD.
3. The hyperspectral sensing research shows that the spectral band at 758nm is best for apple defects detection. Using the 700nm band in an online machine vision system, results in 100% of good apple detection rate and 92% of defects detection rate. Using NIR/MIR dual camera sensing system, the online machine vision system achieves over 92% of stem/calyx detection rate.

4. Within the range of near-infrared spectra studied (700nm-954nm), the neural network classification method achieved over 95% detection rate to differentiate good samples from defective ones and identify stems/calyxes. The detection rates are below 90% in classifying the defects and stems/calyxes.
5. Log transformed input data sets can improve the classification performance for most of the pattern recognition methods used in this study.
6. It is concluded that the integrated PCA-FLD method is highly suited to defect detection in fresh produce.
7. It is concluded that automated, real-time, produce defect detection, classification and grading is a real possibility today.

CHAPTER 8 FUTURE STUDIES

The suggestions for the future work that need to be done are:

1. In hyperspectral band selection and combination research, both projection based method and search based method have been applied separately. The research was focused on projection based statistical pattern recognition methods. Search-based methods and the optimal combination of search-based and projection based techniques need to be explored in future studies.
2. In the hyperspectral research, the log-transformed input data was found to perform better in most of pattern recognition methods in this study (compared with non-transformed input data). This suggests that nonlinearity factors affect the classification results. In future studies, nonlinear methods or nonlinear transformations should be further investigated.
3. For an online apple defect inspection machine vision system, in order to further improve the speed and detection rates of the whole system, fast algorithms and dedicated hardware techniques are needed, their development and application should be investigated in the future studies.
4. The methods presented in this study can be modified and extended to other image analysis applications, such applications should be pursued in future studies to further test their efficiency, accuracy and feasibility.

REFERENCE

- Acosta L., J.N. Rodriguez, A. Hamilton, J.A. Mendez, L. Moreno. 2003. An artificial vision system for classifying silverware, dishes and bottles. *Mechatronics and Machine Vision in Practice* 2003.
- Bae U., R. Managuli, V. Shamdasani, H. Inoue, Y. Kim. 2002. Fast unsharp masking on a programmable mediaprocessor. *Proc. of SPIE conf. medical imaging* 4687, In press, 2002.
- Bartlett, S.L., P.J. Besl, C.L. Cole, R. Jain, D. Mukherjee, K.D. Skifstad. 1988. Automatic solder joint inspection. *Trans. IEEE on Pattern Analysis and Machine Intelligence* 1(10): 31-43.
- Bashar, M. K., T. Matsumoto, N. Ohnishi. 2003. Wavelet transform-based locally orderless images for texture segmentation, *Pattern Recognition Letters* 24 (15):2633-2650
- Belhumeur, P.N., J.P. Hespanha, D.J. Krijman. 1997. Eigenfaces vs. Fisherfaces: recognition using class specific linear projection. *IEEE Trans. on Pattern Analysis and Machine Intelligence* 19(7):711-721.
- Bennett, J.O., A.H. Krishnan, W.J. Wiebold. 2003. Positional effect on protein and oil content and composition of soybeans. *Journal of agricultural and food chemistry* 5: 6882-6886.
- Biggs A.R. 1999. Apple Fruit Disease Image Directory. [Online available] WWW: http://www.caf.wvu.edu/kearneysville/disease_descriptions/disease_images/viskeyafr.html
- Bochereau, L., P. Bourguine, B. Palagos. 1992. A method for prediction by combining data analysis and neural networks: application to prediction of apple quality using near infra-red spectra. *Journal of agricultural engineering research* 51(3): 207-216.
- Bollen, A.F., H.X. Nguyen, B.T.D. Rue. 1999. Comparison of methods for estimating the bruise volume of apples. *Journal of agricultural engineering research* 74(4): 325-330.
- Bolliger, S., Y.T. Zeng, E.J. Windhab. 1999. In-line measurement of tempered cocoa butter and chocolate by means of near-infrared spectroscopy. *Journal of the American Oil Chemists' Society*. 76(6): 659-667.
- Bonizzi F., G. Finelli, F. Giva, L. Sedoni, U. Manzoli, R. Morselli, P. Pavan. 2003. Bluetooth Embedded Wireless Systems for Home Automation. *Mechatronics and Machine Vision in Practice* 2003.

- Bovik, A. C., M. Clark , W. S. Geisler. 1990. Multichannel texture analysis using localized spatial filters. *IEEE Transactions on Pattern Analysis and Machine Intelligence* 12(1):55-73.
- Brajovic V. and T. Kanade, 2004. When are the Smart Vision Sensors Smart? *Sensor Review*, 2004.
- Brajovic V. 2004. Reflectance Sensitive Retina. *SPIE International Technical Group on Electronic Imaging Newsletter*, SPIE 14(1).
- Brosnan, T. and D.W. Sun. 2002. Inspection and grading of agricultural and food products by computer vision systems -a review. *Computers and Electronics in Agriculture* 36: 193- 213.
- Brosnan, T. and D.W. Sun. 2004. Improving quality inspection of food products by computer vision —a reviewand grading of agricultural and food products by computer vision systems --a review. *Journal of food engineering* 61:3-16.
- Brown, G.K., L.J. Segerlind, R. Summit. 1974. Near-infrared reflectance of bruised apples. *Trans. ASAE* 1974:17-19.
- Brown, G.K. and L.J. Segerlind. 1975. Method for detecting bruises in fruit. *US patent 3.867.041*.
- Burns, G.H. and B.H. Gump. 1993. Technological advances in the analysis of wines. *ACS symposium series* 536:2-12.
- Campins J., J.A. Throop, D.J. Aneshansley. 1997. Apple stem and calyx identification for automatic sorting, *ASAE Annual International Meeting Paper No. 973079*.
- Castro A, and J.G.K Williams. 1997 Single-molecule detection of specific nucleic acid sequences in unamplified genomic DNA. *Anal Chem* 69:3915-3920.
- Chauhan S. , R. Mishra , J.R. Li , L. D. Seneviratne. 2003. A Feasibility Study for Mechatronic Assisted Prostate Biopsy. *Mechatronics and Machine Vision in Practice* 2003.
- Chen N.G, M. Huang, H. Xia , D. Piao, E. Cronin, Q. Zhu. 2004. Portable near-infrared diffusive light imager for breast cancer detection. *J Biomed Opt* 9(3):504-510.
- Chen, P., McCarthy, M.J., R. Kauten. 1989. NMR for internal quality evaluation of fruits and vegetables. *Transactions of the ASAE* 32(5): 1747-1753.

Chen, X. 2003. Detection of physical hazards in boneless poultry product using combined X-ray and laser range imaging technologies. Ph. D. Dissertation. University of Maryland, College Park, MD.

Chen Y. R., B. Park, R. W. Huffman, M. Nguyen. 1998. Classification of on-line poultry carcasses with backpropagation neural networks. *J. Food. Proc. Eng.* 21:33-48.

Chen, Y.R., K. Chao, M.S. Kim. 2002. Machine Vision Technology for Agricultural Applications. *Computers and Electronics in Agriculture* 36: 173- 191.

Cheng, X., Y. R. Chen, Y. Tao, C. Y. Wang, M. S. Kim, A. M. Lefcourt. 2004. A novel integrated PCA and FLD method on hyperspectral image feature extraction for cucumber chilling damage inspection. *ASAE Transactions.* 47(4):1313-1320

Chao, K., Park, B., Chen, Y.R., Hruschka, W.R., Wheaton, F.W. 2000. Design of a dual-camera system for poultry carcasses inspection. *Appl. Eng. Agric.* 16(5):581-587.

Coventry, A.G. and M.J. Hunston. 1984. Application of near-infrared spectroscopy to the analysis of beer samples. *Cereal foods world* 29(11): 715-718

Crowe, T.G. and M.J. Delwiche. 1996a. Real-time Defect Detection in Fruit. Part I: Design Concepts and Development of Prototype Hardware. *Trans. ASAE* 39(6): 2299-2308.

Crowe, T.G. and M.J. Delwiche. 1996b. Real-time Defect Detection in Fruit. Part II: An Algorithm and Performance of a Prototype System. *Trans. ASAE* 39(6): 2309-2317.

Curda, L and O. Kukackova. 2004. NIR spectroscopy: a useful tool for rapid monitoring of processed cheeses manufacture. *Journal of food engineering* 61: 557-560.

Danno K, N. Mori, K. Toda, T. Kobayashi, A. Utani. Near-infrared irradiation stimulates cutaneous wound repair: laboratory experiments on possible mechanisms. *Photodermatol Photoimmunol Photomed* 17(6): 261-265.

Das, K. and M.D. Evans. 1992. Detecting fertility of hatching eggs using machine vision. II. Neural network classifiers. *Transactions of the ASAE* 35(6): 2035-2041.

Daugman, J.G. 1985. Uncertainty relations for resolution in space, spatial frequency, and orientation optimized by two-dimensional visual cortical filters, *Journal of the Optical Society of America A* 2:1160-1169.

- Daumas B., W.L. Xu, J. Bronlund. 2003. Jaw Mechanism Modeling and Simulation. *Mechatronics and Machine Vision in Practice* 2003.
- Davenel A., CH. Guizard, T. Labarre, F. Sevila. 1988. Automatic detection of surface defects on fruit by using a vision system. *J. Agricultural Engineering Research* 41: 1-9.
- David L. Ping-Rey Jang, John C. Luthe, Michael J. McCarthy, Olin P. Norton, M. John Plodinec, Robert L. 2002. Accuracy of Glass Surface Temperature Measurements in Industrial Glass Furnaces. *Glass Manufacturing Issues*.
- Delwiche, S.R, R.O. Pierce, O.K. Chung. 1998. Protein content of wheat by near-infrared spectroscopy of whole grain: collaborative study. *Journal of AOAC International* 81(3): 587-603.
- Deng, Da, J. Zhang, M. Purvis. 2004. Visualisation and comparison of image collections based on self-organized maps, *Proceedings of the second workshop on Australasian information security*: 97-102
- Deng, H., K. L. Chan, J. Liu. 2003. The Poisson equation for image texture modelling, *Pattern Recognition Letters* 24 (9-10): 1571-1582.
- Diener, R.G., J.P. Mitchell, M.L. Rhoten. 1970. Using an X-ray image scan to sort bruised apples. *Agricultural Engineering* 51(6): 356-361.
- Downey, G. and J.D. Kelly. 2004. Detection and quantification of apple adulteration in diluted and sulfited strawberry and raspberry purees using visible and near-infrared spectroscopy. *Journal of agricultural and food chemistry* 52: 204-209.
- Duda, R. O., P. E. Hart, D. G. Stork. 2000. *Pattern Classification*. New York, NY: Wiley.
- Dunn, D., W. E. Higgins, J. Wakeley. Texture segmentation using 2-D Gabor elementary functions, *IEEE Transactions on Pattern Analysis and Machine Intelligence* 16(2):130-149.
- Dunn M., J. Billingsley, N. Finch. 2003. Machine Vision Classification of Animals. *Mechatronics and Machine Vision in Practice* 2003.
- Eisenreich N., J. Herz, W. Mayer, T. Rohe. 1996. Fast On-line Identification of plastics by Near-infrared Spectroscopy. *Proceedings of ANTEC '96, Indianapolis*: 3131-3135
- Fillion, J., F. Sauve, J. Selwyn. 2000. Multiresidue method for the determination of residues of 251 pesticides in fruits and vegetables by gas chromatography/mass

spectrometry and liquid chromatography with fluorescence detection. *Journal of AOAC International* 83(3): 698-713.

Fischer D., E. Pigorsch., K.-J. Eichhorn. 2000. Process analysis in the chemical industry by Infrared and Raman spectroscopy. Virtual Teaching Encyclopedia on Macromolecules & Materials Science (ed. by UNESCO & IUPAC), CD-ROM, compiled by UNESCO Associated Centre for Macromolecules and Materials, University of Stellenbosch, South Africa.

Fontaine, J., B. Schirmer, J. Horr. 2002. Near-infrared reflectance spectroscopy (NIRS) enables the fast and accurate prediction of essential amino acid contents. 2. Results for wheat, barley, corn, triticale, wheat bran/middlings, rice bran, and sorghum. *Journal of agricultural and food chemistry* 50(14): 3902-3911.

Freeman, J. A. and M.S. David. 1991. Neural networks algorithms, applications, and programming techniques. Addison-Wesley Publishing Company.

Graf, G.L. 1982. Automatic Detection of Surface Blemishes on Apples using Digital Image Processing. Ph.D. thesis. Cornell University, Ithaca, New York.

Goedeken, D. L., C. H. Tong, R. R. Lentz. 1992. Design and calibration of a continuous temperature measurement system in a microwave cavity by infrared imaging. *Journal of Food Processing and Preservation* 15:331-337.

Graydon O. 1999. Light scatter checks tissue health, *Opto and Laser Europe* :11.

Han, Y.J., S.V. Bowers, R. B. Dodd. 1992. Nondestructive detection of split-pit peaches. *Transactions of the ASAE* 35 (6): 2063 –2067.

Hansen, J.D. 2001. Ultrasound treatments to control surface pests to fruit. *HortTechnology* 11(2): 186-188.

Harrick, N. J. 1960. Study of Physics and Chemistry of Surfaces from Frustrated Total Internal Reflections. *Phys. Rev. Lett.* 4: 224–226

Harvard School of Public Health. 2004. Fruits and Vegetables. [Online available] WWW: <http://www.hsph.harvard.edu/nutritionsource/fruits.html>

Heeger, D.J., and R. B. James. 1995. Pyramid-based texture analysis/synthesis, *Proceedings of the 22nd annual conference on Computer graphics and interactive techniques*: 229-238

Heitschmidt, J., M. Lanoue, C. Mao, G. May. 1998. Hyperspectral analysis of fecal contamination: a case study of poultry, *SPIE* 3544:134-137.

- Heinemann, P.H., Z.A. Varghese, C.T. Morrow, H.J. Sommer III, R.M. Crassweller. 1995. Machine vision inspection of “Golden Delicious” apples. *Appl. Eng. Agric.* 11(6): 901-906.
- Hitachi. 2003. Hitachi releases the media processor “BroadGere™ Series” with an improved video processing performance. [online available]
WWW:http://www.hitachi.com/New/cnews/030331_030331.pdf
- Houser, P. R. 2002. Air and water monitoring for homeland security, *Earth Observation Magazine* 11(8):33-36.
- Hu, Yu Hen and Jenq-neng Hwang. 2002. Handbook of neural network signal processing. CRC press, Boca Raton, FL.
- Huebschman, M. L., R. A. Schultz, H.R. Garner. 2002. Characteristics and capabilities of the hyperspectral imaging microscope. *IEEE Eng Med Biol Mag.* 21(4):104-117.
- Indigo Systems. 2000. Merlin infrared camera user manual.
- Jaffer F.A., C.H. Tung, J. J. Wykrzykowska, N.H.Ho, A.K. Hounq, G.L. Reed, R. Weissleder. 2003. Molecular imaging of factor XIIIa activity in thrombosis using a novel, near-infrared fluorescent contrast agent that covalently links to thrombi. *Circulation* 110(2):170-176.
- Jain, N.C., M.J. Paape, R.H. Miller. 1991. Use of flow cytometry for determination of differential leukocyte counts in bovine blood. *American journal of veterinary research.* 52(4): 630-636.
- Jain, A. K., P. Robert, W. Duin, J. Mao. 2000. Statistical pattern recognition: a review. *IEEE Transactions on Pattern Aanalysis and Machine Intelligence* 22(1): 4-37.
- Jing, H. 2003. Laser range imaging for on-line mapping of 3d images to pseudo-X-ray images for poultry bone fragment detection. Ph.D. Dissertation. University of Maryland, College Park, MD.
- Johnson, D.E. 1998. Applied multivariate methods for data analysis. Duxbury press, Pacific Grove, CA.
- Kim, M.S., K. Chao, Y.R. Chen, D.E. Chan, and P.M. Mehl. 2000. Hyperspectral imaging system for food safety: detection of fecal contamination on apples. In *Environmental and Industrial Sensing: Photonic Detection and Intervention Technologies for Safe Food*, Boston MA, SPIE 4206:174-184

- Kim, S. and T. F. Schatzki. 2000. Apple water core sorting using X-ray imagery : I . Algorithm development. *Transactions of the ASAE* 43 (6): 1695 –1702.
- Kim, S. and T. F. Schatzki. 2001. Detection of pinholes in almonds through X-ray imaging. *Transactions of the ASAE* 44 (4):997 –1003.
- Kim, M. S., Y. R. Chen, P. M. Mehl. 2001. Hyperspectral Reflectance and Fluorescence Imaging System for Food Quality and Safety. *Trans. ASAE* 44 (3): 721-729.
- Kim, M. S., A. M. Lefcourt, Y. R. Chen, I. Kim, D.E. Chan, and K. Chao. 2002a. Multispectral Detection of Fecal Contamination on Apples Based on Hyperspectral Imagery: Part I. Applications of Visible and Near-Infrared Reflectance Imaging. *Trans. ASAE* 45(6): 2027-2037.
- Kim, M. S., A. M. Lefcourt, Y. R. Chen, I. Kim, D.E. Chan, and K. Chao. 2002b. Multispectral Detection of Fecal Contamination on Apples Based on Hyperspectral Imagery: Part II. Applications of Hyperspectral Fluorescence Imaging. *Trans. ASAE* 45(6): 2039-2047.
- Kong, S. G. , Y. R. Chen, I. Kim, M. S. Kim. 2004. Analysis of hyperspectral fluorescence images for poultry skin tumor inspection. *Applied Optics*. 43(4):824-833.
- Korsman, T., M.B. Nilsson, K. Langren, I. Renberg. 1999. Spatial variability in surface sediment composition characterised by near-infrared (NIR) reflectance spectroscopy. *Journal of Paleolimnology* 21: 61-71.
- Korsman, T., M. Nilsson, J. Ohman, I. Renberg. 1992. Near-infrared reflectance spectroscopy of sediments: A potential method to infer the past pH of lakes. *Environmental Science and Technology* 26: 2122-2126.
- Laine, A. and J. Fan. 1993. Texture classification by wavelet packet signatures, *IEEE Transactions on Pattern Analysis and Machine Intelligence* 15(11): 1186-1191.
- Landgrebe, D. 2002, Hyperspectral image data analysis, *IEEE Signal Processing Magazine* 19(1):17-28.
- Laplante, P. A. and A. D. Stoyenko. 1996. Real-time imaging: theory, techniques, and applications. New York, N.Y.: IEEE press.
- Laporte, M.F. and P. Paquin. 1999. Near-infrared analysis of fat, protein, and casein in cow's milk. *Journal of agricultural and food chemistry* 47(7): 2600-2605.

- Lassiter S.J, W. Stryjewski , B.L. Legendre Jr, R. Erdmann, M. Wahl, J. Wurm, R. Peterson, L. Middendorf, S.A. Soper. 2000. Time-resolved fluorescence imaging of slab gels for lifetime base-calling in DNA sequencing applications. *Anal Chem* 72(21):5373-82.
- Laykin S., Y. Edan, V. Alchanatis, R. Regev, F. Gross, J. Grinshpun, E. Bar-Lev, E. Fallik, S. Alkalai. 1999. Development of a quality sorting machine using machine vision and impact, *ASAE/CSAE-SCGR Annual International Meeting, Toronto, Ontario, Canada*.
- Leemans, V., H. Magein, M.F. Destain. 1999. *Defect segmentation on 'Jonagold' apples using colour vision and a Bayesian classification method*. *Computers and electronics in agriculture* 23(1): 43-53.
- Lin W.C and P.A. Jolliffe. 1996. Light intensity and spectral quality affect fruit growth and shelf life of greenhouse-grown long English cucumber. *Journal of the American Society for Horticultural Science* 121(6):1168-1173.
- Lu, R. and Y. R. Chen. 1998. Hyperspectral imaging for safety inspection of food and agricultural products, *SPIE* 3544:121-133.
- Lu, R., Y.R. Chen, B. Park, and K.H. Choi. 1999. Hyperspectral imaging for detecting bruises in apples, *ASAE Annual International Meeting* Paper No. 993120.
- Lu, R. 2001. Predicting firmness and sugar content of sweet cherries using near-infrared diffuse reflectance spectroscopy. *Transactions of the ASAE* 44(5): 1265-1271.
- Lu, R. and Y. Peng. 2004. Hyperspectral scattering for assessing peach fruit firmness. *ASAE Annual International Meeting* Paper No. 046117.
- Malley, D.F., S.G. Lawrence, M.H. Holoka, P.C. Williams. 1996. Applying near-infrared reflectance spectroscopy to measure carbon, nitrogen, phosphorus, and organic-bound cadmium in lake picoplankton. *Journal of Aquatic Ecosystem Health* 5: 135-147.
- Malley, D.F., H. Röncke, D.L. Findlay, B. Zippel. 1999. Feasibility of using near-infrared reflectance spectroscopy for the analysis of C, N, P, and diatoms in lake sediments. *Journal of Paleolimnology* 21: 295-306.
- Malley, D.F., L. Lockhart, P. Wilkinson, B. Hauser. 2000. Determination of carbon, carbonate, nitrogen, and phosphorus in freshwater sediments by near-infrared reflectance: rapid analysis and a check on conventional analytical methods. *Journal of Paleolimnology* 24: 415-425.

- Managuli R. and Y. Kim. 2002. Mediaprocessors in medical imaging for high performance and flexibility. *Proc. of SPIE conf. medical imaging* 4687.
- Manjunath, B. S. and W. Y. Ma. 1996. Texture features for browsing and retrieval of image data. *IEEE Transactions on Pattern Analysis and Machine Intelligence* 18(8):837-42.
- Martín-Herrero J. and J. L. Alba-Castro. 2003. Real Time Machine Vision for Quality Assurance of Canned Tuna. *Mechatronics and Machine Vision in Practice*.
- Mehl, P. M., Y. R. Chen, M. S. Kim, D. E. Chan. 2004. Development of hyperspectral imaging technique for the detection of apple surface defects and contaminations, *Journal of Food Engineering* 61(1): 67-81.
- Meldrum R.A, S.W. Botchway, C. W. Wharton, G.J. Hirst. 2003. Nanoscale spatial induction of ultraviolet photoproducts in cellular DNA by three-photon near-infrared absorption. *EMBO* 4(12):1144-9.
- Miller B.K and M.J.Delwiche. 1991. Peach defect detection with machine vision. *Trans. ASAE* 34(6):2588-2597.
- Miller W.M. and G.P. Drouillard. 1997. On-Line blemish, color and shape analysis for Florida citrus. *Proc. Sensors for Nondestructive Testing: Measuring the quality of fresh fruit and vegetables* 97: 249-260.
- Miralbes, C. 2003. Prediction chemical composition and alveograph parameters on wheat by near-infrared transmittance spectroscopy. *Journal of agricultural and food chemistry* 51: 6335-6339.
- Motorola Inc. 1998. Motorola Sensor Device Data/Handbook, Rev. 4.
- Muramatsu, N., N. Sakurai, N. Wada, R. Yamamoto, K. Tanaka, T. Asakura, Y. Ishikawa-Takano, D.J. Nevins. 2000. Remote sensing of fruit textural changes with a laser doppler vibrometer. *Journal of the American Society for Horticultural Science* 125(1) : 120-127.
- Nilsson, M., E. Dåbakk, T. Korsman, I. Renberg. 1996. Quantifying relationships between near-infrared reflectance spectra of lake sediments and water chemistry. *Environ. Sci. Technol* 30: 2586-2590.
- Park, B., K. C. Lawrence, W. R. Windham, R. J. Buhr. 2002. Hyperspectral Imaging for Detecting Fecal and Ingesta Contaminants on Poultry Carcasses. *Trans. ASAE* 45(6):2017-2026.

Paulus, I. and E. Schrevens. 1999. Shape characterization of new apple cultivars by Fourier expansion of digitized images. *Journal of agricultural engineering research*. 72(2): 113-118.

Peiris, K.H.S., G.G. Dull, R.G. Leffler, S.J. Kays. 1998. Near-infrared spectrometric method for nondestructive determination of soluble solids content of peaches. *Journal of the American Society for Horticultural Science* 123(5): 989-905.

Peirs, A., N. Scheerlinck, K. Touchant. 2002. Comparison of fourier transform and dispersive near-infrared reflectance spectroscopy for apple quality measurements. *Biosystems engineering* 81(3):305-311.

Penman D.W. 2001. Determination of stem and calyx location on apples using automatic visual inspection, *Computers and Electronics in Agriculture* 33(1): 7-18.

Perez-Vich, B., L.Velasco, J.M. Fernandez-Martinez. 1998. Determination of seed oil content and fatty acid composition in sunflower through the analysis of intact seeds, husked seeds, meal and oil by near-infrared reflectance spectroscopy. *Journal of the American Oil Chemists' Society* 75(5): 547-555.

Pla, F., F. Juste, F. Ferri. 1993. Feature extraction of spherical objects in image analysis: an application to robotic citrus harvesting. *Computers and electronics in agriculture* 8(1): 57-72.

Pla F. and F. Juste. 1995. A thinning-based algorithm to characterize fruit stems from profile images, *Computers and Electronics in Agriculture* 13(4): 301-314.

Raczkowsky J., H. Peters, C. Kübler, D. Engel, H. Wörn. 2003. ACTIVE END EFFECTOR FOR SURGICAL ROBOT. *Mechatronics and Machine Vision in Practice* 2003.

Raghavachari, Ramesh. 2001. Near infrared applications in biotechnology. Marcel Dekker, Inc.

Raj A., S. J. Bertolone, S. Mangold, H. L. Edmonds Jr. 2004. Assessment of cerebral tissue oxygenation in patients with sickle cell disease: effect of transfusion therapy. *J Pediatr Hematol Oncol* 26(5): 279-283.

Registerm, J. 1998. The Basics of IR Thermometry. [Online available] WWW: http://www.sensorsmag.com/articles/0898/ir0898/ir08_sb1.shtml

Russell, S. J. and P. Norvig. 2002. Artificial Intelligence: A Modern Approach (2nd Edition). Prentice Hall.

Saltveit, M. E. Jr., and L. L. Morris. 1990. Overview on Chilling Injury of Horticultural Crops. In *Chilling Injury of Horticultural Crops*, 3-16, C. Y. Wang, ed. CRC Press, Inc. Boca Raton, Florida.

Sarkar, N. and R.R. Wolfe. 1985. Feature extraction techniques for sorting tomatoes by computer vision. *Transactions of the ASAE - American Society of Agricultural Engineers* 28(3): 970-979.

Scanlon, M.G., M.K. Pritchard, L.R.Adam. 1999. Quality evaluation of processing potatoes by near infrared reflectance. *Journal of the science of food and agriculture* 79(5): 763-771.

Schatzki, T.F., R.P. Haff, R. Young, I. Can, L. C. Le, N. Toyofuku. 1997. Defect detection in apples by means of x-ray imaging. *Transactions of the ASAE* 40(5): 1407-1415.

Schultz, R. A., T. Nielsen ,J. R. Zavaleta, R. Ruch, R. Wyatt, H. R. Garner. 2001. Hyperspectral imaging: a novel approach for microscopic analysis, *Cytometry* 43(4):239-47.

Shah K, A. J., X.O. Breakefield, R. Weissleder. 2004. Molecular imaging of gene therapy for cancer. *Gene Ther* 11(15):1175-87.

Shah N, A.E. Cerussi, D. Jakubowski, D. Hsiang, J. Butler, B.J. Tromberg. Spatial variations in optical and physiological properties of healthy breast tissue. *J Biomed Opt.* 9(3):534-40.

Shahin, M.A., E. W. Tollner, M. D. Evans, H. R. Arabnia. 1999. Watercore features for sorting red delicious apples: a statistical approach. *Transactions of the ASAE.* 42(6):1889-1896.

Shaw M. 1998. System Aspects of a Sensor System on a Chip, *Proc Sensors Expo Chicago*.

Shaw, G., and D. Manolakis. 2002. Signal Processing for Hyperspectral Image Exploitation. *IEEE Signal Processing Magazine* 19(1):12-16.

Siesler H.W. 1996. Characterization of Polymer Deformation by Vibrational Spectroscopy. *Oriented Polymer Materials (Ed. S. Fakirov):* 138-166

Siesler H.W. 2000. Quality-Control and Process Monitoring by Mid-Infrared, Near-Infrared and Raman Spectroscopy. In *Near Infrared Spectroscopy: Proceedings of 9th International NIR Conference:* 331-337

- Sinclair, M. B., A. Jerilyn, D. M. Timlin, H. M. Werner-Washburne. 2004, Design, Construction, characterization, and application of a hyperspectral microarray scanner. *Applied Optics* 43(10):2079-2088.
- Slaughter, D.C., R.C. Harrell, P.D. Adsit, T.A. Pool.1986. Image enhancement in robotic fruit harvesting. *American Society of Agricultural Engineers (Microfiche collection)*. fiche : 22.
- Song, J., W.M. Deng, R.M.Beaudry, P.R. Armstrong. 1997. Changes in chlorophyll fluorescence of apple fruit during maturation, ripening, and senescence. *HortScience : a publication of the American Society for Horticultural Science* 32(5): 891-896.
- Song, J., L. Fan, C. F. Forney, M. A. Jordan. 2001. Using volatile emissions and chlorophyll fluorescence as indicators of heat injury in apples. *Journal of the American Society for Horticultural Science* 126(6) :771 -777.
- Sowell J., L. Strekowski, G. Patonay. 2002. DNA and protein applications of near-infrared dyes. *J Biomed Opt.* 7(4): 571-575.
- Spanner G and R. Niessner. 1996. Noninvasive determination of blood constituents using an array of modulated laser diodes and a photoacoustic sensor head. *Anal Bioanal Chem.* 55(3-4):327-328.
- Stiefvater, T.L. 1970. Investigation of An Optical Apple Bruise Detection Technique. M.S. Thesis, Cornell University, Ithaca, New York.
- Sugiyama, J. 1999. Visualization of sugar content in the flesh of a melon by near-infrared imaging. *Journal of agricultural and food chemistry* 47(7): 2715-2718.
- Talukder, A. and D. Casasent,. 1998. A General Methodology for Simultaneous Representation and Discriminant of Multiple Object Classes, *Optical Engineering, Special issue on "Advances in Recognition Techniques"*.
- Tao, Y., L. Chance, B. Liu, 1995. *Full-scale fruit vision sorting system design – factors and considerations*. In Food Processing Automation IV. ASAE Publication. ISBN 0-929355-70-9,
- Tao, Y. 1996. *Spherical transform of fruit images for on-line defect extraction of mass objects*. *Opt. Eng.* 35(2): 334-350.
- Tao, Y. 2001. Photonics in Fruit and Vegetable Quality Assessment, *Optics in Agriculture, A Critical Review 1990-2000*, James A. DeShazer and George E. Meyer eds. *SPIE* 80: 64-100.

- Tao, Y. and Z. Wen. 1999. *An adaptive spherical image transform for high-speed fruit defect detection. Transactions of the ASAE* 42(1): 241-246.
- Taylor, R.W., G.E. Rehkugler, J.A. Throop. 1983. Apple bruise detection using a digital line scan camera system. In: *Agricultural electronics--1983 and beyond : proceedings of the National Conference on Agricultural Electronics Applications, December 11-13, 1983, Hyatt Regency Illinois Center, Chicago, Illinois*
- Terasaki, S., N. Wada, N. Sakurai, N. Muramatsu, R. Yamamoto, D.J. Nevins. 2001. Nondestructive measurement of kiwifruit ripeness using a laser Doppler Vibrometer. *Transactions of the ASAE* 44(1): 81-87.
- Throop, J.A., D.J. Aneshansley, B.L. Upchurch. 1995. An image processing algorithm to find new and old bruises. *Applied engineering in agriculture* 11(5): 751-757.
- Throop J.A., D.J. Aneshansley, B.L. Upchurch. 1997. Apple orientation on automatic sorting equipment, *Proc. Sensors for Nondestructive Testing: Measuring the quality of fresh fruit and vegetables, Orlando Florida* 97: 328-342.
- Tollner, E.W., Shahin, M.A., Maw, B.W., Gilaitis, R.D., Summer, D.R., 1999. Classification of onions based on internal defects using imaging processing and neural network techniques. *1999 ASAE International Meeting Paper No. 993165.*
- Toyserkani E., A. Khajepour, S. Corbin. 2003. Vision-based Feedback Control of Laser Powder Deposition. *Mechatronics and Machine Vision in Practice* 2003.
- Tsatsanis, M., K. Georgios, B. Giannakis. 1992. Object and texture classification using higher order statistics, *IEEE Transactions on Pattern Analysis and Machine Intelligence* 14(7): 733-750.
- Tuceryan, M. and A. K. Jain. 1990. Texture segmentation using Voronoi polygons, *IEEE Transactions on Pattern Analysis and Machine Intelligence* 12(2): 211-216.
- USDA, 2001. Agricultural Statistics: On-line database. [Online available] WWW: <http://www.usda.gov/nass/pub/agstas.htm>.
- Varith, J. 2001. Uses of thermal properties for non-destructive assessment of apple quality. Ph.D. Dissertation, Washington State University, Pullman, WA
- Varith, J., G.M. Hyde, A.L. Baritelle, J.K. Fellman. 2003. Sattabongkot, T. Non-contact bruise detection in apples by thermal imaging. *Innovative Food Science and Emerging Technologies* 4(2): 211-218
- Varith, J., G. M. Hyde, J. Tang, M. J. Pitts. 2001. Validation of bruise detection by thermal imaging using the finite element simulation. In *Uses of thermal properties for*

- nondestructive assessment of apple quality. Ph.D. Dissertation. Washington State University, Pullman, WA.
- Vogel, S. 2003. Military has high hopes for new eye in the sky sensor-equipped blimps could aid homeland security. *Washington Post*, August 8, 2003:B01
- Wabuyele M. B., S.M. Ford, W. Stryjewski, J. Barrow, S. A. Soper. 2001. Single molecule detection of double-stranded DNA in polymethylmethacrylate and polycarbonate microfluidic devices. *Electrophoresis* 22 (18): 3939-3948.
- Wen, Z. and Y. Tao. 1997. Adaptive Spherical Transform of Fruit Images for High-Speed Defect Detection. *ASAE International Meeting Paper No. 973076*.
- Wen Z. and Y. Tao. 1998a. Method of dual-camera NIR/MIR image for fruit sorting. *ASAE International Meeting Paper No. 983043*.
- Wen Z. and Y. Tao. 1998b. Dual-wavelength imaging for online identification of stem ends and calyxes. *Proc. SPIE* 3460: 249-253.
- Wen, Z. and Y. Tao. 2000. Dual-camera NIR/MIR imaging for stem-end/calyx identification in apple defect sorting. *Trans. ASAE* 43(2): 449-452.
- Wilhoit, J.H., A.L. Auburn, L.J. Kutz, D.E. Fly, D.B. South. 1994. PC-based multiple camera machine vision systems for pine seedling measurements. *Applied engineering in agriculture* 10(6): 841-847.
- Windhan, W. R., K. C. Lawrence, B. Park, R. J. Buhr. 2001. Visible/NIR Spectroscopy for Characterizing Fecal Contamination of Chicken Carcasses, *ASAE International Meeting Paper No. 016004*.
- Wolfe R.R., W.E. Sandler. 1985. An algorithm for stem detection using digital image analysis, *Trans. ASAE* 28(2): 641-644.
- Wu, J.G., C. Shi, X. Zhang. 2002. Estimating the amino acid composition in milled rice by near-infrared reflectance spectroscopy. *Field crops research* 75(1): 1-7.
- Xiang, Y., Y. Vanessa, J. Silverberg, M. B. Schaffler, T. Raphan. 2003. Quantification of trabecular bone mass and orientation using Gabor wavelets, Proceedings of the 2003 ACM symposium on Applied computing.
- Yang, Q. 1993. Finding stalk and calyx of apples using structured lighting. *Comput. Electron. Agric.* 8:31-42.

- Yang, Q. 1996. Apple stem and calyx identification with machine vision. *J. Agricultural Engineering Research* 63(3): 229-236.
- Zhang, H.Z., W. Zeng, M. Rutman. 2000. Simultaneous determination of moisture, protein and fat in fish meal using near-infrared spectroscopy. *Food science and technology research* 6(1): 19-23.
- Zhu, Y., T. Tan , Y. Wang. 2001. Font recognition based on global texture analysis, *IEEE Transactions on Pattern Analysis and Machine Intelligence* 23(10):1192-1200.
- Zuech, N. 2004. Machine Vision and Lighting. *Machine Vision On Line*. [Online available] WWW:
<http://www.machinevisiononline.org/public/articles/archivedetails.cfm?id=1430>.